Structural and electronic properties of nickelate heterostructures

Von der Fakultät Chemie der Universität Stuttgart
zur Erlangung der Würde einer Doktorin der Naturwissenschaften
(Dr. rer. nat.) genehmigte Abhandlung

Vorgelegt von

Friederike Wrobel

aus Braunschweig (Deutschland)

Hauptberichter:	Prof. Dr. Bernhard Keimer
Mitberichterin:	Prof. Dr. Anke Weidenkaff
Prüfungsvorsitzender:	Prof. Dr. Rainer Niewa

Tag der Einreichung:	18.07.2016
Tag der mündlichen Prüfung:	19.08.2016

Max-Planck-Institut für Festkörperforschung
Stuttgart 2016

Contents

Abbreviations

ABF	Annular bright field
ADF	Annular dark field
AFM	Antiferromagnetic
AFM	Atomic force microscopy
ARPES	Angle-resolved photoemission spectroscopy
a.u.	arbitrary units
CDW	Charge density wave
cps	counts per second
DM	Dzyaloshinskii-Moriya
EELS	Electron energy loss spectroscopy
E_F	Fermi energy
emu	electromagnetic units
FC	Field-cooled
FL	Fermi liquid
FY	Fluorescence yield
FS	Fermi surface
GSO	Gadolinium scandate, i.e., $GdScO_3$
HAADF	High-angle annular dark field
HRTEM	High-resolution TEM
HTSC	High-temperature superconductor
JT	Jahn-Teller
$\underline{L}$	Ligand hole

LCO	Lanthanum copper oxide, i.e., La_2CuO_4
LAO	Lanthanum aluminate, i.e., $LaAlO_3$
LHB	lower Hubbard band
LNO	Lanthanum nickelate, i.e., $LaNiO_3$
LSAO	Lanthanum strontium aluminate, i.e., $LaSrAlO_4$
LSAT	Lanthanum strontium aluminum tantalate, i.e., $(LaAlO_3)_{0.3}$-$(Sr_2AlTaO_6)_{0.7}$
LSO	Lanthanum scandate, i.e., $LaScO_3$
MBE	Molecular beam epitaxy
MIT	Metal-insulator transition
MR	Magnetoresistance, i.e., $(\rho_{0\mathrm{T}} - \rho_B)/\rho_{0\mathrm{T}}$
NFL	Non-Fermi liquid
pc	pseudo-cubic
PLD	Pulsed laser deposition
PPMS	Physical properties measurement system
pt	pseudo-tetragonal
QCM	Quartz crystal microbalance
QCP	Quantum critical point
RBS	Rutherford backscattering
RE	Rare earth element
RGA	Residual-gas analyzer
RHEED	Reflection high-energy electron diffraction
rlu	reciprocal lattice units
RP phases	Ruddlesden-Popper phases
RRR	Residual resistance ratio, i.e., ρ_{300K}/ρ_{4K}
RSM	Reciprocal space map
SDW	Spin-density wave
SL	Superlattice
SNR	Signal-to-noise ratio
SOC	Spin-orbit coupling
SQUID	Superconducting quantum interference device
STEM	Scanning transmission electron microscopy

STO	Strontium titanate, i.e., $SrTiO_3$
T_c	critical temperature below which a material is in the superconducting state
TEM	Transmission electron microscopy
TEY	Total electron yield
TGA	Thermogravimetric analysis
TM	Transition metal
TMO	Transition metal oxide
T_N	Néel temperature
u.c.	unit cell
UHB	Upper Hubbard band
WAL	Weak anti-localization
WL	Weak localization
XAS	X-ray absorption spectroscopy
XLD	X-ray linear dichroism
XMCD	X-ray magnetic circular dichroism
XMLD	X-ray magnetic linear dichroism
XRD	X-ray diffraction
XRR	X-ray reflectivity
YBCO	$YBa_2Cu_3O_7$
ZFC	Zero-field-cooled

Zusammenfassung in deutscher Sprache

An der Grenzfläche zweier Materialien treten häufig Effekte zu Tage, die in den isolierten Bulk-Versionen der selben Materialien nicht zu finden sind. Des Weiteren führt die Beschränkung in einer oder mehreren Dimensionen zu neuartigen physikalischen Verhaltensweisen. Zum Beispiel wird $LaNiO_3$ (LNO), das im Bulk paramagnetisch und metallisch ist, und das als dünne Schicht auf einem einkristallinen Substrat mit atomar glatter Oberfläche gewachsen wird, schwach isolierend und antiferromagnetisch, sobald die Dicke der einzelnen Nickelat-Lagen nur noch zwei Einheitszellen beträgt und diese Lagen in Form eines sogenannten Übergitters mittels eines Bandisolators, hier $LaAlO_3$ (LAO), voneinander getrennt sind. [1, 2] Außerdem zeigten ähnliche Übergitter, bei denen die Dicke der Nickelatschicht nur noch eine Einheitszelle betrug, in Modellrechnungen Ähnlichkeiten mit Hochtemperatursupraleitern. [3, 4] Diese Hoffnung auf Supraleitung hat sich bisher nicht erfüllt, nichtsdestotrotz hat das Feld in den letzten Jahren einen großen Aufschwung erfahren und die Eigenschaften von nickelatbasierten Übergittern und ultradünnen Filmen wurden umfassend untersucht.

Der Großteil der aus der Literatur bekannten Proben wurde entweder mittels Magnetronsputtern oder Laserstrahlverdampfen (*engl.* “pulsed laser deposition”, PLD) hergestellt. Im Rahmen der vorliegenden Arbeit wird eine weitere Methode zur Probenherstellung vorgestellt, nämlich mittels Oxid-Molekularstrahlepitaxie (*engl.* “oxide molecular beam epitaxy” bzw. “ozone-assisted molecular beam epitaxy”, MBE). Das Probenwachstum mittels MBE hat den Vorteil, dass die abgeschiedenen Teilchen eine weitaus geringere kinetische Energie haben, als das mit anderen Methoden der Fall ist. Dadurch kann man glattere Grenzflächen erwarten. Des Weiteren schafft die Kontrolle über einzelne atomare Lagen, im Gegensatz zur Kontrolle über einzelne

Einheitszellen in PLD und Sputtering, neue Möglichkeiten des Designs neuartiger Materialien mit funktionalen Eigenschaften. Der damit einhergehende Nachteil ist eine erschwerte Einstellung des Verhältnisses der einzelnen Atomsorten zueinander, da mittels Elektronenstrahlbeugung (*engl.* “reflection high-energy electron diffraction”, RHEED), das als in-situ Kontrollmethode zur Verfügung steht, nicht immer zweifelsfrei das Abschließen einer kompletten Atomlage bestimmt werden kann. Zudem ist man in der Wahl des Kammerdrucks während des Wachstums eingeschränkt, da ein ballistischer Transport der Atome von der Effusionszelle zum Substrat gewährleistet sein muss. Der Druck ist neben der Temperatur ein empfindlicher Parameter im chemischen Gleichgewicht, der über die Stabilität der einen oder anderen Phase entscheidet.

Man muss also, um das gewünschte Produkt in hoher Qualität zu erhalten, das empfindliche Gleichgewicht aus Temperatur, Druck und Stöchiometrie beherrschen. Und so wird zu Beginn dieser Arbeit gezeigt, wie es möglich ist $LaNiO_3$ und Übergitter daraus in hoher Qualität zu wachsen, obwohl eine große Neigung zur Bildung von Sauerstofffehlstellen und Fremdphasen, insbesondere Ruddlesden-Popper-Phasen ($La_{n+1}Ni_nO_{3n+1}$, $1 \leq n \leq \infty$), besteht. Das Gros der Filme und Übergitter wurde auf LSAT-Substraten, einem Mischkristall aus $LaAlO_3$ und Sr_2TaAlO_6 mit nur leicht größeren Gitterparametern als LNO, gewachsen und auf diese Proben werden wir uns im folgenden konzentrieren.

Wir vergleichen die Eigenschaften unserer Proben mit aus der Literatur bekannten Werten und mit nominell identischen Proben, die mittels PLD gewachsen wurden, und stellen eine große Übereinstimmung fest. Besonders bemerkenswert ist die hohe elektrische Leitfähigkeit mit einem geringem Restwiderstand, die alle bisher gemessenen Werte übertrifft. [5–8] Daneben sind, wie erwartet, die Grenzflächen der MBE-Proben zwischen Substrat und Probe, sowie zwischen den unterschiedlichen Lagen, glatter und weisen weniger Durchmischung auf. Im Gegenzug besitzen MBE-Proben eine höhere Dichte sogenannter 3D-Ruddlesden-Popper-Defekte. Hier führt ein leichter Nickel-Mangel bzw. ein Überschuss an Lanthan zu einer zusätzlichen Lage Lanthanoxid und zu einer Verschiebung der darüber liegenden Schichten um eine halbe Einheitszelle. Des Weiteren beobachten wir einen Unterschied in der Form der Röntgenabsorptionslinien, der möglicherweise mit der Grenzflächenrauigkeit zusammenhängt, indem nämlich die chemische Umgebung eines Nickelatoms verändert wird.

Damit einher geht die unterschiedliche Besetzung der e_g-Orbitale. Während diese in Bulk-LNO entartet und gleichermaßen von einem Elektron besetzt sind – in einem vereinfachten Bild besitzt Nickel in LNO eine $3d^7$-Konfiguration, wovon sechs Elektronen in den t_{2g}-Orbitalen und eines in den e_g-Orbitalen zu finden sind – führt die epitaktische Verpannung durch das Substrat und die Einschränkung der Bewegung der Elektronen senkrecht zur Probenoberfläche zu einer bevorzugten Besetzung der in der Ebene liegenden $3d_{x^2-y^2}$-Orbitale. Diese orbitale Polarisation ist erstaunlicherweise in den PLD-Proben größer, kann aber möglicherweise auch durch die unterschiedliche chemische Umgebung des Nickelatoms erklärt werden.

Die Kontrolle über einzelne, atomare Lagen und die geringe Grenzflächenrauigkeit erleichtern bzw. ermöglichen das Wachstum von Übergittern, in denen die LNO-Schicht nur noch eine Einheitszelle dick ist. Wir untersuchten die Evolution der Röntgenabsorptionsspektren in Abhängigkeit der Dicke der LNO-Schicht. Durch die Reduzierung der Dicke nähert sich die Form der Spektren immer mehr derjenigen der Seltenerdnickelate (RENiO$_3$, RE = Seltenerdmetall, z.B. Pr, Nd, Sm, etc.) die einen kleineren Radius des Seltenerdmetalls haben. Im Fall der Seltenerdnickelate ist diese Veränderung der Spektren mit einem Übergang zu einem ladungsgeordnetem, isolierenden Zustand verbunden. Auch in den Übergittern beobachten wir eine zunehmende Lokalisierung der Elektronen. Damit einhergehend ist ein Zuwachs an orbitaler Polarisation mit abnehmender LNO-Dicke. Diese bleibt aber deutlich unter den Werten, die aus theoretischen Modellen vorhergesagt wurden.

Die hohe Qualität insbesondere eines 25 Einheitszellen (entspricht ~95 Å) dicken Films gewachsen auf LSAT ermöglichte es, das temperaturabhängige Verhalten des Widerstands genauer zu untersuchen. Dieses kann unter anderem Aufschluss geben über Elektron-Elektron-Wechselwirkungen und über mögliche magnetische Fluktuationen. So skaliert beispielsweise der Widerstand einer Fermi-Flüssigkeit quadratisch mit der Temperatur. In unserem Fall skaliert der Widerstand unterhalb von 3 K mit einem Exponenten von 1.8. Darüber gibt es einen großen Bereich ohne spezifischen Exponenten, bevor man bei Temperaturen über 140 K einen Exponenten von ungefähr 1.5 findet. Dieses Verhalten wird so von keiner Theorie vorhergesagt.

Als nächstes untersuchten wir das Verhalten der Ladungsträger in Abhängigkeit der Temperatur und der Dicke der LNO-Lagen. Im Einklang mit Literaturwerten für

Bulk-LNO finden wir für Übergitter und dünne Filme mit mindestens vier zusammenhängenden Einheitszellen LNO positive Ladungsträger, deren Dichte stark von der Temperatur abhängt. [9] Durch Messungen in Magnetfeldern bis zu 33 T konnten wir unter Anwendung eines Zweibändermodells zeigen, dass bei tiefen Temperaturen eine zweite Art von (positiven) Ladungsträgern zur Leitfähigkeit beiträgt.

In Übergittern, in denen die LNO-Dicke auf lediglich zwei Einheitszellen reduziert wurde, ist die Ladungsträgerdichte deutlich reduziert. Interessanterweise ist das die gleiche Schichtdicke, bei der eine antiferromagnetische Ordnung gefunden wurde, sodass ein Zusammenhang zu vermuten ist.

Messungen des elektrischen Widerstands in Abhängigkeit des magnetischen Feldes zeigen, dass sich der Widerstand eines LNO-Films im Magnetfeld erhöht. Dies ist ein Zeichen für die hohe Sauerstoffkonzentration in diesem Film. Durch Reduzierung der Schichtdicke reduziert sich auch der Effekt des magnetischen Feldes und kehrt sich sogar ins Negative. Dieses Verhalten ist bedingt durch eine schwache Lokalisierung (*engl.* “weak localization”, WL) der Ladungsträger, die bevorzugt in zweidimensionalen Systemen auftritt. Dieser Trend verläuft graduell bis eine Dicke von drei Einheitszellen LNO erreicht wird. Hinter diesem Punkt steigt der Effekt des magnetischen Feldes auf den Widerstand signifikant an, da die Spins der antiferromagnetisch geordneten Elektronen im magnetischen Feld ausgerichtet werden, wodurch Streuprozesse teilweise unterbunden werden und der Widerstand somit verringert wird.

Zusätzlich zur Dickenabhängigkeit des Magnetwiderstands, wurde das Verhalten eines 25 Einheitszellen dicken Films in magnetischen Feldern bis zu 33 T untersucht. In niedrigen Feldern wächst der Widerstand quadratisch mit dem angelegten Feld, was ein für Metalle relativ normales Verhalten widerspiegelt. Anstatt jedoch einen Sättigungswiderstand zu erreichen oder weiterhin quadratisch mit dem Feld anzuwachsen, was man erwarten würde, wächst der Widerstand ab einem gewissen Punkt linear an ohne zu sättigen. Dieses Verhalten ist für Metalle mit einer großen Fermioberfläche höchst ungewöhnlich und kann im Rahmen der vorhandenen theoretischen Modelle nur unter der Annahme einer kleinen, zusätzlichen Fermioberfläche mit “leichten” Ladungsträgern erklärt werden. Weitere Untersuchungen werden zeigen müssen, ob dies der Fall ist oder ob der lineare Magnetwiderstand anders erklärt werden muss.

Im zweiten Teil der Arbeit wird die Kontrolle über einzelne, atomare Lagen, die

die Technik der MBE bietet, ausgenutzt, um neuartige Materialien zu wachsen, die in dieser Form nicht in der Natur vorkommen und die mit keiner anderen Wachstumsmethode hergestellt werden können. Wir haben Hybridstrukturen aus La_2CuO_4 (LCO) und $LaNiO_3$ hergestellt, wobei sich zwischen den La_2CuO_4- und $LaNiO_3$-Lagen jeweils zwei Lanthanoxid-Lagen befinden, sodass die Struktur als eine Komposition aus La_2CuO_4 und der entsprechenden Ruddlesden-Popper-Phase, $La_{n+1}Ni_nO_{3n+1}$, zu sehen ist. Daraus folgt die, allgemeine Summenformel für derartige *Hybridstrukturen*: $[(La_2CuO_4)_nLaO(LaNiO_3)_m]_l$, abgekürzt lx(n//m)

Versuche, diese zusätzliche Lanthanoxid-Lage wegzulassen, waren nicht erfolgreich, da sich die Atomlagen jeweils so anordneten, dass stets zwei Lanthanoxid-Lagen die Kuprat- und Nickelat-Schichten trennten. Wir können also schlussfolgern, dass Kupfer in direkter Nachbarschaft zu Nickel (nur getrennt durch ein gemeinsames Sauerstoffatom) unter MBE-Wachstumsbedingungen nicht stabil ist.

Die hohe Qualität einer einzelnen Probe – 6x(3//4) – erlaubte es uns, via Rastertransmissionselektronenmikroskopie (*engl.* scanning transmission electron microscopy, STEM) sogar die Positionen der Sauerstoffatome in den einzelnen Kuprat- und Nickelat-Lagen zu verfolgen. So sind die Kupfer-Sauerstoff-Oktaeder bzw. die Nickel-Sauerstoff-Okateder entlang der Wachstumsrichtung, im Vergleich zur lateralen Ausdehnung, gestreckt. Im Falle von Kupfer kann dieses Verhalten durch eine Jahn-Teller-Verzerrung erklärt werden. Wenn man jedoch die gemessenen Werte mit denen von Bulk-LCO vergleicht, stellt man fest, dass die Oktaeder in der Hybridstruktur weniger verzerrt sind. Dies kann nur teilweise durch die vom Substrat verursachte Verspannung erklärt werden. Gründe darüber hinaus sind ein möglicher Ladungstransfer über die Grenzfläche hinweg, ein gehäuftes Auftreten von Sauerstofffehlstellen an der Grenzfläche oder Grenzflächenrauigkeit. Im Fall der Nickel-Oktaeder erkennt man einen Unterschied zwischen inneren und äußeren (an der Grenzfläche) Lagen. So sind die Oktaeder an der Grenzfläche mit einem Abstand der Apex-Sauerstoffe von 4.11 Å stärker gestreckt als die inneren mit einem Abstand von 3.91 Å. Dem liegt eine unterschiedliche Koordination der beiden Nickelatome zu Grunde.

Diese Unterschiede spiegeln sich auch in den Röntgenabsorptionsspektren wider, durch die man zeigen kann, dass sich Kupfer hauptsächlich im Oxidationszustand +II befindet. Allerdings treten auch geringe Variationen von Probe zu Probe auf, die nicht

auf einfache Weise erklärt werden können. Der Oxidationszustand des Nickels liegt zwischen +II und +III und auch hier sehen wir Unterschiede zwischen verschiedenen Proben, die wir im Detail diskutieren.

Die Verwendung von linear polarisiertem Röntgenlicht erlaubt es, den Unterschied in der Orbitalbesetzung zwischen in der Ebene liegenden $3d_{x^2-y^2}$-Orbitalen und aus der Ebene zeigende $3d_{3z^2-r^2}$-Orbitalen festzustellen. Hierdurch zeigt sich, dass in beiden Fällen (Kupfer und Nickel), das $3d_{3z^2-r^2}$-Orbital bevorzugt besetzt wird. Dies steht in direktem Zusammenhang mit der Streckung der Oktaeder, die wir durch STEM beobachten konnten.

Messungen der Magnetisierung mit Hilfe eines SQUID-Magnetometers zeigen einen schwach ferromagnetisch geordneten Zustand unterhalb von 165 K in allen gemessenen Proben. Die Tatsache, dass sich ein LCO-Dünnfilm gleich verhält, deutet darauf hin, dass das magnetische Moment durch eine Auslenkung der ansonsten antiferromagnetisch geordneten Kupfer-Momente aus der Ebene entsteht. Dieses Verhalten wird durch die Dzyaloshinskii-Moriya-Wechselwirkung (DM) hervorgerufen. Es ist bemerkenswert, dass die Ordnung unabhängig von der Dicke der Kuprat-Lagen stets bei der gleichen Temperatur einsetzt, sogar in Proben mit nur einer einzelnen Kuprat-Lage. In diesen Messungen gibt es keinen Hinweis auf einen zweiten Übergang, der auf eine zusätzliche Ordnung der Nickel-Momente deuten würde.

Um die Untersuchung der magnetischen Ordnung zu komplettieren, wurde der zirkulare magnetische Röntgendichroismus (*engl.* x-ray magnetic circular dichroism, XMCD) an den Kupfer- und Nickel-$L_{2,3}$-Kanten gemessen. Während wir in einem LCO-Dünnfilm ein kleines Signal messen, das auf den Effekt der DM-Wechselwirkung hindeutet, können wir für die Hybridstruktur keinen Dichroismus finden. Dies deutet darauf hin, dass in der Hybridstruktur die Abweichungen von der idealen, tetragonalen Struktur durch Rotationen der Kupfer-Sauerstoff-Oktaeder geringer sind als im dünnen Film, was zu einer Abschwächung der DM-Wechselwirkung und somit zu einem kleineren XMCD-Signal führt, das nicht mehr aufgelöst werden kann. An den $L_{2,3}$-Kanten des Nickels sehen wir ein kleines Signal, dessen Temperaturabhängigkeit magnetische Ordnung anzeigt. Allerdings können wir auf Basis der vorhandenen Daten und deren Analyse die Möglichkeit einer Sättigung der paramagnetischen Momente nicht ausschließen, die zu einem ähnlichen Temperaturverhalten führen würde.

Der elektrische Widerstand der verschiedenen Hybridstrukturen mit unterschiedlichen Dicken der Kuprat- und Nickelat-Lagen ist vorwiegend metallisch. Nur eine Probe mit lediglich zwei Lagen Nickelat ist halbleitend. Proben mit einzelnen Nickelat-Lagen wurden nicht untersucht. Des Weiteren können wir feststellen, dass nicht nur die Nickelat-Lagen zum elektrischen Transport beitragen, sondern auch die Kuprat-Lagen, und das obwohl undotiertes LCO isolierend ist. Ein kleiner, positiver Magnetwiderstand, der weder in $La_{n+1}Ni_nO_{3n+1}$ (mit $n = 2$, 3 oder 4) noch in Bulk-LCO auftritt, weist auf die Möglichkeit schwacher Antilokalisierung (*engl.* “weak antilocalization”, WAL) hin, die typischerweise durch eine Spin-Bahn-Kopplung hervorgerufen wird.

Abstract

Creating interfaces between two different materials often gives rise to effects that do not occur in the isolated bulk versions of the same materials. In addition, confinement in one or more dimensions leads to novel properties of materials. For instance, $LaNiO_3$ (LNO), which is a paramagnetic metal in bulk, exhibits a transition to a weakly insulating, antiferromagnetic state, if it is grown on top of the atomically flat surface of a single crystalline substrate, as soon as the thickness of the single LNO layers is only two unit cells (u.c.) and the LNO layers are sandwiched in between a band insulator, here $LaAlO_3$ (LAO), thereby creating a superlattice (SL). [1, 2] Moreover, the electronic structure of similar SLs, where the thickness of the nickelate layers is reduced to one u.c., resembles that of high-temperature superconductors (HTSC). [3, 4] The prospect of superconductivity has not been fulfilled. Nonetheless, the field has experienced a boom in recent years and the properties of nickelate based SLs and ultrathin films have been studied extensively.

The majority of these samples has so far been grown by magnetron sputtering or pulsed laser deposition (PLD). In the course of this work, we present another deposition technique, namely oxide molecular beam epitaxy (oxide MBE). Its low deposition energy compared to other techniques is expected to give rise to smoother interfaces. Moreover, it is possible to control the deposition of individual atomic layers with MBE in contrast to PLD and sputtering where only the control over one u.c. is given. Exploiting this advantage, it is possible to design novel materials with functional properties. The atomic layer control, however, makes it harder to accurately determine the ratio of the different types of atoms because with reflection high-energy electron diffration (RHEED), which is used as a tool to follow the growth in-situ, it

is not always possible to determine the completion of an atomic layer beyond doubt. Furthermore, the choice of chamber pressures is limited since ballistic transport from the effusion cell to the substrate is required. Pressure is, in addition to temperature, a sensitive parameter to tune the chemical equilibrium and decide whether one or the other phase is formed.

To obtain the desired product in high quality, it is necessary to master the balance of temperature, pressure and stoichiometry. We show, at the beginning of this work, how to grow LNO and SLs thereof in high quality despite its tendency to form oxygen vacancies and impurity phases, in particular the Ruddlesden-Popper phases ($La_{n+1}Ni_nO_{3n+1}$, $1 \leq n \leq \infty$). The majority of samples has been grown on LSAT substrates, a solid solution of $LaAlO_3$ and Sr_2TaAlO_6 which has only a slight lattice mismatch with LNO, and we will focus on these samples in the following.

We compare the properties our samples with known values and nominally identical samples that were grown with PLD and we find indeed a high level of agreement. But the high conductivity and low residual resistivity are remarkable since they exceed any other values reported in literature. [5–8] As expected, the interfaces of MBE samples between substrate and sample as well as between between the different layers are smoother and exhibit less intermixing. In return, the MBE samples contain a higher density of so called 3D-Ruddlesden-Popper faults where a slight nickel deficiency or lanthanum surplus leads to an additional layer of lanthanum oxide and to a shift of all subsequent layers by half a u.c. Furthermore, we observe difference in x-ray absorption lineshapes that are possibly related to the higher interface roughness by changing the chemical environment of the nickel ion. This is accompanied by a difference in the occupation of the e_g-orbitals. While they are degenerate and equally occupied by one electron in bulk LNO – in a simplified picture nickel in LNO has a $3d^7$ configuration – the epitaxial strain caused by the substrate and the confinement of the electrons leads to a preferential occupation of the in-plane $3d_{x^2-y^2}$-orbital. Astonishingly, this orbital polarization is bigger in the PLD samples but can possibly be explained by the different chemical environment of the nickel ion.

The control over single, atomic layers and the smoothness of the interfaces makes it feasible to grow SLs where the LNO layer is only one u.c. thick. We investigated the evolution of x-ray absorption spectra (XAS) with respect to the LNO thickness.

Through reducing the LNO thickness, the lineshape of the spectra undergoes a very similar evolution as the one known from rare earth nickelates (RENiO$_3$, RE = rare earth element, e.g., Pr, Nd, Sm, etc.) with decreasing size of the rare earth ion. In the case of RENiO$_3$, theses changes come along with a transition to a charge-ordered, insulating state. In the SLs, we also observe an increasing localization. In the same time, we observe an increase of orbital polarisation with decreasing LNO thickness. However, its magnitude remains well below the value predicted by theoretical model calculations.

The high quality of our samples, in particular that of one film with a thickness of 25 u.c. (~95 Å) grown on LSAT, enabled us to have a closer look on the temperature dependence of resistivity. These measurements can allow for conclusion on the importance of, e.g., electron-electron interaction and magnetic fluctuations, in the sample. For instance, the resistivity of a Fermi liquid increases quadratically with temperature. In our case, the resistivity scales with 1.8 below 3 K. Above, there is a wide temperature regime without a specific exponent before an exponent of about 1.5 is found above 140 K. This is a sort of behavior that is not predicted by any theory so far.

Afterwards, we studied the temperature and thickness dependence of the charge carrier density. In accordance with literature data for bulk LNO, we find for our thin films and SLs that have at least four consecutive layers of LNO positive charge carriers whose density strongly depends on temperature. [9] Through measurements up to 33 T, we could show by applying a two-band model that a second type of (positive) charge carriers contributes to conductivity at low temperatures. In SLs whose LNO thickness is reduced to two u.c., the charge carrier density is substantially reduce. Remarkably, this is the same thickness where also antiferromagnetic order sets in, indicating a relationship between the two.

Field dependent measurements show an increased resistivity of an LNO film in magnetic field, i.e., a positive magnetoresistance (MR), which is an indication for the high level of oxygen. Simultaneously with a reduction of LNO thickness, the MR is reduced and even becomes negative which is caused by a *weak localization* (WL) of the charge carriers and which is an effect that predominantly occurs in two-dimensional systems. This trend continues gradually until a thickness of three u.c. Below this thickness, the effect of the magnetic field on resistivity increases significantly since

the spins of the antiferromagnetically ordered electrons are aligned in the magnetic field which reduces scattering and therefore reduces resistivity.

In addition to the thickness dependence of the MR, we studied the MR of a 25 u.c. thick film in fields up to 33 T. In the low-field regime, the resistivity increases quadratically with field which reflects a quite normal behavior for metals. Instead of saturating or continuing to grow quadratically, which would be expected for an ordinary metal, the resistivity grows linear with the field without saturating. For metals with a large Fermi surface (FS), this is a highly unusual behavior which can only be explained within the existing theories if one assume a small, additional FS with carriers that have a low mass. Further investigations have to show whether this is indeed the case or whether the linear MR has to be explained in a different way.

In the second part of this thesis, we exploit the control over single, atomic layers, enabled through the use of MBE, to grow novel materials that do not occur in nature and that cannot be grown with any other deposition technique. We have fabricated hybrid structures from La_2CuO_4 (LCO) and $LaNiO_3$. There are always two layers lanthanum oxide in between the LCO and LNO layers such that the structure can be more accurately described as a composition of LCO and the corresponding Ruddlesden-Popper phase, $La_{n+1}Ni_nO_{3n+1}$. The resulting sum formula for these *hybrid structure* is $[(La_2CuO_4)_nLaO(LaNiO_3)_m]_l$, short lx(n//m).

Attempts to grow samples without the additional lanthanum oxide layer in between nickelate and cuprate layers, were not successful. The atomic layers always rearranged in such a way that the cuprate and nickelate layers are always separated by two layers of lanthanum oxide. Hence, we can conclude that copper in direct vicinity of nickel (solely separated by one shared oxygen) is not stable under MBE growth conditions.

The high quality of a single sample – 6x(3//4) – enabled us to measure the positions of oxygen positions in the cuprate and nickelate layers by scanning tunneling microscopy (STEM). The copper-oxygen octahedra as well as the nickel-oxygen octahedra are elongated along growth direction when compared to their lateral dimensions. The elongation of the copper-oxygen octahedra can be explained with the Jahn-Teller distortion. Comparing the measured values with values in bulk LCO, one realizes, however, that the octahedra of the hybrid structures are less elongated. This can only be partially explained with substrate strain. The underlying reasons include a possible

charge transfer across the interface, a higher density of oxygen vacancies or interstitials at the interface or interface roughness. In the case of the nickel-oxygen octahedra, one can distinguish between inner and outer (interfacial) layers. The octahedra at the interface (apical oxygen-oxygen distance = 4.11 Å) are more elongated than the inner ones (apical oxygen-oxygen distance = 3.91 Å). The reason behind is a different coordination of the two nickel ions.

These differences are reflected in XAS spectra. It can be shown that copper is mainly in a +II oxidation state. And the oxidation state of nickel is between +II and +III. In both cases, we observe differences between the samples which are discussed in detail.

The use of linearly polarized light allows to determine the difference in orbital occupation of the in-plane $3d_{x^2-y^2}$-orbitals and out-of-plane $3d_{3z^2-r^2}$-orbitals. Both cases, copper and nickel, show a preferential occupation of the $3d_{3z^2-r^2}$-orbital which is in a close relationship with the elongation of the octahedra observed in STEM.

Measurements of the magnetization with a SQUID magnetometer show a weak ferromagnetism below 165 K in all measured samples. The fact that an LCO thin film shows the same transition indicates that the magnetic moment results from a canting of the otherwise antiferromagnetically ordered copper moments which is induced by the Dzyaloshinskii-Moriya (DM) interaction. It is remarkable that the transition occurs always at the same temperature, independent of the layer thickness and even for samples with a single, isolated cuprate layer. These measurements do not show any sign of a second transition that would indicate an additional ordering of the nickel moments.

To complete the study of the magnetism, we measured the x-ray magnetic circular dichroism (XMCD) at the copper and nickel $L_{2,3}$-edges. While we measure a small signal at the copper edge, indicative of the DM interaction, we do not observe a dichroic signal at the copper edge of a hybrid structure. This difference indicates that the deviations from the ideal, tetragonal structure through rotations of the copper-oxygen octahedra are smaller than in the LCO film which leads to a decrease of the DM interaction and consequently to a smaller XMCD signal which cannot be resolved anymore. At the nickel $L_{2,3}$-edges, whose temperature dependence indicates a magnetic order. However, we cannot exclude a saturation of paramagnetic moments,

which would lead to a similar temperature dependence, based on the data and their analyses at hand.

The resistivity of the hybrid structures with different cuprate and nickelate layer thicknesses is predominantly metallic. Only one sample with only two layers nickelate is semiconducting. Samples with a single nickelate layer have not been studied. We observe that not only the nickelate layers contribute to conductivity but also the cuprate layers albeit undoped LCO is insulating. A small, positive MR, which occurs neither in $La_{n+1}Ni_nO_{3n+1}$ (with $n = 2$, 3 or 4) nor in bulk LCO, indicates the possibility of weak antilocalization (WAL) resulting from spin-orbit coupling.

Chapter 1

Introduction

Modern deposition techniques have made it possible to fabricate extremely thin layers of metal oxides and heterostructures thereof with higher and higher precision. The limit of two-dimensional precision has been achieved by atomic layer-by-layer oxide molecular beam epitaxy (ALL-MBE). Through the accurate control of the shutters in front of effusion cells, which evaporate the metals of interest, it is feasible to deposit one atomic layer at a time onto a single-crystalline and atomically flat substrate surface, thereby justifying the name.

The properties of the novel materials created in this way can differ greatly from any behavior observed in bulk materials. However, the mastery of such a delicate and sensitive technique requires a lot of time and effort.

Therefore, we will describe *in the first part* of this work how to optimize the growth conditions for a class of materials that has been studied extensively in the past and compare nominally identical samples grown by two different techniques, namely ALL-MBE and pulsed laser deposition (PLD). The material system of choice are lanthanum nickelate ($LaNiO_3$, LNO) layers sandwiched between a band insulator (in most cases this will be lanthanum aluminate, $LaAlO_3$, LAO), i.e., LNO-LAO superlattices (SLs).

In the second part, we will show how to exploit the possibilities of ALL-MBE and design new materials. But we will also demonstrate the limits set by the chemical

stability of the intended material. In this case, the material class of choice are hybrid structures consisting of lanthanum cuprate (La_2CuO_4, LCO) and Ruddlesden-Popper (RP) phases of lanthanum nickelate ($La_{n+1}Ni_nO_{3n+1}$, $1 \leq n \leq \infty$).

As an introduction, the following sections will give an overview of nickelates and cuprates. Details on the properties of the band insulators are omitted because they are viewed as spacer materials that are used to confine and separate different layers but are themselves electronically inactive.

1.1 Nickelates

1.1.1 The phase diagram of bulk rare-earth nickelates

The rare-earth nickelates (RENiO$_3$, where RE might not only be a rare-earth ion but could also be a heavy metal, e.g., thallium or bismuth or yttrium) adopt a perovskite (ABO$_3$) structure with nickel on the B site and the RE ion on the A site. While the archetypical perovskite structure is cubic, distortions from the perfect cubic structure arise as soon as the tolerance factor t deviates from one: [10]

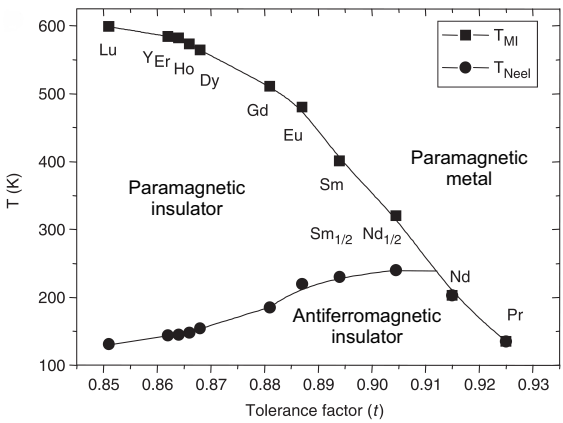

Figure 1.1: The phase diagram of the rare-earth nickelates (RENiO$_3$, RE = Lu, ..., Pr) indicates the temperature of the metal-to-insulator transition (T_{MI}) and the Néel temperature (T_{Neel}) as a function of the tolerance factor (t, Equation 1.1). Reprinted from [10].

$$t \equiv \frac{d_{RE\text{–O}}}{\sqrt{2}d_{\text{Ni–O}}}, \tag{1.1}$$

$d_{RE\text{–O}}$ ($d_{\text{Ni–O}}$) is the ionic bond distance between the *RE* (nickel) ion and oxygen. The tolerance factor is less than one for all nickelates. And the distortions from the ideal, cubic structure grow through rotations of the nickel-oxygen octahedra upon reducing the size of the *RE* ion. This is reflected in the Ni–O–Ni bond angle which would be 180° in the ideal, cubic structure but which is at most 165° as in the case of $LaNiO_3$. [11] The distortions imply a lowering of the symmetry, i.e., $LaNiO_3$ is rhombohedral ($R\bar{3}c$) and all other members of the family are orthorhombic (*Pbnm*). For simplicity, we will use the pseudocubic (*pc*) notation.

Among all members of the rare-earth nickelates, LNO is the only one that remains paramagnetic and metallic upon cooling to lowest temperatures. All other compounds experience a transition to an antiferromagnetic (AFM) insulating state below a certain transition temperature. For rare-earth ions that are smaller than neodymium, an intermediate, paramagnetic and insulating state is observed before AFM ordering sets in at a lower temperature. The corresponding phase diagram as a function of the tolerance factor is shown in Figure 1.1.

There is an ongoing debate about the underlying mechanism of the metal-to-insulator transition (MIT). Experiments find two inequivalent nickel sites below the MIT, leading to a further lowering of the crystal symmetry to a monoclinic space group ($P2_1/n$). [10, 12] The occurrence of the two sites is often attributed to a charge disproportionation into $Ni^{3+\delta}$ and $Ni^{3-\delta}$. But also orbital ordering creating an ionic and a covalent nickel site or bond disproportionation have been suggested. [10, 13]

In the AFM phase, the nickel moments order in a noncollinear fashion where ferromagnetic planes are stacked along the pseudocubic $(111)_{pc}$-direction. Each plane in a set of four shows a different orientation of the nickel moment giving rise to a $(1/4\ 1/4\ 1/4)_{pc}$ propagation vector of the AFM ordering. The averaged nickel moment is close to $1\,\mu_B$ which is in agreement with the expected low-spin $t_{2g}^6 e_g^1$ configuration. Moreover, the magnetic transition occurs at a different temperature than the MIT for all *RE* ions except for praseodymium and neodymium. [10, 14]

1.1.2 Ruddlesden-Popper phases of lanthanum nickelate

Ruddlesden-Popper phases are structures that are derived from the perovskite by inserting an additional AO-layer (here A = La) between the BO_2 planes (here B = Ni) and, resulting in a sum formula of $La_{n+1}Ni_nO_{3n+1}$ ($1 \leq n \leq \infty$). n corresponds to the number of nickelate layers in a perovskite-like stack. The structures are illustrated in Figure 1.2.

While La_2NiO_4 ($n = 1$) with its oxidation state of +II is thermodynamically favored, it is possible to stabilize $LaNiO_3$ ($n = \infty$) in particular at low temperatures or high (oxygen) pressures. But it will decompose into La_2NiO_4 and NiO at high temperatures, which both have an oxidation state of +II.

Moreover, the physical properties change drastically for the different members of this series. For example, $LaNiO_3$ is a paramagnetic metal while La_2NiO_4 is an AFM insulator.

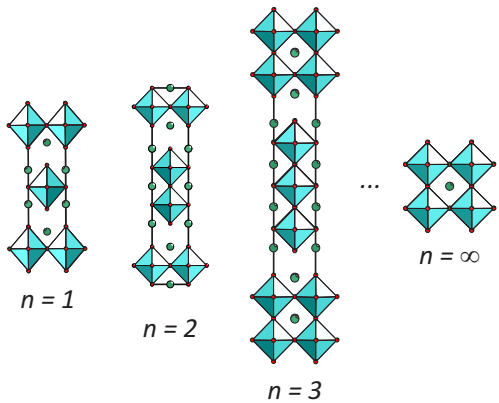

Figure 1.2: The Ruddlesden-Poper series of lanthanum nickelate, $La_{n+1}Ni_nO_{3n+1}$ with $1 \leq n \leq \infty$. Nickel-oxygen octahedra are printed in blue, oxygen atoms in red and lanthanum atoms in green.

1.1.3 Thickness dependence of physical properties in $LaNiO_3$ based heterostructures

It has been predicted that a confinement of LNO to one unit cell (u.c.) thick layers sandwiched between a band insulator, e.g., LAO, would lead to a single-sheeted Fermi surface (FS) which is the essential ingredient for superconductivity. [3, 4] The confinement leads to a reduced hopping along the out-of-plane direction while the electrons remain delocalized in the plane of the layer. This results in a stabilization of the in-plane $3d_{x^2-y^2}$-orbital, thereby inducing an orbital polarization which can be further enhanced by applying tensile strain through using a substrate that has a bigger in-plane lattice constant than LNO.

To date, superconductivity has not been found in LNO-LAO superlattices or other, nickelate based heterostructures. The orbital polarization does not reach the theoretically predicted values that are necessary to produce a single-sheeted FS. Instead, a large hole FS at the corners of the Brillouin zone and a small electron FS at the center of the Brillouin zone are found. [8, 15] The reason behind is the assumption of an inaccurate theoretical model and the experimental difficulties of growing samples with exactly one u.c. thick layers without too much intermixing.

Nonetheless, these predictions stimulated research on dimensionally confined LNO. It was found that epitaxial strain induces orbital polarization with a preferential occupation of the $3d_{x^2-y^2}$-orbital ($3d_{3z^2-r^2}$-orbital) for tensile (compressive) strain. [16, 17] By reducing the thickness of LNO from bulk to one u.c. thick layers, the resistivity increases until an insulating state is obtained. Different values for the critical thickness below which this transition occurs have been reported, ranging from two to about thirteen u.c. [5, 8] Further details on this thickness-induced MIT will be given in Chapter 4.2.

Indeed, the most remarkable observation is antiferromagnetism in SLs where the thickness is reduced to only two u.c. [1, 2] The ordering of the nickel moments is analogous to bulk RENiO$_3$ ($RE \neq$ La), i.e., forming a spin-spiral with a $(1/4\ 1/4\ L)_{pc}$ propagation vector whose tilt pattern can be controlled via the orbital polarization which, in turn, is controlled via epitaxial strain and confinement. [2]

1.2 Lanthanum cuprates

Lanthanum cuprate (La_2CuO_4, LCO) and related compounds, e.g., $YBa_2Cu_3O_7$ (YBCO), are best known for the high-temperature superconducting (HTSC) state that arises when these compounds are doped either with holes or electrons. HTSC was first observed in $La_{2-x}Ba_xCuO_4$ with a superconducting transition temperature (T_c) at about 40 K. [18] Shortly after the discovery of superconductivity in the LCO-system, YBCO was reported to have a T_c as high as 90 K which represents a milestone because it implies that YBCO can be made superconducting by simply cooling with liquid nitrogen. [19]

Besides superconductivity, the members of the big cuprate family display a plethora of quite remarkable phenomena. Depending mostly on doping they show, for instance, antiferromagnetism, charge order, orbital order, a pseudo-gap, a linear scaling of resistivity with temperature or a quadratic scaling of resistivity with temperature. Their connection to HTSC has been studied intensively. However, it remains unclear to date which of the phenomena are essential for superconductivity. [20]

What all of them have in common are two-dimensional copper oxide planes with a spacer layer in between. Moreover, copper in the undoped parent compound has an oxidation state of +II with a $3d^9$ configuration. Due to the large splitting of the e_g-states, the single hole in the d-shell resides to almost completely in the in-plane $3d_{x^2-y^2}$-orbital. The strong Coulomb repulsion in the half-filled $3d_{x^2-y^2}$-band leads to a localization of carriers and the opening of a gap, which is the hallmark of a *Mott insulator*. The Mott insulating state also brings along an AFM ordering of the spins on neighboring copper sites. The AFM correlations are that strong that undoped compounds are already AFM at room temperature. Upon doping (both, hole or electron), the magnetism dies off quickly and superconductivity sets in.

The structure-wise simplest member of the cuprate family is La_2CuO_4 which is therefore an appropriate model system to study the influence of different parameters, like doping and structural distortions, and to try to separate their effect on superconductivity.

Chapter 2

Growth of thin films and heterostructures

2.1 General topics regarding the growth of thin films

Thin films are mostly synthesized by deposition, either via chemical or physical methods. And their properties are extremely sensitive to the method of deposition. This work is focused on the synthesis of complex oxide films and heterostructures by using two deposition methods that both belong to the group of physical deposition methods, namely atomic layer-by-layer oxide molecular beam epitaxy (ALL-MBE; in this work, we will use the abbreviation MBE because no confusion with other varieties of MBE growth are possible) and pulsed laser deposition (PLD). The main difference between the two methods is that in MBE growth, metals are evaporated from effusion cells and are deposited atomic layer by atomic layer whereas in PLD growth, a stoichiometric target material is ablated through the power of a laser. A more detailed description will follow later (Chapters 2.2 and 2.3). Before, we will discuss certain general topics that concern every growth technique, often using examples from MBE- and PLD-growth.

Thin film techniques have made it possible to study the effect of confinement and interfaces. Through confining materials to two dimensions and through creating interfaces in between them, novel phenomena may arise. For example, by bringing the two band insulators $SrTiO_3$ and $LaAlO_3$ together, a two-dimensional electron liquid is

formed that is metallic and even becomes superconducting at very low temperatures, i.e., in the milli-Kelvin regime. [21, 22] With thin film growth it is feasible to manipulate the composition of materials layer by layer, thereby artificially designing novel materials.

Not only the artificial design is of interest. In some cases, e.g., $LaNiO_3$, the bulk material cannot be grown as a large single crystal. In such a case, the growth of the bulk material as a thin film can aid to stabilize the respective compound in a single-crystalline form. For this purpose, a single-crystalline substrate is used that has a similar lattice structure and lattice constant as the material of interest. Then, the structure of the film may follow the structure of the substrate, i.e., grow epitaxially.

Usually, the lattice parameters of the substrate and the material grown on top do not match perfectly in which case the material on top will adapt to the structure of the substrate, resulting in a certain amount of strain, so called *epitaxial strain*. Epitaxial strain acts similar to pressure and it is also of interest to study its effect on the deposited material. Depending on the substrate parameters, the strain can be either compressive or tensile and to quantify its amount the lattice misfit ϵ is used:

$$\epsilon = \frac{a_s - a_f}{a_f} \tag{2.1}$$

where a_s and a_f are the film and substrate lattice parameters that characterize symmetry and bond distances perpendicular to the growth direction, i.e., in-plane. For instance, when growing rhombohedral $LaNiO_3$ ($a = b = 5.4573$ Å, $c = 13.1601$ Å, pseudocubic = 3.84 Å [23]) on orthorhombic $GdScO_3$ ($a = 5.480$ Å, $b = 5.746$ Å, $c = 7.932$ Å, pseudocubic ≈ 3.97 Å [24]) along the (100) pseudocubic direction, one needs to compare the pseudocubic lattice parameters to find the lattice misfit.

In general, thin films can, in principle, also be grown amorphous and polycrystalline and this is actually done, but in the course of this work we consider only films and heterostructures that were grown epitaxially.

Every growth technique has its advantages and disadvantages. One important difference is the kinetic energy with which the particles that are deposited hit the substrate. This energy depends on the process that brings the particles into the gas phase. On the two ends of the energy scale are MBE and PLD growth. In MBE growth metals are thermally evaporated and hence the particles have a very low kinetic energy (~0.1 eV)

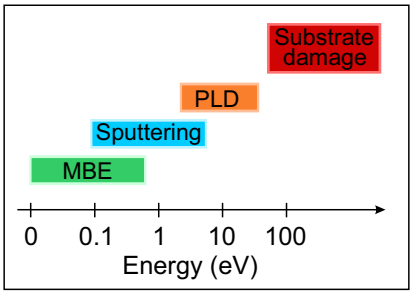

Figure 2.1: Comparison of the kinetic energy of impinging particles for different growth techniques.

whereas in PLD growth particles are evaporated via the power of a laser which results in a plasma plume of highly energetic particles (~10 eV). A pictorial representation of this energy scheme is shown in Figure 2.1. These energy differences obviously have an impact on the growth process and on the samples themselves. Some of these aspects will be discussed in the following.

2.1.1 The interplay of pressure, temperature and stoichiometry

As in any other chemical reaction, thin film growth is subject to the rules of thermodynamics and kinetics. In Figure 2.2 the impact of thermodynamics is schematically drawn for the example of lanthanum nickelates.

For the growth of most oxides, relatively high *pressures* of an oxidant (oxygen radicals, molecular oxygen or ozone) are needed. On the other hand, a high background pressure hinders particles to reach the substrate and sample quality suffers. Because of the high particle energy in PLD growth the pressure can be relatively high, namely up to several hundredth of a millibar. The growth pressure in MBE is limited to about 10^{-4} mbar because a ballistic transport of particles has to be ensured. Molecular oxygen at this pressure (and at the required temperatures) would not be sufficient to obtain the intended oxidation states of the metals of interest. To overcome this issue, ozone has been used which has enough oxidation power to even oxidize silver at room temperature and a pressure of 10^{-5} mbar.

The second important parameter is *temperature*. In general, a high temperature

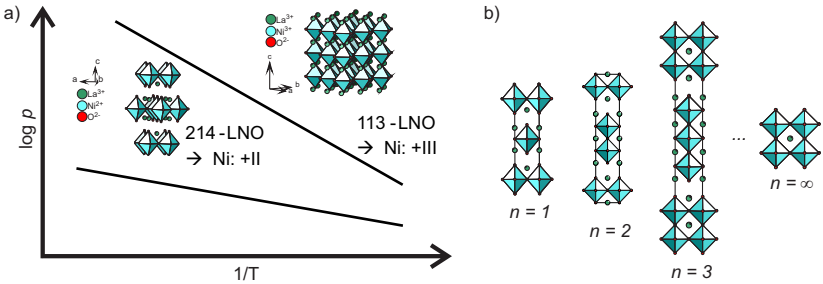

Figure 2.2: a) Sketch of the pressure-temperature phase diagram of lanthanum nickelates. At high temperatures & low pressures La_2NiO_4 (Ni: +II) and at low temperatures and high pressures $LaNiO_3$ (Ni: +III) will be formed. b) Ruddlesden-Popper phases, $La_{n+1}Ni_nO_{3n+1}$, form if stoichiometry is off.

leads to an overall higher crystallinity. On the downside, a high temperature shifts the chemical equilibrium towards the lower oxidation state and either oxygen vacancies form or another, undesired phase becomes more stable. The example of lanthanum nickelates is depicted in Figure 2.2. If one, for instance, aims for $LaNiO_3$ (Ni: +III), and sets the temperature too high, the film will decompose into La_2NiO_4 (Ni: +II) and NiO (Ni: +II). Moreover, the influence of temperature on mobility of adatoms on the surface leads to different growth modes, e.g., island growth or layer-by-layer growth, which are explained in Chapter 2.1.3.

The third parameter that needs to be taken into account is *stoichiometry*. As we will see later in greater detail (Chapter 2.3, the ratio of the different types of atoms in PLD growth is set by a stoichiometric bulk target which in turn determines, with few exceptions, the phase that will be formed. In MBE growth, on the contrary, it is required to control every single atomic layer which leads to a bigger error bar. And a deviation from the optimal ration of the different ions will lead to the formation either of defects (e.g., NiO precipitates) or of other phases (e.g., Ruddlesden-Popper phases in the case of nickelates, see Figure 2.2b).

Another aspect of growth are kinetic effects. While PLD growth is rather fast, MBE growth is rather slow. Therefore, kinetic effects are more important in PLD growth while thermodynamics are more important in MBE growth. As a consequence, metastable phases are likelier to be formed in PLD growth.

2.1.2 RHEED: Reflection high-energy electron diffraction

An important tool to follow the growth process is reflection high-energy electron diffraction (RHEED). In the simplest picture, the atomically flat surface of a single crystal can be viewed as a mirror that reflects an electron beam that is shone upon it resulting in the observation of a specular spot on the detector fluorescence screen. The smoother the surface, the higher the intensity of the reflected beam. One can easily imagine that as soon as atoms are deposited onto the surface the roughness increases and the reflected intensity is reduced. By continuing with the deposition, eventually one layer is filled, the substrate surface is as smooth as before and the intensity of the reflected beam is also back at its origin. This process leads to the observation of oscillations of the reflected intensity and therefore, it is possible to track the deposition of a single layers and to count and choose their number.

High energies of 10–100 keV are used (here: ~25 keV, which corresponds to a wavelength of ~0.1 Å [25]) and the angle of the incoming electron beam should be small, in the order of a few degrees, to ensure surface sensitivity.

Due to the wave character of the electrons, the electron beam is not only reflected but also diffracted. So, instead of a single reflected spot, one sees a diffraction pattern on the detector screen that provides additional information, namely the occurence of diffraction spots that indicate the in-plane symmetry of the substrate or sample. Both, the specular spot and the in-plane diffraction spots are not points in reciprocal space as one is used to from the diffraction pattern from 3D-crystal but through the two-dimensionality these point become rods. Typically, streaky features are observed that arise from imperfections, both caused by the sample as well as through experimental errors. For an example, see Figure 4.4a&b.

During growth surface reconstructions may occur, for example to alleviate a surface polarity. The occurrence of these reconstructions in a regular pattern on the surface will lead to the formation of additional streaks. For an example, see Figure 5.3c&d.

If large enough three-dimensional defects form during growth, e.g., through an outgrowth of a secondary phase, additional spots appear. Such an effect can be seen, for example, in Figure 4.3a, where a surplus of nickel was deposited, leading to an outgrowth of NiO precipitates.

Additional complexity arises from the fact that electrons are not only diffracted

through a single scattering event (kinematic scattering). Due to their strong interaction with matter, electrons often undergo a series of scattering events before they escape the substrate (dynamical scattering).

The complexity of the growth and the scattering process that the simple picture drawn in the beginning is not quite true, namely the maximum intensity does not necessarily correspond to one full atomic layer. In fact, almost the opposite might be the case as was shown in Reference [26].

2.1.3 The different growth modes of thin films

Depending on substrate temperature and on the strength of the chemical bonds between adatoms and substrate, different growth modes can occur. One can distinguish between four different growth modes: [27]

At low temperatures and when the adatoms are strongly bound to each other, stronger than to the substrate, the atoms form islands. This growth mode is called *island growth* or *Volmer-Weber growth*. The formation of these islands makes the surface rougher and rougher and the intensity of the specular spot in RHEED decreases.

If the temperature is very high and the adatoms are very mobile on the surface, they will immediately move towards surface steps on the substrate. These positions are thermodynamically favored because the adatom has less dangling bonds than on a terrace. In this so-called *step-flow growth* no RHEED oscillations are observed but the reflected intensity remains high because the surface remains smooth.

Moreover, in *layer-by-layer* or *Frank-van der Merwe growth*, which occurs at intermediate temperature and if the bonds between adatoms and substrate are stronger than between each other, the energy of the adatoms is high enough that islands dissolve, but the atoms are not mobile enough to move to the next step. This is the picture drawn in the beginning of the description of the RHEED process (Chapter 2.1.2) and RHEED oscillations are observed. This is the ideal case to control the deposition of single layers.

Finally, a combination of growth modes may occur. In *Stranski-Krastanov* or *layer plus island* growth, the first layer or the first few layers grow in a layer-by-layer fashion and afterwards, islands start forming.

2.1.4 The substrate surface and its alteration

Not only do the properties of thin films and interfaces differ from bulk behavior, but it is the same for the structure and the properties of a crystal surface.

Substrates for thin films growth are cut along certain crystallographic planes. The most common one in the case of a cubic perovskite is the (100) plane which is a cut along a face of the unit cell. All samples that were grown in the course of this thesis project were grown on substrates that were cut along the (100) plane or along the corresponding plane in the case of a non-cubic substrate. For example, in the case of $GdScO_3$ the (110) plane corresponds to the $(100)_{pc}$ plane where the index *pc* denotes pseudocubic notation.

These cuts are never perfect but there is an angle between the substrate surface and the crystallographic plane. This angle is called *miscut angle* and is typically 0.1° or less in the case of the substrates used for this thesis project. The miscut gives rise to the occurrence of terraces and steps whose topology can be mapped by atomic force microscopy (AFM).

In as-received substrates, these steps are not smooth and well-defined but they are jagged. Smooth steps and terraces are thermodynamically preferred because of the fewer dangling bonds. Hence, at high temperatures, when the mobility of the surface atoms is high enough, these defects will heal and smooth steps and terraces are formed.

Moreover, the chemical composition of the surface is not well defined. Both A and B site cations are found at the surface. For certain substrates, a procedure exists to etch away one type of atom selectively and to obtain well defined surfaces. In general, such procedures are possible if either the A or the B site cation has a higher solubility in the etching solution. In the following, we will briefly describe the so-called *substrate termination* in the case of $SrTiO_3$ (STO) and $GdScO_3$ (GSO).

$(LaAlO_3)_{0.3}(Sr_2TaAlO_6)_{0.7}$ (LSAT) substrates that were used to grow samples for this thesis project were used as received. They were neither annealed nor etched. Nonetheless, sample quality was still satisfactory.

$SrTiO_3$ termination

A termination procedure that selectively etches strontium was developed by Koster *et al.* [28] Following their steps, the as-received substrate is thoroughly cleaned and immersed in purified water in an ultrasonic bath for 30 min. This step forms strontium hydroxide at the surface which can subsequently be removed if the substrate is dipped into buffered HF for 30 sec. Afterwards, the residuals of this etching process are carefully removed by washing the substrate with purified water. Then, the substrate is annealed at 1050°C for 1–2 h to achieve smooth steps and terraces.

$GdScO_3$ termination

Kleibeuker *et al.* [29] developed a method to obtain a scandium-terminated surfaces of the rare earth scandates. Here, we will explain the procedure for the case of GSO but, in principle, it works for all scandates.

The as-received substrate is first annealed at 1000°. Afterwards, the substrate is immersed for 1 h in a 12 M sodium hydroxide solution and washed with 1 M sodium hydroxide. Subsequently, it is rinsed with water.

Note, that in the case of rare-earth scandates, the substrate is first annealed and then etched. The reason behind is that at 1000°C, diffusion within the GSO substrate is already that high that a mixed-termination would appear otherwise.

2.2 Oxide MBE: Oxide molecular beam epitaxy

The MBE set-up that was used to grow the samples investigated in the course of this work is described in great detail in Reference [30] and a simplified sketch is shown in Figure 2.3. In this section, we will just briefly describe the certain aspects of the growth procedure.

After the annealing and etching procedure described in 2.1.4, the substrates were thoroughly cleaned through immersion in acetone and isopropanol each for 5 min in an ultrasonic bath. The insulating substrates are almost colorless. During growth they will be heated by radiation and backside-coating is needed to enable absorption of light and efficient heating. Therefore, the substrates' backsides were painted with

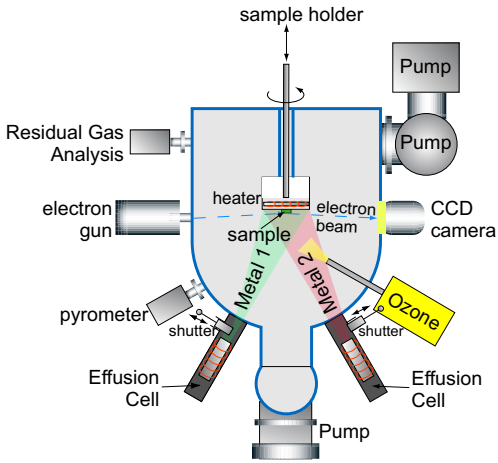

Figure 2.3: Simplified sketch of the MBE system. Reproduced from Reference [30].

$SrRuO_3$ powder, dissolved in isopropanol, which is black.

The substrates were fixed to a sample holder with tantalum wire and loaded first into the load lock where they are annealed at ~120°C in vacuum (~10^{-7} mbar) to remove carbon contamination ant residual water. Then they were transferred to the growth chamber and heated to growth temperature (usually between 500 and 650°C).

Before growth, the fluxes of the effusion cells were calibrated with a quartz crystal microbalance (QCM) which measures the mass of the deposited atoms per time through shifts of its resonance frequency which can be measure with a high accuracy. Nonetheless, uncertainties remain because, for instance, the measured frequency is very sensitive to small vibrations caused by, e.g., the opening an closing of a shutter. Therefore, we started the data acquisition about one minute after the shutter was opened and averaged over two minutes. One issue is that, while the shutter in front of an effusion cell is closed, gas may build up which is released upon opening the shutter. The effect is similar to a pot of boiling water upon lifting the pot's lid and leads to uncertainties in flux calibration since the time during which this extra amount of material is released is not covered by the calibration with the QCM. To reduce this effect and the resulting uncertainty, low deposition rates and long shutter opening times are

needed.

The ozone used to oxidize the metals during sample growth was produced with an ozone generator. The ozone was collected in an insulated still where it was kept in the liquid state through cooling with liquid nitrogen. The still temperature was adjusted with a combination of heating and cooling such that a certain vapor pressure builds up and ozone is delivered into the growth chamber. The pressure in the growth chamber (~10^{-6}–10^{-5} mbar) can be controlled via the vapor pressure (~500–650 mbar). The chamber pressure may not exceed 10^{-4} mbar to ensure ballistic transport from the effusion cells to the substrate surface. The high oxidation power of ozone enables to achieve high oxidation states in the deposited metals.

Ten effusion cells are attached to the chamber, enabling, in principle, the deposition of ten different metals. Their design depends on the temperature range needed for evaporation. For the evaporation of nickel, for example, most of the time an alumina crucible was used that was heated with a single filament. The shutters in front of the cells are controlled electronically to achieve high accuracy in layer-by-layer deposition.

The temperature of the sample is measured with an infrared radiation pyrometer. Moreover, a thermocouple is close to the heating element.

In addition, a mass spectrometer (residual-gas analyzer, RGA) is attached to the chamber to enable tracking of the gas mixture in the chamber. It aids, for instance, in discovering leaks or issues related to the ozone delivery.

2.3 PLD: Pulsed laser deposition

All PLD samples that were grown as a part of this thesis project were grown by Georg Christiani in collaboration with the Technology Group at the MPI-FKF in Stuttgart. A simplified sketch of the growth chamber is shown in Figure 2.4.

Instead of evaporating metals from separate metal sources, the ablation of the stoichiometric target material upon laser irradiation and creation of a plasma plume is used in the PLD growth process. The process of the plasma creation is very complicated, however, under optimized conditions it is sufficient to consider the growth process as a simple transfer of the target material towards the hot substrate where the

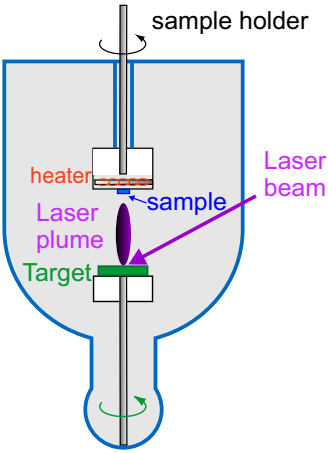

Figure 2.4: Simplified sketch of a PLD system.

oxide film starts to grow in an epitaxial manner.

In our work, we have used stoichiometric targets of, e.g., $LaNiO_3$ and $LaAlO_3$. The growth conditions and their optimization are described in Chapter 4.3.

Chapter 3

Characterization of thin films and heterostructures

3.1 X-ray techniques

X-ray light comprises electromagnetic radiation with a wavelength of about 0.1–100 Å which corresponds to energies of about 100 eV–100 keV. X-rays are grouped into two regimes, i.e., into hard x-rays from about 5 to 10 keV and soft x-rays below 1 keV. They interact with matter which enables the use of x-rays to study material properties in different ways. Two of such characterization techniques will be described here, namely hard x-ray diffraction and soft x-ray absorption.

3.1.1 XRD: Off-resonant x-ray diffraction

The wavelength of hard x-rays is in the order of typical atomic distances which gives rise to regular diffraction patterns if these atoms are on a regular lattice. The arrangement of the atoms can be determined from the measurement of the positions and intensities of spots where the x-rays interfere constructively, so called Bragg reflections. These conditions are met for the following condition (*Bragg's law*): [31]

$$2d \cdot \sin(\theta) = n \cdot \lambda, \tag{3.1}$$

where d is the spacing between lattice planes, θ is the angle between the set of parallel lattice planes and the incoming beam, n is an integer and λ is the wavelength. And one will pick up a signal with a detector at an angle $2 \cdot \theta$ between incoming and outgoing beam.

The intensity depends on the crystal symmetry and on the atoms the crystal is made of. To obtain these intensities, the reader is referred to the standard textbooks, for example Reference [32].

Diffraction patterns are often given in terms of the wavelength-independent scattering vector $\vec{q}$ whose absolute value is given by the following equation:

$$Q = \frac{4\pi}{\lambda} \sin(\theta) = \frac{2\pi}{d} \tag{3.2}$$

The components of the scattering vector in the three dimensions (q_x, q_y and q_z) are given via:

$$q_x \cdot a = 2\pi h \tag{3.3}$$

$$q_y \cdot b = 2\pi k \tag{3.4}$$

$$q_z \cdot c = 2\pi l \tag{3.5}$$

where a, b and c are the dimensions of the unit cell (u.c.) and h, k and l are the reciprocal lattice units (rlu). If there is no systematic extinction of a reflection due to the Laue conditions, [32] a peak will be found for integer numbers of h, k and l. In this thesis, diffraction patterns are plotted either in terms of $1/d$, which gives direct access to distances between the planes, or in reciprocal lattice units of the substrate.

To correct for a series of systematic measurement errors when determining the size of the unit cell, the *Nelson-Riley* fit is used: [33]

$$f(\theta) = \frac{\cos^2(\theta)}{\theta} + \frac{\cos^2(\theta)}{\sin(\theta)} \tag{3.6}$$

where the angles θ correspond to peak positions. If one plots the apparent lattice parameter d as determined from Equation 3.1 against $1/2 \cdot f(\theta)$ and fits a linear slope

to the data, the intercept gives the desired lattice parameter.

Another important parameter of single crystals is their *mosaicity*. In a perfect crystal with infinite dimensions where the lattice planes across the whole crystal are exactly parallel, the diffraction peaks will have zero width (the peak width would be determined by the experimental resolution in this case). The finite size of a real crystal gives rise to a broadening of the peak. Moreover, domains occur in a real crystal that are tilted with respect to each other, resulting also in a broadening of the diffraction peak. The width of the peak measured by moving the angle θ at fixed detector angle, 2θ, through the peak gives the *mosaicity* and such a scan is called a *rocking* curve.

The finite size of thin films and superlattices gives rise to certain features in the diffraction pattern. A summary is depicted in Figure 3.1. First of all, the Bragg peaks are broad in the direction of truncation. Moreover, the observed fringes are called *Laue fringes* and as indicated, their width is directly connected to the total thickness of the film superlattice (SL). In case of a SL, SL Bragg reflections can be observed

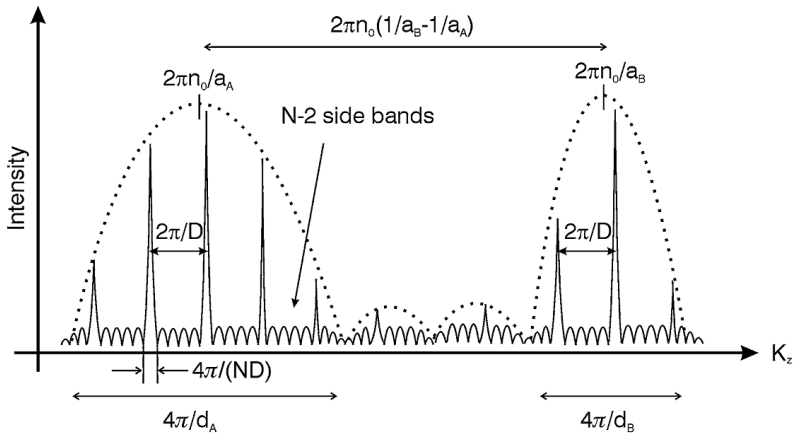

Figure 3.1: Theoretical diffraction pattern of a superlattice (without substrate) consisting of two materials, A and B, where K_z is the scattering vector in z-direction (corresponding to q_z as defined in Equation 3.5). d_A and d_B are the thicknesses of layer A and B. $D = d_A + d_B$ is the bilayer thickness. N is the number of repetitions of the bilayer. n_0 is the Miller index of the measured peak (corresponding to l in Equation 3.5). a_A and a_B are lattice constants of material A and B. ©Springer-Verlag Berlin Heidelberg 2015 [34]

corresponding to the periodicity of the superstructure.

In contrast to the example in Figure 3.1, the lattice constants of the two constituents of our SLs are almost equal (or we have a heterostructure where the lattice parameters of its constituents are not resolved). As a consequence, the diffraction pattern will be simplified in the following way: the two envelopes, indicated by the dotted lines in Figure 3.1, whose maxima correspond to the lattice parameters a_A and a_B, will overlap such that their center will correspond to the average lattice parameter $a = (a_A + a_B)/2$. For an example, see Figure 4.6.

Figure 3.1 shows the diffraction pattern of the SL alone. In fact, the substrate underneath the SL also contributes to the diffraction pattern. First of all, the substrate is a high-quality single crystal and therefore it will show sharp Bragg peaks in addition to the SL peaks. Furthermore, the smooth and abrupt surface of the substrate gives rise to a *crystal truncation rod*. The measured film peaks can interfere with the rod contribution. The film peak, just by itself, is often too weak to be measured with the standard, in-house diffractometers. Synchrotron radiation with its orders of magnitude higher intensity reveals the film peak in its full extent. The consequence is that a measurement of the film peak width to determine the mosaicity can be misleading if it is interfering with the rod and not measured at a synchrotron.

A particular application of x-ray diffraction is x-ray reflectivity (XRR) where one measures the x-ray intensity that is reflected from the surface of the sample at very low angles, starting at 0°. Below the *angle of total reflection*, the full intensity of the x-ray beam is reflected as the name implies. Above, oscillations of the intensity, due to the interference between x-rays scattered from the substrate-film interface and the surface, set in and in analogy to what was discussed above, the film thickness t can be determined via the following equation: [34]

$$\sin(\theta_m) = \frac{m \cdot \lambda}{2t} \tag{3.7}$$

An example is given in Figure 4.7.

High resolution XRD and XRR measurements were routinely performed using a four-circle diffractometer with a Cu K_α source. Selected measurements were performed at the MPI-MF Surface Diffraction beamline of the ANKA light source of the Karlsruher Institute of Technology in Germany. The use of the Mythen detector

(line detector) in both cases enabled the fast measurement of reciprocal space maps (RSM). [35]

3.1.2 XAS: X-ray absorption spectroscopy

The energy of x-rays is in the same range as the energy needed to excite a core electron into an empty state above the Fermi level (FL). In particular, soft x-rays in the range from about 400 to 1000 eV correspond to energies required for transitions from $2p$- into $3d$-states (the so called L-edge, see Figure 3.2) which are of great interest in the study of first-row transition metals and their compounds, among them the materials investigated in the course of this work. [36]

The sudden possibility for an electron to be excited into an empty state upon scanning the energy from below to above the threshold energy gives rise to an *edge jump*. The threshold energy corresponds to the binding energy of the core state. Due to spin-orbit coupling, the $2p$-states are split into $2p_{3/2}$ and $2p_{1/2}$ states, resulting also in two

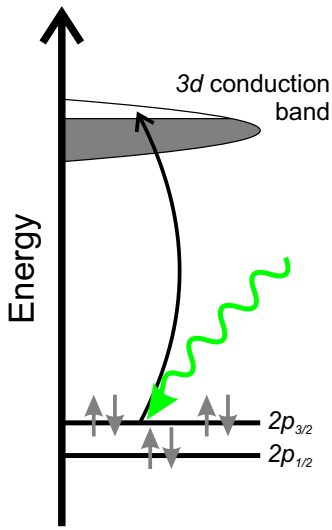

Figure 3.2: Sketch of an x-ray (green arrow) induced transition from the $2p$ orbitals into empty states of the $3d$ conduction band, i.e., the transition corresponding to the $L_{2,3}$-edges.

absorption edges, the L_2- and L_3-edges.

Within the *single electron approximation*, one electron that does not interact with other electrons or with the core-hole is excited into an empty state and the absorption spectrum reflects the *site and symmetry projected unoccupied density of states*.

This picture fails if the final state experiences strong electron-electron (strongly correlated or localized states) or electron-core interactions which is the case, among others, for all systems that have a partially filled 3*d*-shell in the final state. The strong interactions lead to *multiplet splitting*. [37]

Cluster calculations, which typically consider one metal atom surrounded by its ligands, take these interactions into account. This approach results in a very local picture and consequently they do not accurately reproduce the spectra of delocalized systems, i.e., metals. For insulators, e.g., NiO, [38] cluster calculations agree well with measured spectra. [39]

Experimentally, absorption can be detected in several ways. The most direct way is to measure *transmission* and compare the intensity of the x-ray beam before and after it has passed the sample. In our case, this procedure is not feasible because soft x-rays are attenuated quickly and no signal due to absorption of the x-rays by the substrate, no signal would be measured. Samples measured in transmission need to be very thin, i.e., in the order of a few hundred nanometer. [36]

Instead, one can probe the decay of the core-hole that was created in the absorption process in different ways. In the course of this work *total electron yield (TEY)* and *fluorescence yield (FY)* were used.

When an electron escapes the sample after being excited, the created hole will be filled with an electron through electrical contacts on the sample. This process gives rise to a current – the *total electron yield (TEY)* – that can be accurately measured and that is proportional to absorption. Because of the strong interaction of electrons with matter, electrons cannot escape from the bulk of the sample. They can only escape from the sample surface, i.e., typically a depth of about 30–100 Å which results in a high surface-sensitivity of the TEY.

The core-hole can also decay via the emission of fluorescent light. The light picked up with a detector is the *fluorescence yield (FY)*. Since the incoming and the outgoing photon have similar mean free paths, FY is bulk sensitive. On the other hand, self-

absorption effects can occur which distort the lineshape of the spectra. Moreover, if multiplets are present, the fluorescent decay process is not simply proportional to absorption anymore. [37]

Electron energy loss spectroscopy (EELS) is another, yet completely different technique that gives information about these atomic transitions. In EELS, the energy that is lost while electrons of 100–300 keV are transmitted through a very thin sample is studied in transmission electron microscopy (TEM).

XLD: X-ray linear dichroism

If the spherical symmetry of an atomic site is broken by magnetic or crystalline electric fields, dichroism can arise. That is, light with different linear or circular polarization will result in different absorption spectra. Magnetic fields can give rise to circular and linear dichroism whereas electric fields can only give rise to linear dichroism. First, we will discuss linear dichroism caused by an anisotropic electric field before we turn towards linear dichroism caused by a magnetic field and towards circular dichroism.

Taking the e_g-states of a transition metal in an octahedral ligand field as an example, one can explain XLD in the following way: If the electric field of the incoming x-ray light at resonance with the L_2- or L_3-edge points into z-direction, only transitions into the $3d_{3z^2-r^2}$-orbital will be probed. On the contrary, mainly $3d_{x^2-y^2}$-states will be probed if the electric field lies in the xy-plane. However, since the $3d_{3z^2-r^2}$-orbital also has some probability density in the xy-plane, transitions into the $3d_{3z^2-r^2}$-orbital are also allowed, although at a lower probability than transitions into the $3d_{x^2-y^2}$-orbital. The sum-rule for linear dichroism quantifies these dependencies, resulting in the ratio of the number of holes in the $3d_{3z^2-r^2}$-orbital and the $3d_{x^2-y^2}$-orbital, X_{ave}: [16, 40]

$$X_{ave} = \frac{h_{3z^2-r^2}}{h_{x^2-y^2}} = \frac{3I_z}{4I_x - I_z} \tag{3.8}$$

where $h_{3z^2-r^2}$ and $h_{x^2-y^2}$ are the number of holes in the respective orbitals and I_z and I_x are total integrated intensities $\int_{L_{3,2}} I_{x,z}(E)dE$ for in-plane (x) and out-of-plane (z) polarization, respectively. For a more general expression, see Reference [40].

Based on X_{ave}, one can calculate the often used orbital polarization P, if the number of electrons in the e_g-states, n_{e_g}, is known:

$$P = \frac{n_{x^2-y^2} - n_{3z^2-r^2}}{n_{x^2-y^2} + n_{3z^2-r^2}} = \left(\frac{4}{n_{e_g}} - 1\right)\frac{(X_{ave} - 1)}{(X_{ave} + 1)} \tag{3.9}$$

where $n_{3z^2-r^2}$ and $n_{x^2-y^2}$ are the number of electrons in the respective orbitals. For the perovskite-type nickelates n_{e_g}, we set it to one. For a discussion on this topic, see Reference [17].

XMLD: X-ray magnetic linear dichroism

The ordering of magnetic moments along a preferential magnetic axis in an antiferromagnetic material leads, via spin-orbit coupling, to a charge anisotropy which, in turn, gives rise to linear dichroism. The maximum XMLD signal is obtained if one compares measurements with the electric field parallel and perpendicular to the magnetic axis. The magnitude of this effect scales quadratically with the magnetization but it is often small in 3*d*-metals because the spin-orbit coupling is small and the band width large. The occurrence of multiplet effects, however, enhances the XMLD signal. [41]

Moreover, the lineshapes of the absorption spectra are sensitive to the magnitude of the exchange field. As a consequence, spectral weight is transferred from one multiplet peak to another which does not depend on the direction of the electric field and is therefore also observable in the isotropic spectra. [42]

The effects of XMLD caused by magnetic ordering and XLD caused by crystal field effects add to each other. To distinguish between the two, usually a temperature dependence of the spectra is taken across the Néel temperature.

XMCD: X-ray magnetic circular dichroism

A net ferromagnetic moment can be measured with XMCD. Here, (left or right) circularly polarized light couples to the polarization of the spins. By either switching the polarization or the external magnetic field, dichroism is observed whose magnitude is proportional to the magnetic moment. Sum rules can be used to determine the spin (S_Z) and orbital (L_Z) contributions to the magnetic moment. Their ratio is given via: [43]

$$\frac{\langle L_Z \rangle}{\langle S_Z \rangle} = \frac{4}{3} \frac{\int_{\text{edge}} (\sigma^+ - \sigma^-)}{\int_{L_3\text{edge}} (\sigma^+ - \sigma^-) - 2 \int_{L_2\text{edge}} (\sigma^+ - \sigma^-)} \tag{3.10}$$

where σ^+ and σ^- correspond to the intensities measured with right or left circularly polarized light, respectively.

XMCD is mainly used for the study of ferro- and ferrimagnetic materials. But also antiferromagnetic materials can be studied if they have a canted moment. [44]

Experimental details

All XAS measurements for this thesis project were performed at BESSY II in Berlin, Germany either at UE56/2-PGM1 or at UE46-PGM1 soft x-ray beam line.

All XAS spectra with linearly polarized light were measured at an angle $\theta = 30°$ between the sample and the incoming light (see Figure 3.3). In this geometry, σ-polarization corresponds directly to intensity with the electric field being in-plane, e.g., E ∥ x (we do not distinguish between x and y or their diagonal, i.e., we assume that our samples are isotropic in the sample plane), but the intensity measured with π-polarized light needs to be corrected in the following way to obtain the intensity for E ∥ z, I_z:

$$I_z(E) = {}^4/_3 I_\pi(E) - {}^1/_3 I_x(E) \tag{3.11}$$

where $I_\pi(E)$ is the intensity measured with π-polarized light and $I_x(E) = I_\sigma(E)$ is

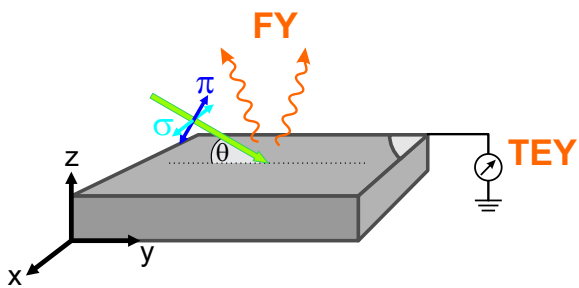

Figure 3.3: Sketch of measurement geometry for the measurement of x-ray linear dichroism.

the intensity measured with σ-polarized light.

In our spectra taken at the nickel $L_{2,3}$-edges, we face the problem that the L_3-edge overlaps with the intense lanthanum M_4-line. Therefore, we fitted the latter with a Lorentzian which we then subtracted from the spectra. All nickel spectra in Chapters 4 and 5 are shown after subtraction of the Lorentzian. Figure 3.4 shows the spectrum of a $LaNiO_3$-film before the subtraction where the tail of the fitted Lorentzian is drawn with a red, dashed line. [16, 17] For a more detailed description of this procedure and its related errors see Reference [45].

3.2 Electrical transport

3.2.1 Basics of transport measurements

The current density, i.e., the flow of charge carriers in a given volume, induced by an electric field is proportional to the latter and the constant of proportionality is the electrical resistivity, ρ. The resistivity is a parameter that characterizes the measured material. Microscopically, one measures the scattering of charge carriers which hinders the flow of current and causes resistivity. The average time between two scattering events of a charge carrier is the relaxation time, τ. And the inverse of resistivity is the conductivity σ which can be written, in its simplest version, in the following way: [32]

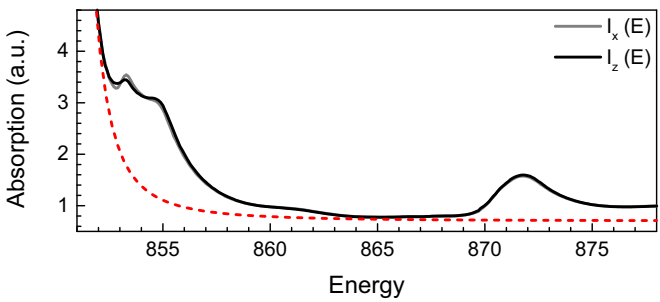

Figure 3.4: Exemplary XAS spectrum of an $LaNiO_3$ film on LSAT substrate measured with linearly polarized light in TEY mode. The dashed red line shows the result of a Lorentzian fit to the La M_4 line.

$$\sigma = \frac{1}{\rho} = n\, e\, \mu = \frac{n\, e^2\, \tau}{m^*} \tag{3.12}$$

where n is the charge carrier density, μ their mobility and e the elementary charge and m^* the effective mass, which is equivalent to the mass of an electron in free electron model. If different charge carriers with different mobilities are present in a material, the conductivity can be written in a more general way: [46]

$$\sigma = e \left(\sum_i n_i\, \mu_i \right) \tag{3.13}$$

where n_i and μ_i are the density and mobility of charge carrier i.

The measurement of resistivity enables to draw conclusions on the electronic structure of a material. The simplest distinction is that between an insulator and a metal. Insulators have a high resistivity that decreases upon increasing the temperature whereas metals have a low resistivity that increases upon increasing temperature. Besides, there are many more implications, applications and theoretical models. Few of them will be discussed within the current chapter others in Chapters 4.2, 4.5, 4.6 and 5.3.3.

To measure resistivity, we used the *van-der-Pauw geometry* in which it is possible to determine the sheet resistance of an arbitrarily shaped, two-dimensional sample. [47] In our case, platinum contacts were sputtered onto the corners of the square-shaped samples and a current is applied while the voltage is measured according to the geometry shown in Figure 3.5. Usually, a measurement of the two indicated resistances R_1 and R_2 is sufficient. For an accurate measurement, the current direction is inversed,

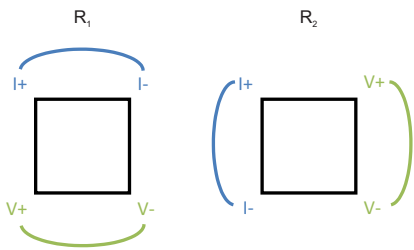

Figure 3.5: The two configurations of the resistivity measurements after *L. J. van der Pauw*. [47]

voltage and current are exchanged and the average of the four values obtained in such a way gives R_1 and R_2, respectively. The sheet resistance, R_S, can then be determined via the following equation:

$$e^{-\pi R_1/R_S} + e^{-\pi R_2/R_S} = 1 \tag{3.14}$$

which can also be written as:

$$R_S = \frac{\pi}{\ln 2} \frac{R_1 + R_2}{2} \cdot f(R_1/R_2) \tag{3.15}$$

or in terms of ρ:

$$\rho = \frac{\pi \cdot t}{\ln 2} \frac{R_1 + R_2}{2} \cdot f(R_1/R_2) \tag{3.16}$$

where t is the film thickness and f is a correction function that can be obtained from tables, e.g., from Reference [48]. For $R_1 = R_2$, f is equal to one.

To obtain accurate results from measurements in van-der-Pauw geometry, one has to take care that the contacts are at the edges of the sample, the contacts are small compared to the dimensions of the sample, the thickness of the sample is homogenous and that the sample does not have isolated holes. [47]

Practical notes:

Most measurements were conducted with a Quantum Design Physical Property Measurement System (PPMS) in temperatures ranging from 2–300 K and fields from 0–9 T. The contact resistance, which is approximately the four-point-resistance (R_1 or R_2) subtracted from the two-point-resistance measured by a multimeter between two contacts ($R_{contact} = R_{two-point} - R_{four-point}$), was routinely checked. The measurement current was set as high as possible without heating the sample, in particular at low temperatures. Therefore, the resistance was measured while varying the current. The AC mode in the resistivity option should be preferred to DC mode. In AC mode, the frequency is so low that, in principle, the same is measured as in DC but the noise in the measurements is reduced.

3.2.2 Magnetotransport

Hall measurements

If a magnetic field ($\vec{B} \parallel$ z, B_z) is applied perpendicular to the current direction ($I \parallel$ x, I_x), the trajectories of the charge carriers are bent due to the Lorentz force, which gives rise to a *Hall voltage* in y-direction, V_y, and the corresponding resistance, $\rho_{xy} = V_y/I_x$.

We define the Hall resistance ρ_{H} as:

$$\rho_{\mathrm{H}} = \frac{\rho_{xy}(+B) - \rho_{xy}(-B)}{2} \tag{3.17}$$

The above correction is necessary to correct for the contribution of magnetoresistance to the Hall resistance in van-der-Pauw-geometry.

In analogy to the measurement of the sheet resistance discussed above the measurement can be improved through inversion of current direction and exchange of voltage and current and subsequent averaging over all obtained values. A sketch of the two measurement geometries is shown in Figure 3.6.

Typically, the Hall resistance is measured as a function of the field, B. Then, the Hall coefficient, R_{H}, is obtained from:

$$R_{\mathrm{H}} = t \cdot \frac{\partial \rho_{\mathrm{H}}}{\partial B} \tag{3.18}$$

where t is the sample thickness. The sign of the Hall coefficient indicates whether the charge carriers are holes (positive) or electrons (negative). If only one type of

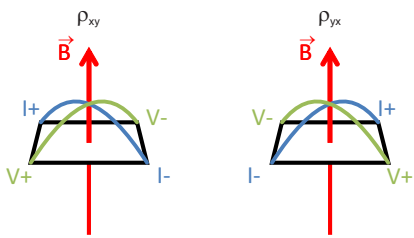

Figure 3.6: The two configurations for Hall resistance measurements in van-der-Pauw-geometry. [47]

charge carrier contributes to conductivity, R_{H} is constant and the charge carrier density n is:

$$n = \frac{1}{R_{\mathrm{H}} \cdot e} \tag{3.19}$$

Whereas metals typically have a carrier density that is constant with temperature, the carrier density of semiconductors and insulators increases with temperature due to thermal excitations into the conduction band.

If different types of carriers contribute to conductivity, the Hall coefficient is not constant in field anymore and the charge carrier densities cannot be extracted in a straightforward manner. There are models, however, that can be fitted to the data to obtain the individual densities, for example the *two-band model in 2D*. [49]

One can consider two bands (or two different groups of electrons) with n_i, μ_i, and τ_i where the latter is isotropic and constant and where interband transitions are not allowed. Moreover, it is assumed that the contributions to conductivity from each band simply add. [49] In such a case, the Hall resistance can be written as:

$$\rho_{\mathrm{H}} = \frac{B}{e} \frac{(\mu_1^2\, n_1 + \mu_2^2\, n_2) + (\mu_1\, \mu_2\, B)^2 (n_1 + n_2)}{(\mu_1 |n_1| + \mu_2 |n_2|)^2 + (\mu_1\, \mu_2\, B)^2 (n_1 + n_2)^2} \tag{3.20}$$

In the limiting case for infinitely large fields, one obtains:

$$\lim_{B \to \infty} \rho_{\mathrm{H}} = \frac{B}{e\,(n_1 + n_2)} \tag{3.21}$$

The drawback of this model is the number of adjustable parameters that allow a fit with reasonable parameters in almost any case. [49] To reduce the ambiguity of the mode. it is advisable to simultaneously fit the resistivity in zero field:

$$\rho_{xx,0\mathrm{T}} = \frac{1}{e\,(\mu_1\, n_1 + \mu_2\, n_2)} \tag{3.22}$$

Magnetoresistance

Besides inducing a Hall voltage, a magnetic field can also alter the resistivity itself, giving rise to magnetoresistance (MR). According to the free electron model, there should be no MR at all. [50] However, simply assuming a second type of charge

carrier is enough to obtain MR. [49] In a thin film or heterostructure, three geometries should be considered when measuring MR. They are sketched in Figure 3.7 for the van-der-Pauw-geometry.

In a material with an approximately spherical FS, the trajectories of the electrons will describe helices whose axes are parallel to the magnetic field. The corresponding angular velocity, ω_c, is given by: [50]

$$\omega_c = \frac{e\,B}{m^*} \tag{3.23}$$

Multiplied with the scattering time, τ, one obtains the mean angle by which an electron has turned in between two collisions:

$$\omega_c\,\tau = \frac{B\,\sigma_0}{n\,e} \tag{3.24}$$

In metals with a more complicated FS, the trajectories do not describe helices anymore. $\omega_c\tau$ is, however, still a good quantity to distinguish between high and low fields. Typically, one would expect that a significant MR only sets in when $\omega_c\tau > 1$, i.e. when an electron completes a full orbit before it is scattered. [50]

Depending on the measured material, the effect of a magnetic field can be quite different. For example, in alkaline metals where only electrons contribute to conductivity and which have a spherical FS, there is almost no MR, close to the prediction that an ideal free electron gas should have none at all.

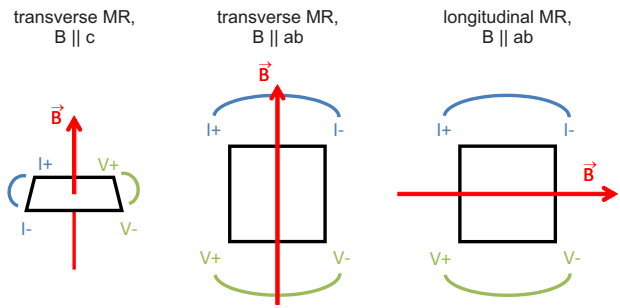

Figure 3.7: Three geometries for the measurement of magnetoresistance in van-der-Pauw-geometry.

In ordinary metals, the MR is positive and grows quadratically with field before it saturates at high fields.

In compensated metals, which have an equal number of electrons and holes, strong MR is observed.

Due to the alignment of spins by the magnetic field the scattering in a ferromagnet is reduced and a negative MR is measured, especially when the temperature is close to the Curie point.

In very clean samples, the quantization of orbits due to the magnetic field leads to the observation of *quantum oscillations*. The frequency of these oscillations is proportional to $1/B$ and they can be used to measure the FS.

3.2.3 Localization phenomena

Impurities in a sample can lead to a localization of charge carriers and therefore to an increase in resistivity. Two such localization phenomena will be discussed in the following, namely Anderson localization and weak localization. Moreover, one should mention the Kondo effect in this context although it is not considered here. [32]

Anderson localization and the Mott-Ioffe-Regel limit

When the resistivity of a metal rises due to temperature or due to a high number of impurities, the mean free path of the charge carriers decreases simultaneously. It was argued that the mean free path cannot decrease beyond a certain point, namely beyond the interatomic spacing. Consequently, a certain maximum resistivity (or minimum conductivity) exists, the so-called Mott-Ioffe-Regel limit. For rare-earth nickelates, for instance, this limit was estimated to be at about $2000\,\Omega^{-1}\mathrm{cm}^{-1}$. [51] Above the limit, it was predicted that a localization of the carriers sets in, so called *Anderson localization* or *strong localization*. [52]

Weak localization and antilocalization

In a system with impurities, the elastic scattering of an electron with impurities can lead to a trajectory that ends at its origin. [53] If simultaneously another electron

travels in the exact opposite direction, their waves will interfere, in the absence of spin-orbit coupling (SOC), constructively at the origin since the phase of the electrons does not change along that path. This leads to an increased probability to find an electron at the origin which implies carrier localization and hence an increase of resistivity. This phenomenon was coined *weak localization* (WL).

If, however, SOC is present in the sample, the phase of the electron changes while traveling in a loop upon arriving back at the origin. And the phase of the electron traveling in the opposite direction changes as well but in the opposite way which leads to a destructive interference at the origin. Hence a decreased probability to find the electron at the origin which leads to a decrease in resistivity. This phenomenon was coined *weak antilocalization* (WAL).

In both cases, the correction to conductivity has a logarithmic temperature dependence.

In a magnetic field, the electrons pick up (an additional) phase shift along their trajectory and hence the effect of weak (anti)localization is reduced which gives rise to a negative MR in the case of WL and a positive MR in the case of WAL.

The effect occurs both in two-dimensional and three-dimensional systems. In 2D-systems, weak (anti)localization is more likely to play a significant role since the electrons are confined and the chance that two trajectories are indeed the same is increased. In this case, there is an anisotropy between MR measured with the field in-plane and out-of-plane.

Chapter 4

LNO-L*X*O superlattices, *X* = Al, Sc: MBE growth and physical properties

4.1 Optimization of growth parameters

In this section, a path is shown how to optimize the growth of $LaNiO_3$ (LNO). Reflection high-energy electron diffraction (RHEED) is an important tool to follow the growth in-situ but is not conclusive and can be misleading sometimes (see Chapter 2.1.2 and Ref. [26]). Ex-situ methods such as x-ray diffraction (XRD), atomic force microscopy (AFM) and electric transport measurements combined provide a good basis to judge the quality of a sample.

General criteria to identify good samples:

- Atomic force microscopy (AFM):
  - smooth surface without precipates and a mean roughness of the order of one unit cell (u.c.).
- X-ray diffraction (XRD):
  - small u.c. volume because defects often lead to an increase. In particular, oxygen vacancies lead to an expansion of the u.c., e.g., in LNO films grown on STO. [54]

  - Laue fringes: the smoother the interfaces and the surface, the more oscillations can be observed.

- X-ray reflectivity (XRR):
  - similar to the case of Laue fringes, the smoother the interfaces and the surface, the more Kiessig fringes can be observed. In an ideal case the average intensity should decrease with q_z^{-4}.
  - the thickness obtained from the analysis of the Kiessig fringes should be close to the targeted value. An error of ~10 Å is normal.

- Electrical transport:
  - metallic samples should have a small resisitivity with a high residual resistance ratio (RRR) because scattering from defects adds to the resistivity, especially at low temperatures where all other scattering channels become less and less important.

In MBE growth, the main tuning parameters for obtaining the desired phase are temperature, pressure and stoichiometry. Since the growth is a rather slow process (in comparison with PLD), thermodynamics will be more relevant than kinetics in determining the resulting phases. This implies that pressure and temperature are crucial to determine which phase will be formed during the growth process. At high temperatures and low pressures Ni^{2+} will be stable whereas Ni^{3+} will form at low temperatures and high pressures.

Note that Ni^{3+} is, in general, the less stable oxidation state under normal conditions. Hence, we chose the maximum pressure that can be obtained in our MBE system. We then adjusted the temperature optimizing the samples with respect to the criteria given above. In the end, we found that La_2NiO_4 grows optimally at ~600°C and ~10^{-6} mbar and $LaNiO_3$ at ~550°C and ~10^{-5} mbar. It is not possible to determine the full pressure-temperature phase diagram but a sketch is shown in Figure 4.1a.

The control of stoichiometry is less direct. In principle, there are two tools, namely rate determination with the QCM and atomic layer control through the observation of RHEED oscillations. Before growth, the fluxes of the effusion cells are calibrated with a QCM (see Chapter 2.2). The rate for lanthanum determined thereby should be the

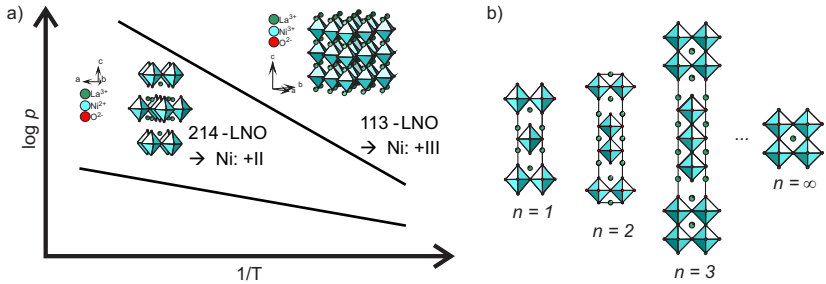

Figure 4.1: a) Sketch of the pressure-temperature phase diagram. b) Ruddlesden-Popper phases, $La_{n+1}Ni_nO_{3n+1}$, form if stoichiometry is off.

most accurate because of its high atomic weight. Therefore, the shutter opening time for lanthanum is kept at the theoretical value found by the aforementioned calibration. We start with a shutter opening time for the *B* site cation according to the theoretical value but vary it in such a way that the RHEED intensity and the amplitude of the oscillations is maximal.

The interpretation of the RHEED pattern alone can be misleading, however. For example, Sullivan *et al.* [26] studied the oscillations of RHEED and x-ray reflectivity (XRR) intensity simultaneously and observed that, indeed, the maximum in XRR corresponds to the completion of a layer but the phase of the RHEED oscillations can be almost opposite, e.g., shifted by 137°.

For this work, in-situ XRR was not available. Getting reliable feedback during growth from RHEED alone is a multiple-step process. First, one should not only rely on the position of the maximum but also aim to maximize the amplitude of oscillations. Once it seems that the optimal stoichiometry is found one should test this hypothesis by varying the shutter opening times again. For one sample of $LaNiO_3$, this approach was followed up to the extremes. The corresponding RHEED oscillations are shown in Figure 4.2.

First, the nickel rate was reduced by ~20%. Astonishingly, we still observed stable oscillations, only the overall intensity was reduced. This behavior is specific for the nickelate system. Instead of precipitates, Ruddlesden-Popper (RP) phases (Figure 4.1b) are formed. These phases still grow in a layer-by-layer fashion, i.e., very

smoothly. Hence the oscillations persist and neither in the RHEED image nor in AFM images taken after the growth defects can be observed.

If, however, excess nickel is deposited, defects do form. These are presumably nickel oxide precipitates which can be seen as additional spots in the RHEED image as in Figure 4.3a. To a certain extent, the formation of precipitates is reversible. If the nickel flux is cut by the right amount, the freshly deposited lanthanum will dissolve the precipitates. If a high nickel rate is maintained over the whole growth, the precipitates remain and can be seen in AFM images afterwards as, for example, in Figure 4.3b.

In an optimal growth, the oscillations will remain throughout the whole growth and the features seen in the RHEED images, e.g., the spot of the directly reflected beam and the inplane reflections, will remain sharp. An example of a 3x(4//4) superlattice (SL) consisting of LNO and LAO is given in Figure 4.4.

To confirm that the overall desired amount of material has been deposited, the film thickness is measured by x-ray reflectivity (XRR). Typically, the thickness of the samples determined through the analyses of Kiessig fringes lies within the error of the measurement which is about 10 Å.

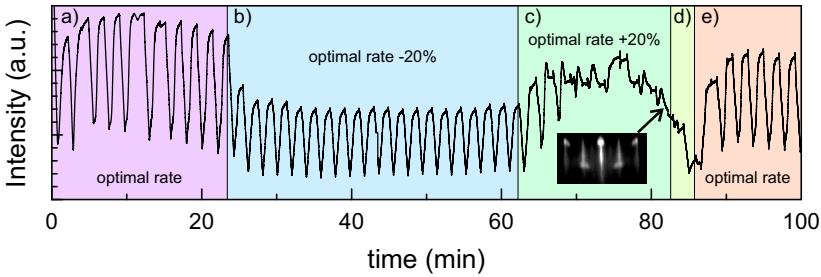

Figure 4.2: Intensity oscillations of the reflected beam during the growth of $LaNiO_3$ on LSAT while changing the Ni rate. a) Stable oscillations with high intensity and amplitude during deposition with optimal Ni rate (r_{opt}, 10 layers). b) Reduction of the Ni rate by ~20% with respect to r_{opt} leads to a reduced intensity and amplitude but the oscillations remain regular (20 layers). c) Increase of Ni rate by ~20% with respect to r_{opt} leads first to a partial recovery of intensity, then to an irregular pattern and finally to a drop in intensity and formation of NiO precipitates (8 layers) that are shown in the inset. A larger version can be found in Figure 4.3a. d) Depositing three consecutive layers of La dissolves the precipitates. e) Continuation with r_{opt} results in a recovery of RHEED oscillations.

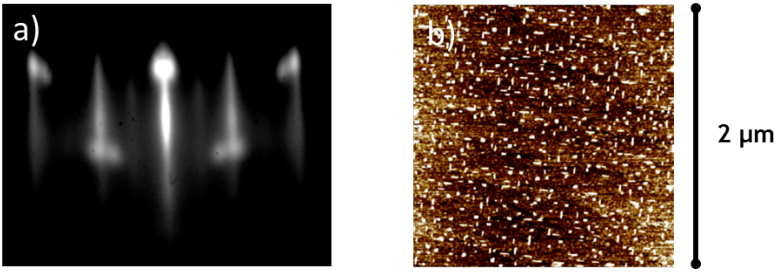

Figure 4.3: NiO defects form when excess Ni is deposited. a) RHEED image of a sample with excess nickel. b) AFM image of a sample with a high nickel rate maintained over the full growth and consequently outgrowth of NiO precipitates.

To conclude, for the growth of $LaNiO_3$ the pressure is set as high as possible. Then, the temperature is varied in order to find the optimal temperature. Once ideal settings are found for pressure and temperature, it is rather simple to keep these conditions (unless major changes or maintenance of the hardware are undertaken). The accurate control of stoichiometry, however, requires a lot of care and experience and is ensured by an iterative approach of in-situ RHEED and ex-situ feedback measurements.

4.2 Characteristics of typical samples

The ex-situ feedback measurements typically include atomic force microscopy (AFM), x-ray diffraction (XRD), x-ray reflectivity (XRR) and electrical transport measurements. To complement those, transmission electron microscopy (TEM) images and x-ray absorption spectra (XAS) were taken for selected samples.

In the present chapter, we show these selected measurements and images. These examples shall illustrate the connection between growth conditions and sample properties. They depict, for example, typical defects in comparison with defect-free areas of a sample, aiming to explain the cause of these imperfections.

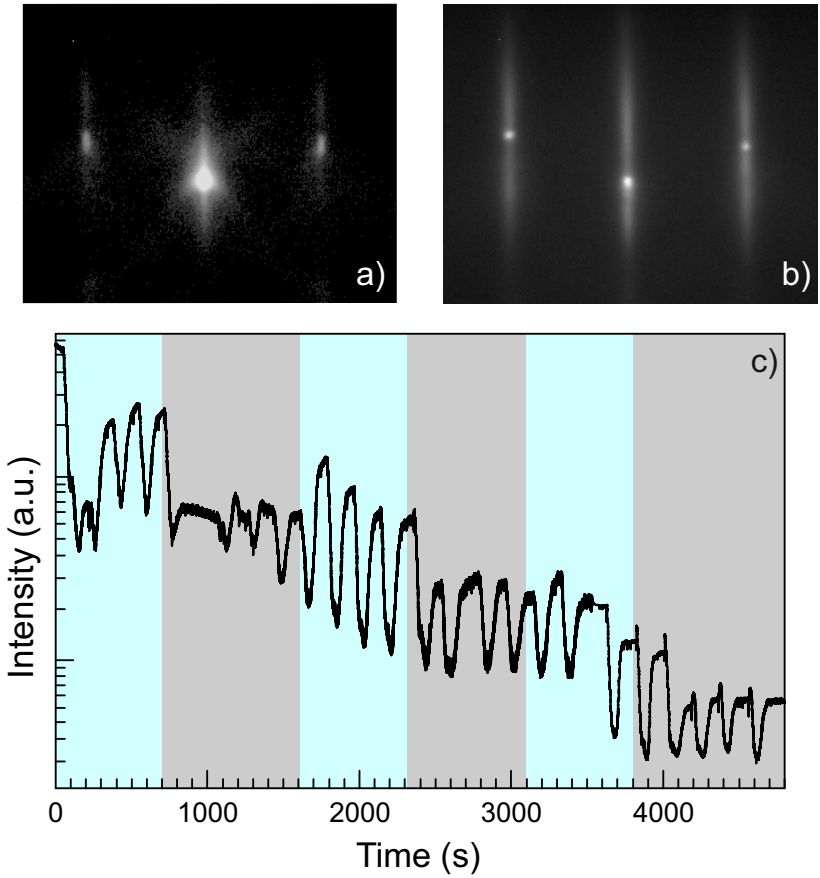

Figure 4.4: Growth of a 3x(4//4) LNO-LAO superlattice. a) RHEED image of the as-received LSAT substrate at growth temperature. b) RHEED image at the end of the growth. c) RHEED intensity oscillations of the directly reflected beam during the growth. Blue-shaded areas mark the deposition of $LaNiO_3$ and grey-shaded areas mark the deposition of $LaAlO_3$.

AFM

Atomic force microscopy measures the surface topology. In a perfect sample, one should not be able to distinguish between substrate and substrate with film on top (see

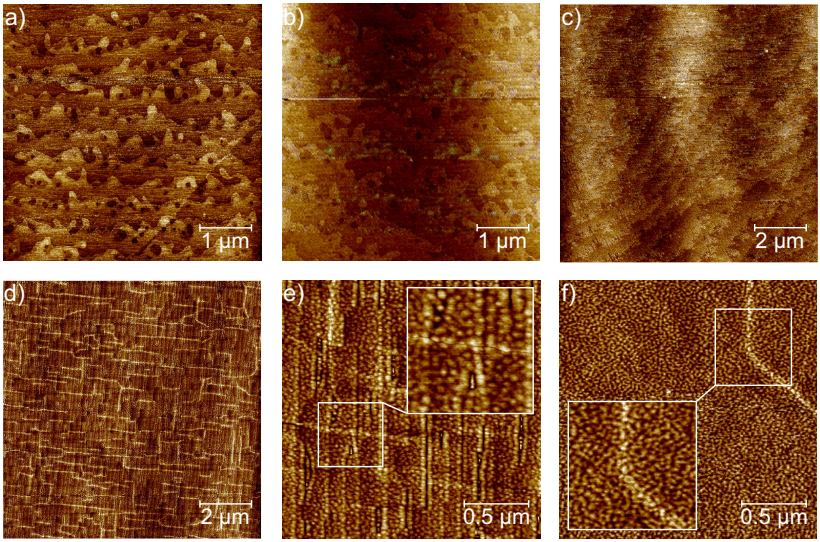

Figure 4.5: AFM images of samples and substrates. a) Annealed GSO substrate. b) The same substrate as in (a) with a 24 u.c. thick SL on top. c) 24 u.c. thick SL grown on LSAT. d) LNO-LAO SL grown on STO shows cracks across the whole sample surface. e) A scan of the same sample as in (d), with higher resolution. The inset shows a magnification of a crack. f) LNO-LAO SL grown on LSAT shows similar cracks as the sample shown in (d) and (e).

Figure 4.5a-c) and the surface should be atomically flat. The roughness is usually of the order of ~½ u.c.

Chemical etching and annealing STO and GSO substrates (see Chapter 2.1.4) leads to a clear visibility of steps and terraces. The same holds for films grown thereon (see Figure 4.5a and b). Atomic terraces are also visible on LSAT and films grown thereon. They are smeared out, however, (Figure 4.5c) because the substrates were used as-received and were neither annealed nor etched. Methods of surface treatment were reported in literature [55, 56] but are not well established and could not be reproduced in this work. Not much effort was used to improve this situation since the quality of the samples was already excellent.

As mentioned above, a substrate with a film on top should essentially look the same as without. The thicker the film is, however, the more smeared out the steps and

terraces are and the more islands form.

Although it is a rather crude method, imperfections during the growth are often visible in AFM images. One example was already mentioned in the previous section (see Chapter 4.1). In the case of excess Ni the resulting NiO precipitates are seen in the AFM images (see Figure 4.3).

In other samples, cracks formed (Figure 4.5d-f). They are much more likely to occur in samples grown on STO than on LSAT. Both substrates impose a tensile strain on LNO and LAO but LSAT does so only slightly. Moreover, the only LSAT sample that exhibits this microstructure is one where problems with the Ni cell, i.e., a closing of the cell due to nickel oxide build-up and consequently a reduced nickel flux, occurred. Hence, we conclude that the cracks result from a combination of strain and nickel deficiency.

XRD

Important structural information is obtained from x-ray scans that are usually taken along the $(0\ 0\ l)_{pc}$ and $(1\ 0\ l)_{pc}$ direction.

The following information can be extracted (see Figure 4.6 for clarity):

- average c-axis parameter of the SL: via Bragg's law (Eqn. 3.1) from the SL Bragg peak position
- in-plane lattice parameter:

$$a_{sample} = a_{substrate} \cdot \frac{k_{sample}}{k_{substrate}}$$

  where $a_{sample} = b_{sample}$ = in-plane lattice parameter of the sample, $a_{substrate}$ = in-plane lattice parameter of the substrate, k_{sample} = in-plane peak position of the sample in reciprocal lattice units (rlu) of the substrate, $k_{substrate}$ = in-plane peak position of the substrate in reciprocal lattice units (rlu) of the substrate
- bilayer thickness: the distance between main peak and SL satellite peak is the inverse of the bilayer thickness

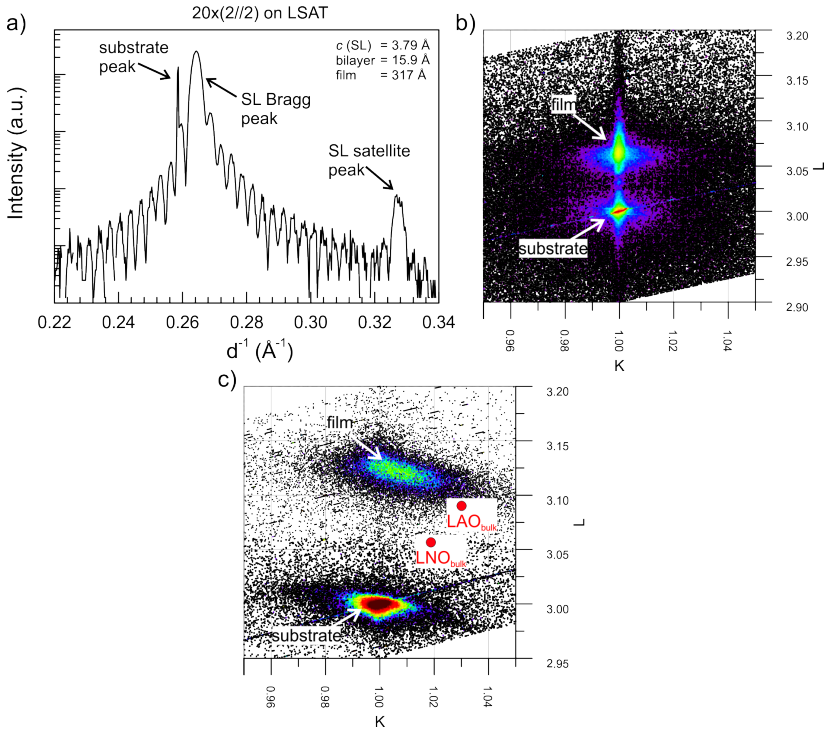

Figure 4.6: a) XRD scan around the $(001)_{pc}$ reflection of a 20x(2//2) LNO-LAO-SL grown on LSAT. b) RSM around the $(103)_{pc}$ reflection of the same sample shows that the film is fully strained. c) RSM around the $(103)_{pc}$ reflection of a 16x(2//2) LNO-LAO-SL grown on STO. The film is partially relaxed. The red dots correspond to the bulk lattice parameters of LNO and LAO, respectively.

- film thickness: the distance between the maxima of the Laue fringes is the inverse of the total film thickness

XRR

X-ray reflectivity is particularly sensitive to the sample surface and interface. Hence, surface & interface roughnesses and film thicknesses are best estimated from reflectivity measurements.

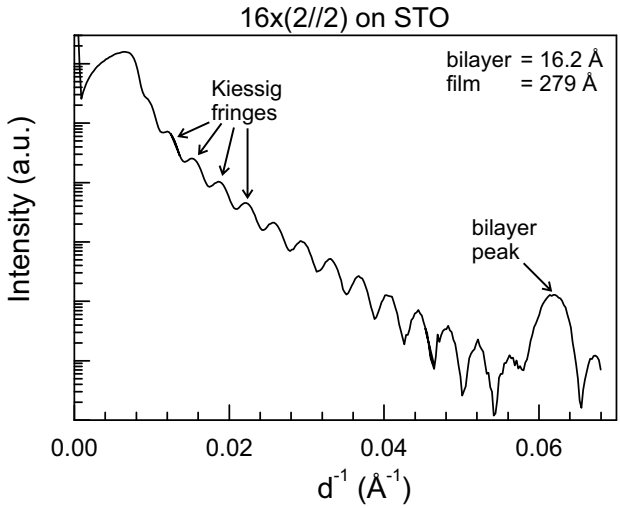

Figure 4.7: XRR of a 16x(2//2) LNO-LAO-SL grown on STO.

The total film thickness is the inverse of the distance between the minima (or maxima) of the Kiessig fringes (see Figure 4.7). And the inverse of the first bilayer peak gives the bilayer thickness. The full reflectivity curve can be fitted with, e.g., the software package ReMagX, [57] www.remagx.org. In case of non-resonant measurements, this procedure gives a reliable value for the total thickness and the surface roughness. In order to access the thicknesses of the individual layers and their corresponding interface roughnesses (including the roughness of the substrate-film interface), resonant measurements are necessary.

Temperature dependent electrical transport

Changes in the electronic structure are usually reflected in the electrical resistance and its temperature dependence which makes a measurement thereof a very sensitive probe. On the hindsight, it is difficult to disentangle the different contributions (see Chapter 4.5). But in general, one can say that any kind of defect, e.g., vacancies, interstitials, grain boundaries and interface roughness, add to the resistivity of an

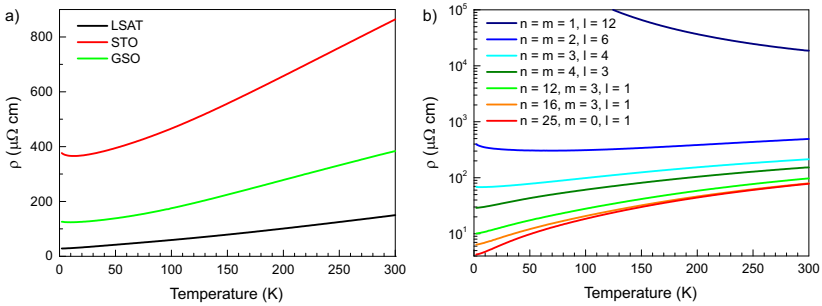

Figure 4.8: a) Resistivity of 3x(4//4) SLs grown on LSAT (black), STO (red) and GSO (green). b) Resistivity of thin films and superlattices with different LNO thicknesses, $[(LaNiO_3)_n(LaAlO_3)_m]_l$, grown on LSAT.

otherwise metallic LNO sample. Hence, when aiming for higher sample quality one should look for lower resistivity.

Apart from defects there are also intrinsic effects that lead to an increased resistivity, i.e., reduction of LNO layer thickness and an increase of tensile epitaxial strain which will be discussed in the following. A special role that shall also be considered in further detail is the role of oxygen vacancies.

Influence of epitaxial strain

It was reported that an increase of tensile strain leads to a reduced bandwidth of the *d*-band, [5] and hence, the resistivity also increases. This effect was observed by Son *et al.* [5, 58].

Our samples grown on LSAT and GSO follow this general trend (see Figure 4.8a). In contrast, samples grown on STO have a significantly higher resistivity, even higher than comparable PLD-grown samples (see Chapter 4.3). Among all the other commonly used substrates, STO with its non-polar surface is a special case. Growing a polar material on-top of a non-polar material leads to an ever growing electrical potential. This scenario was named *"polar catastrophe"* (see Chapter 2.1.4).

It was reported that the polarity drives the formation of NiO precipitates at the interface between LNO grown on-top of STO. [59] TEM images of our MBE-grown samples don't show any precipitates (Figure 4.17c). Hence, another mechanism that alleviates the polarity must occur. A reasonable explanation is the formation of oxygen

vacancies at the interface which would increase the sample's resistivity. The role of oxygen vacancies on the transport properties will be discussed below in more detail.

Influence of LNO layer thickness

Different groups found an increase of resistivity accompanying a decrease of the number of consecutive LNO layers and even an insulating state once the thickness was reduced beyond a certain critical thickness. [5, 6, 8, 58, 60] However, there is a dispute on both the critical thickness and the origin of the effect.

Two groups (Scherwitzl *et al.* [6, 60] and Son *et al.* [5, 58]) claim that the Mott-Ioffe-Regel limit (see Chapter 3.2.3, [52]) is reached in 3 to 4 nm thick films and strong localization occurs.

King *et al.*, however draw a different picture. [8] Based on their transport and ARPES data, they exclude the above mentioned localization scenario. Moreover, they exclude a Mott transition in the Brinkman-Rice scenario and a bandwidth narrowing by quantum size effect. Instead, they observe a sudden breakdown of Fermi liquid-like quasiparticles once the LNO thickness is reduced to 2 u.c. and attribute this behavior to charge/spin order.

The values of resistivity reported in literature vary significantly between the different groups (see Table 4.1). Astonishingly, we observe very similar but somewhat lower values for resistivity in our superlattices (Figure 4.8b) grown on LSAT as for the thin films reported in Ref. [8]. Note that the latter were grown on LAO substrates which exert a small compressive strain and should therefore have a lower resistivity. [5] However, the strain effect for both cases (LAO and LSAT) is rather small and is apparently overruled by the effect of sample quality.

To conclude, we can say that we were able to reproduce the thickness dependence reported in literature and improve sample quality along the way.

Influence of oxygen vacancies

As mentioned above, any kind of defect leads to an increase of resistivity. Among the different kinds, oxygen vacancies play a special role. They form easily because oxygen ions are quite mobile in ceramic materials already at rather low temperatures. Even at room temperature, samples tend to lose (excess) oxygen over time. Consequently, the surrounding pressure and temperature during growth, while cooling and afterwards are crucial for the final amount of oxygen in a sample. Moreover, oxygen

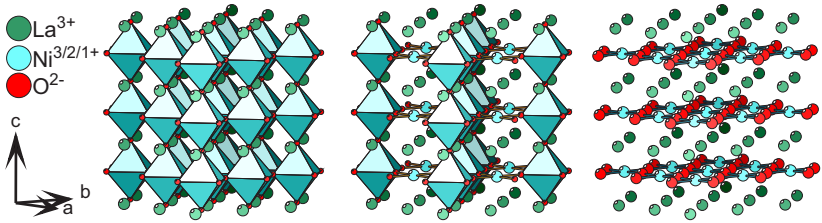

Figure 4.9: Structural changes accompanying the reduction of $LaNiO_3$ (left) to $LaNiO_{2.5}$ (middle) $LaNiO_2$ (right).

vacancies not only distort the structure but also act as a dopant, effect the amount of charge carriers and hence properties that depend thereon, for example resistivity.

LNO is a material that is prone to the formation of vacancies. It is possible to tune their amount in a controlled manner via a chemical reaction either with hydrogen gas or calcium hydride and the process can be reversed by annealing in ozone. [61–63] Figure 4.9 shows how, in this fashion, $LaNiO_3$ (Ni: +III) is converted into $LaNiO_{2.5}$ (Ni: +II) and finally into $LaNiO_2$ (Ni: +I). Along the way, resistivity shows metallic (Ni: +III), insulating (Ni: +II) and again metallic (Ni: +I) behavior.

With these drastic changes in mind, it is not surprising that the resistivity of bulk LNO was found to increase almost exponentially with the amount of oxygen vacancies since by creating an oxygen vacancy, Ni(II) is formed. [9]

In bulk samples, thermogravimetric analysis (TGA) or iodometric titration can be used to determine oxygen stoichiometry. Unfortunately, no corresponding measurement technique exists for thin films since their masses are orders of magnitude smaller than the substrates' masses. However, especially thin films are prone to the formation of oxygen vacancies or interstitials. Some of the physical properties of LNO thin films, especially measurements of resistivity, that were reported in literature might be dominated by oxygen vacancies.

For example, the thin films grown and measured by Scherwitzl *et al.* [6, 60] and Son *et al.* [5, 58] might only reach the Ioffe-Regel limit because of oxygen vacancies. [52] Scherwitzl *et al.* [6] discuss Ni^{2+} ions originating from oxygen vacancies as an origin for their observation of an isotropic, negative magnetoresistance in a 7 u.c. thick film grown on STO.

In summary, differences in oxygen vacancy concentration could be the main reason why thin film resistivities reported from different groups vary as much. Moreover, they might drive strong localization which then leads to reaching the Ioffe-Regel limit and explain why the critical thickness below which a metal-to-insulator transition is observed changes as well.

If one compares only the samples with lowest resistivity, i.e., highest sample quality, which also includes the samples discussed in this work, the values of resistivity and also the critical thickness agree quite well. [7, 8] Hence, we can assume that these are well oxygenated samples that show the intrinsic properties of LNO.

Transmission electron microscopy (TEM)

In order to judge overall sample quality it is important to combine local and non-local probes. X-ray techniques and transport measurements typically probe a large sample volume. The local probe, par excellence, is TEM. This technique maps the electron density and has advanced immensely in recent years such that it is possible to achieve atomic resolution nowadays. It should be kept in mind that one always sees a projection of atoms in a thin specimen slab (~10th of nanometers) on top of each other which can make it difficult to find an unambiguous interpretation. Moreover, "local probe" always means that it is impossible to give good statistics over the whole sample.

All images that will be shown in the course of this chapter were taken in collaboration with the StEM group headed by Prof. P. van Aken. The observations and analyses were performed by Dr. A. F. Mark and the TEM specimen were prepared by U. Salzberger.

Cross-sectional TEM foils from each specimen were prepared using a standard wedge polishing procedure. A slice was cut from the prepared thin film using a diamond wire saw; the slice was then mechanically ground, followed by tripod polishing. Final thinning was done with argon ion beam milling in a stage cooled with liquid nitrogen (Gatan Precision Ion Polishing System).

Figure 4.10a shows a TEM image of a (4//4) superlattice consisting of LNO and $LaScO_3$ (LSO) grown on GSO which exerts a high lattice mismatch of ~3% (see Equation 2.1) on LNO but a small compressive strain (~2%) on LSO. At the bottom

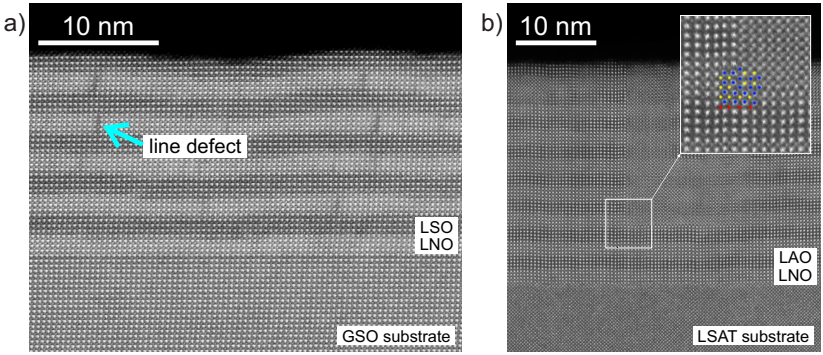

Figure 4.10: a) Annular dark field (ADF) image of a 5x(4//4) superlattice consisting of LNO (bright layers) and $LaScO_3$ (dark layers) grown on a scandium terminated GSO substrate. The green arrow indicates the occurence of a line defect which is quite common in this particular superlattice. b) ADF image of an 8x(4//4) superlattice consisting of LNO (bright layers) and LAO (dark layers) grown on an LSAT substrate. The inset shows a close-up at the corner of a 3D-Ruddlesden-Popper fault. The colored dots, blue, yellow and red represent lanthanum, nickel and aluminium, respectively.

of the image, one can see the GSO substrate followed by alternating layers of nickelate (bright) and scandate (dark). The interface between substrate and superlattice is remarkably sharp which can be attributed to (i) the surface treatment before growth and (ii) to the low deposition energies obtainable in MBE growth.

The following interfaces appear “wavy”. Due to the high tensile strain on LNO, it might be energetically favored to form already the second layer before the first one is complete (compared to substrates exerting smaller strain, see Fig 4.10b). During deposition of LSO the space in the incomplete layer is filled. And on average, the strain on LNO is released in this way. Moreover, dark line defects perpendicular to the interfaces are observed in the LNO layers of this specific sample. It is likely that within these defects nickel is replaced by scandium, which appears darker in the image. This is another route of strain relaxation.

Another common defect in LNO based samples are 3D-Ruddlesden-Popper faults. They originate from nickel deficiency or lanthanum surplus during growth. At a certain point, when a critical amount of lanthanum oxide at the surface is reached, an island consisting of a monolayer of lanthanum oxide is formed. All consecutive lay-

ers are shifted by half a unit cell which is sketched in the inset of Figure 4.10b. A more detailed discussion can be found below (Chapter 4.3).

Overall, TEM enables the detection of local defects that often play an important role in determining the macroscopic physical properties. For example, no indication of the line defects seen in the sample grown on GSO is visible in x-ray diffraction. XRD shows, in this case, only a fully strained superlattice whereas it might be locally relaxed.

Given that TEM maps the electron density, it is clear that it is particularly sensitive to heavy atoms. Oxygen atoms are not visible in annular dark field (ADF) TEM images. However, nowadays it is possible to make even oxygen atoms visible in a separate measurement. For this specific set of samples, the overall structural quality was the main point of interest and not the mapping of oxygen atoms. For a different set of samples, which will be discussed in Chapter 5, the position of oxygen atoms is of importance and hence their positions were mapped and the images are presented in Chapter 5.2.

Despite the locality of the probe, point defects are still quite impossible to see because an image is always a projection of several atoms behind each other. Moreover, the processing of the sample, i.e., thinning it down to several tenths of nanometers, and the measurement itself with a highly energetic electron beam in vacuum can damage the sample. These drawbacks should be carefully ruled out.

To conclude, the images that were discussed above show a high sample quality with the low deposition energy of MBE enabling a particularly sharp interface between substrate and film. The observed defects are innate to the deposited materials and to the growth technique. The influence of the latter will be discussed in the following (Chapter 4.3).

X-ray absorption spectroscopy (XAS)

A probe for the electronic structure of a metal with empty $3d$-states is XAS at the respective L-edges at which electrons are excited from $2p$- into $3d$-states forming excitonic bound states giving rise to the *"white lines"* in the spectrum or they are excited into the continuum which gives rise to an *"edge jump"*.

Because of strong spin-orbit coupling of the core $2p$ core level, the edge is split into

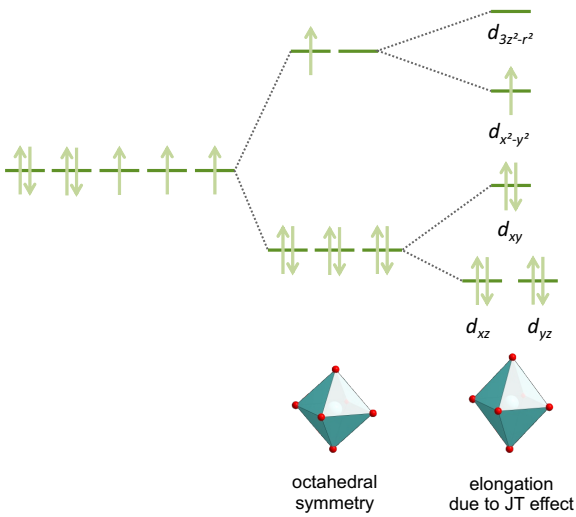

Figure 4.11: Crystal field splitting of the d levels in the case of a low-spin d^7-system. Left: in a spherical ligand field, all orbitals are degenerate; middle: in an octahedral ligand field the levels are split into three degenerate t_{2g} levels and two degenerate e_g levels; right: the elongation of the octahedral environment leads to a further lifting of the degeneracy.

two, namely peaks corresponding to the L_3- (J = 3/2 at lower energies) and the L_2-edge (J = 1/2 at higher energies). For a more detailed explanation, see Chapter 3.1.2.

For the series of 3d-metals, the transitions occur at energies of about 400 – 1000 eV and therefore in the soft x-ray regime. Since the spectra give information about the site and symmetry projected empty density of states they allow for conclusions on the chemical environment, including oxidation state and local crystal field symmetry. In this chapter, we investigate the nickel $L_{2,3}$-edges of our superlattices, which occur at energies of ~855 eV and ~872 eV. The L_3-edge at ~855 eV overlaps with the strong lanthanum M_4-line. To facilitate the access to the spectra for the reader, we subtracted a Lorentzian fitted to the lanthanum line in all spectra shown in this work. For details on the procedure, see Chapter 3.1.2 and Ref. [45].

In the present discussion, we assume an oxidation state of +III for nickel. The influence of the oxidation state on the nickel L-edge spectra will be discussed later in Chapter 5.3.1. First, we will discuss the influence of the symmetry and bonding

on the spectra. Because of multiplet effects (interaction of empty states in the d-shell with the core hole), the L-edge lineshapes are complicated and can only be described well through theoretical calculations in cases where it is sufficient to consider a very localized picture, e.g., the insulator NiO. [38] Therefore, we restrict ourselves to a qualitative and phenomenological discussion.

In the perovskite structure, nickel is surrounded by six oxygen ions. The octahedral symmetry leads to a splitting of the d levels of $10\,\mathrm{Dq} \approx 2\,\mathrm{eV}$ into three degenerate t_{2g} and two degenerate e_g levels (see Figure 4.11). [16] In trivalent nickel, which is nominally d^7, the t_{2g} states are fully occupied and can therefore be neglected for the discussion of XAS. In principle, an ion with one electron in the e_g states should be prone to the Jahn-Teller (JT) effect, which causes a tetragonal distortion of the octahedron. As we can see in Figure 4.11, the degeneracy is lifted and overall the energy of the d^7-system is lowered. d^1, d^4, d^7 or d^9 low-spin electronic configurations in an octahedral field are prone to a JT instability. And the effect is usually strong for d^7 and d^8 configuration.

So far, there are no indications of non-degenerate e_g-orbitals in LNO, probably

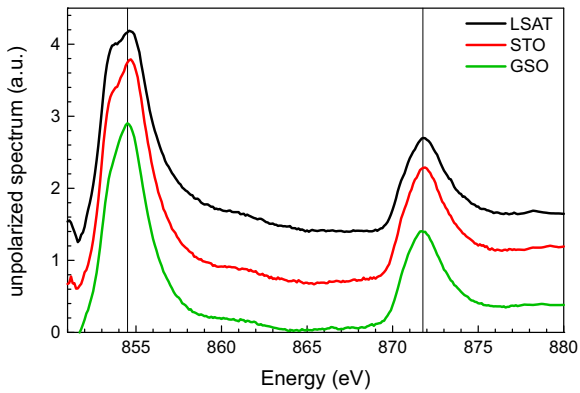

Figure 4.12: Polarization averaged XAS spectra obtained in fluorescence yield mode at the Ni $L_{2,3}$-edges after subtraction of a Lorentzian fitted to the lanthanum M_4 line. The energy scale of all spectra was normalized to the lanthanum M_4 line. All samples have the same layer sequence, i.e., 8x(4//4): $[(LaNiO_3)_4(LaAlO_3)_4]_8$ on LSAT (black), $[(LaNiO_3)_4(LaAlO_3)_4]_8$ on STO (red), $[(LaNiO_3)_4(LaScO_3)_4]_8$ on GSO (green). The black, vertical lines serve as a guide to the eye and indicate the peak positions of the sample grown on GSO at the L_3- and L_2-edge.

related to the large band width that make the JT instability unfavorable. Both, a bandwidth (Guan *et al.* [64] calculate a bandwidth of 5.5 eV for LNO) much larger than the JT splitting (typically 0.1–0.5 eV) or a charge order, which lifts the degeneracy of the e_g-levels, can cause this effect. [65]

Moreover, according to Johnston *et al.* [13] the ground state is better described as $d^8\underline{\mathrm{L}}$, where $\underline{\mathrm{L}}$ denotes a ligand hole, i.e., an electron is transferred from oxygen to nickel. And a d^8-state is no longer prone to the JT effect.

Upon application of tensile or compressive strain, the degeneracy is lifted. [16, 17] Tensile (compressive) strain leads, in a somewhat simplified picture, to a compression (elongation) of the nickel-oxygen octahedra. As a consequence, the in-plane $3d_{x^2-y^2}$ (out-of-plane $3d_{3z^2-r^2}$) orbital is lowered in energy and therefore the degeneracy is lifted and orbital polarization occurs. In addition, confinement induces orbital polarization without the necessity of a splitting of the e_g-orbitals.

This polarization can be made visible by measuring XAS with polarized light. X-rays with the electric field vector lying in the plane will mostly excite electrons into the in-plane $3d_{x^2-y^2}$-orbitals and x-rays with the electric field vector out-of-plane will only excite electrons into the $3d_{3z^2-r^2}$-levels (see Chapter 3.1.2). By looking at the difference spectra, one can determine the ratio of holes in the $3d_{x^2-y^2}$- and $3d_{3z^2-r^2}$-orbitals.

Before we turn to the spectra measured with polarized light, it is worthwhile to look at the polarization averaged spectra. Note that all spectra shown in this section were taken in fluorescence yield (FY) which does not measure the pure XAS cross section. [66] The proper measure of XAS lineshapes when multiplet effects are significant is total electron yield (TEY). Unfortunately, we were not able to take a full dataset of TEY data with sufficient quality. However, the effects and trends discussed below are also visible in the TEY data.

As we can see in Figure 4.12 the lineshape changes upon increasing strain, especially at the L_3-edge. The peak appears to consist of two peaks and while increasing the epitaxial strain from LSAT via STO to GSO, the peaks move closer to each other and the first peak decreases in intensity. By taking the black, vertical line in Figure 4.12, which indicates the peak position of the sample grown on GSO at the L_3-edge, as a reference, we can see the shift of the peak.

There are two main suspects for this evolution of spectra. The first one are oxygen vacancies. As we have seen in Section 4.2, we can exlude a major contribution of oxygen vacancies. Moreover, in compounds with a contribution of divalent nickel the first peak at the L_3-edge is higher than the second which is not observed in the present case. [67] The second argument is that the strain-induced change of symmetry leads to a change of crystal field and hybridization and therefore to the observed change in the lineshape. Indeed, it was shown through cluster calculations that the e_g-splitting increases with growing tensile strain. [17] However, the effect on the XAS lineshapes of such an increased e_g-splitting is unclear. So far, existing theories fail to accurately reproduce the XAS lineshapes of LNO.

The opposite trend regarding the lineshape is observed for the series of rare-earth nickelates, *RE*NiO_3, with decreasing radius of the rare-earth ion. [67–69] The peak-splitting increases and the two peaks become more equal in intensity. As in our case, the origin of this behavior is not well understood but it is closely related to the metal-to-insulator transition observed in all rare-earth nickelates, except $LaNiO_3$.

Figure 4.13 shows the absorption spectra of the same three samples as discussed above, now each with the electric field vector of the linearly polarized light lying either in-plane (E ∥ x) or out-of-plane (E ∥ z). As we can see immediately, the change of lineshape is most noticeable with E ∥ z. This is the polarization that probes the $3d_{3z^2-r^2}$-orbital which is the one connecting a nickel ion via an oxygen ion with either aluminum (samples grown on LSAT and STO) or scandium (sample grown on GSO). While only small changes occur between the sample grown on LSAT and STO, the strongest effect is observed when exchanging $LaAlO_3$ for $LaScO_3$ as the insulating layer and growing the sample on GSO.

With respect to strain, the sample grown on STO with a lattice mismatch of 1.7% is about in the middle between LSAT with 0.7% and GSO with 3.3%. If the observed effect was solely based on strain, the evolution of the spectra should be more continuous. Hence, it seems likely that the contrast between the sample on GSO and the other two samples is related to the exchange of aluminum for scandium.

From the polarized spectra, one can also obtain the orbital polarization and Wu *et al.* [17] found for (4//4)-superlattices that the polarization increases quite linearly with epitaxial strain. For the superlattices investigated in the course of this work, we found

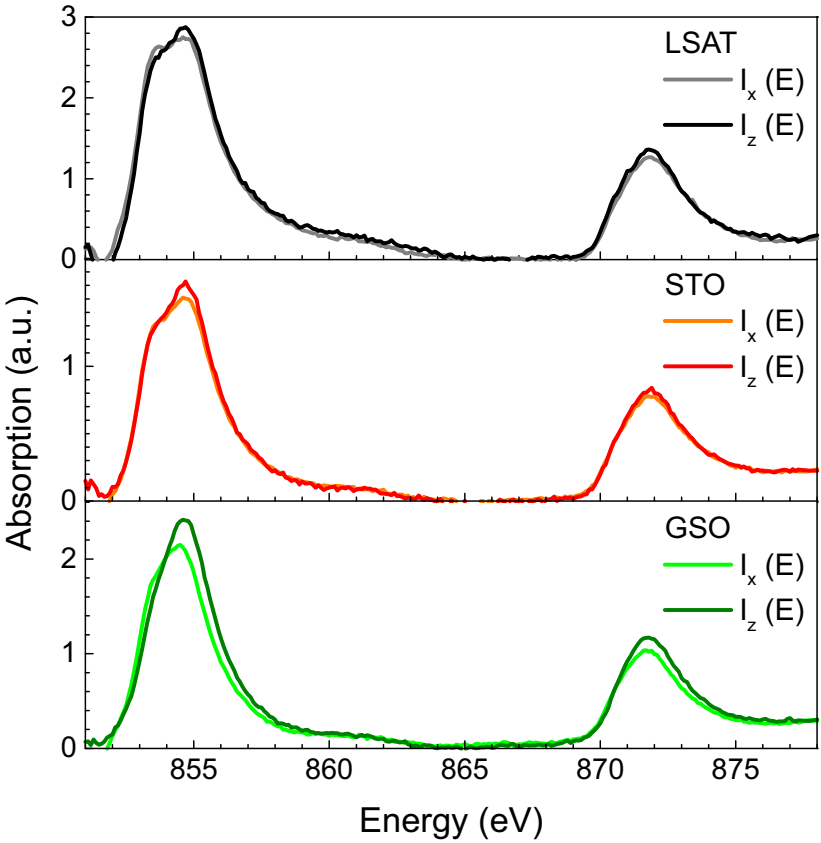

Figure 4.13: XAS spectra obtained in fluorescence yield mode for E ∥ x (in-plane) and E ∥ z (out-of-plane) at the Ni $L_{2,3}$-edges. A Lorentzian was fitted to the lanthanum M_4 line and subtracted. All samples have the same layer sequence, i.e., 8x(4//4): $[(LaNiO_3)_4(LaAlO_3)_4]_8$ on LSAT (black/gray), $[(LaNiO_3)_4(LaAlO_3)_4]_8$ on STO (red/orange), $[(LaNiO_3)_4(LaScO_3)_4]_8$ on GSO (green).

that they roughly follow the reported trend. [16, 17] The data are quite noisy which prevents an accurate determination of the average hole ration. However, if we compare the normalized dichroic signal (Figure 4.14), which is the least affected by measurement issues, and compare those with the spectra reported in literature we see that they

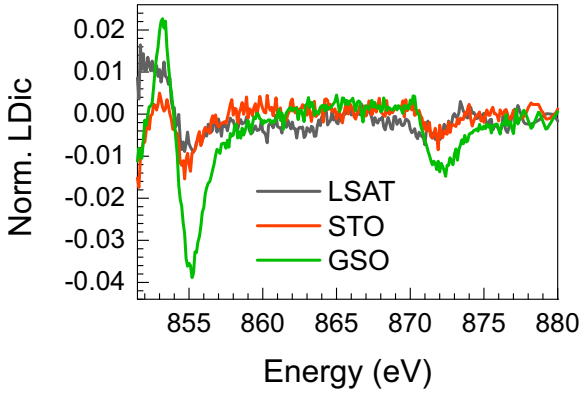

Figure 4.14: Normalized dichroic signal $[I_x(E) - I_z(E)]/[(2 \cdot I_x + I_z)/3]$ at the Ni $L_{2,3}$-edges. All samples have the same layer sequence, i.e., 8x(4//4): $[(LaNiO_3)_4(LaAlO_3)_4]_8$ on LSAT (gray); $[(LaNiO_3)_4(LaAlO_3)_4]_8$ on STO (red); $[(LaNiO_3)_4(LaScO_3)_4]_8$ on GSO (green).

are indeed very similar and that the e_g-splitting increases with the lattice mismatch. Later on (Chapter 4.3), we will directly compare spectra of samples grown with different techniques and reflect on their differences.

In conclusion, we showed how the electronic structure is probed by XAS. We observe changes in the lineshapes of polarization-averaged spectra when increasing epitaxial strain but lack an explanation which will have to be delivered by theoretical calculations. To date, the theoretical models are not able to accurately reproduce the spectra. And within the accuracy of the measurement, the orbital polarization of our samples follows the reported trend. [16, 17]

4.3 Comparison between MBE and PLD grown samples

Nickelate superlattices are a very sensitive model system for investigating the influence of extrinsic parameters and defects on electronic and magnetic properties. Having a unique infrastructure allowing PLD and ozone-assisted MBE growth in the same laboratory, we chose to directly compare nominally identical $LaNiO_3/LaAlO_3$ (LNO/LAO) superlattices grown by these two techniques. The PLD samples were grown in collaboration with the technology group by Georg Christiani. The results

from x-ray diffraction (XRD) and transport agree widely. Small differences in the value of resistivity are attributed to a higher oxygen content and lower disorder in MBE samples and a more accurate lanthanum-to-nickel ratio in PLD samples. Still puzzling is that the lineshapes of the nickel $L_{2,3}$ x-ray absorption spectra differ between MBE- and PLD-grown sample.

We compare superlattices deposited on the (001) surfaces of cubic LSAT, with a small lattice mismatch, and samples grown on STO, with larger mismatch. The bulk (pseudo)cubic lattice constants of STO, LSAT, LNO and LAO are 3.91, 3.87, 3.84 and 3.83 Å respectively. [70] Growth parameters were optimized individually for each growth technique. The optimization of MBE growth is explained in great detail in Chapter 4.1 and PLD samples were deposited in a 0.5 mbar oxygen atmosphere at 730°C from stoichiometric targets using a KrF excimer laser with a 2 Hz pulse rate and a laser fluence of 1.6 J·cm^{-2}. Subsequent annealing at 1.0 bar oxygen pressure and 690°C for 30 min ensured oxygen stoichiometry. Layer thickness control was achieved by iterative sample growth and XRD feedback measurements.

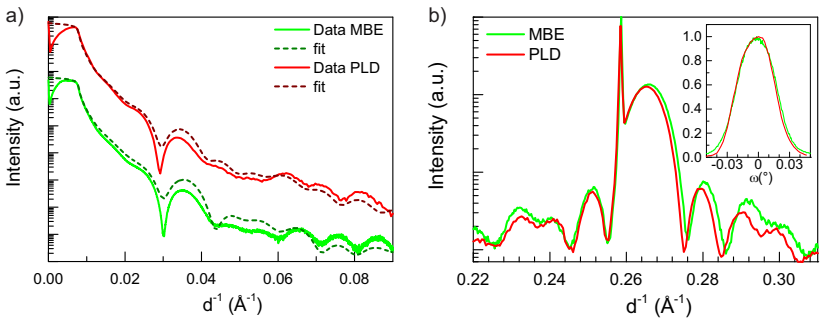

Figure 4.15: Hard x-ray data of two nominally identical 3x(4//4) samples on LSAT substrates grown by MBE (green solid line) and PLD (red solid line). a) Reflectivity range. From a Parrat fit (dashed lines, fitted with the software package ReMagX, [57] www.remagx.org) we obtained total film thicknesses of 99 Å and 105 Å for the MBE and PLD sample, respectively. b) Scans through the (001) reflections of substrate and superlattice. The average c-axis parameter is 3.768 ± 0.008 Å for the MBE sample and 3.773 ± 0.005 Å for the PLD sample. The inset shows the corresponding rocking curves measured at the (001) reflection of the film where the intensities were normalized such that the maximum intensity of each scan is equal to 1.

The nominally identical samples grown by MBE and PLD on LSAT show only minor differences in their XRD patterns, both in scans through the (0 0 1) reflection and in reflectivity measurements (Figure 4.15). The *c*-axis parameters of the superlattices, which are an average of LNO and LAO lattice parameters, are identical within the experimental error. The damping of the reflectivity curve, correlated with the surface roughness, is almost the same. Only the total thicknesses, obtained from Parrat fit, differ. The MBE sample is 99 Å and the PLD sample is 105 Å thick, whereas the target thickness was 90 Å in both cases. The surface roughness for both samples is approximately 4 Å. Due to the low contrast between substrate and film, interface roughnesses and bilayer thicknesses cannot be extracted unambiguously from the fit of the non-resonant data only.

While the global picture from XRD of the two samples is nearly identical, they differ at a local level as is revealed by TEM. TEM examination was done using scanning mode and the annular dark field (ADF) detector in a corrected JEOL ARM200F operated at 200kV. Each thin foil was prepared by first cutting a cross-section through the layers, then thinning the section using mechanical grinding and polishing on both sides to create a wedge-shaped slice (wedge angle 2°). The slice was thinned to electron transparency by ion-milling with LN_2 cooling. The images were taken in collaboration with the StEM group headed by Prof. P. van Aken. The observations and analyses were performed by Dr. A. F. Mark and the TEM specimen were prepared by U. Salzberger.

Figure 4.16 shows annular dark field (ADF) images taken from 8x(4//4) and 20x(2//2) superlattices grown with MBE and PLD on LSAT. Moreover, Figure 4.17 shows the substrate-superlattice interface of an MBE grown sample with an 8x(4//4) sequence. In ADF images, common features observed in all samples, with significantly varying densities, are 3D-Ruddlesden-Popper (3D-RP) faults caused by an additional layer of lanthanum oxide over a small area-fraction of a layer. All subsequent layers are shifted by half a unit cell. These faults were already described in Chapter 4.2 and visualized in the inset of Figure 4.10b. They reflect a deviation from the ideal 1:1-ratio of A- and B-site cations. Despite the apparently large volume of the shifted areas in the image, the change in stoichiometry indicated by one RP fault is very small. Adjustments in the ratio of A to B cations occur only at the edges of the

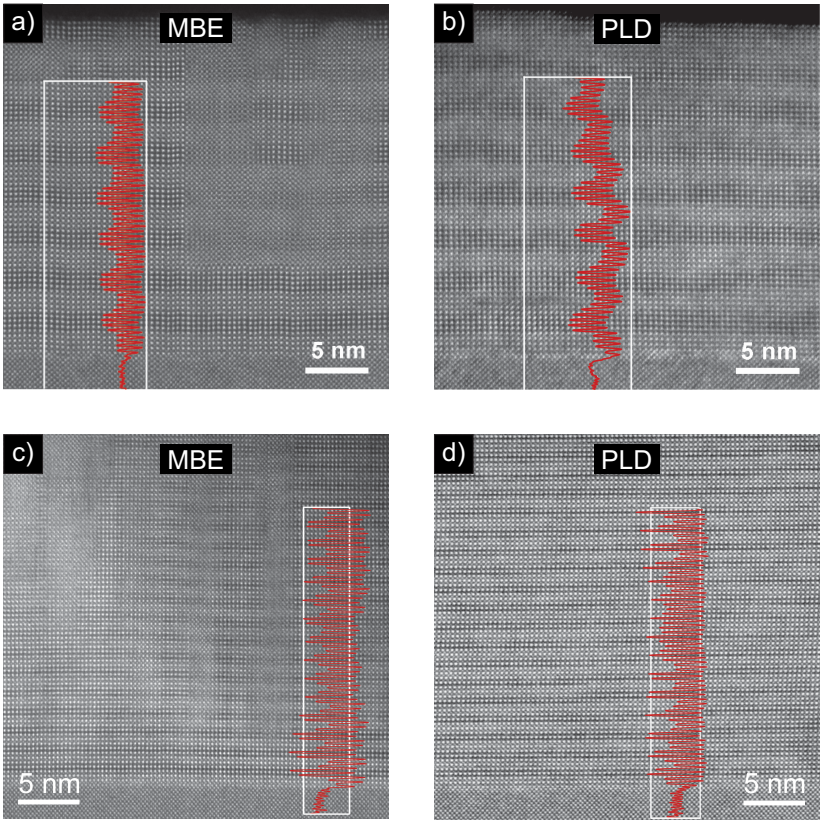

Figure 4.16: Annular dark field (ADF) images of two 8x(4//4) (a&b) and two 20x(2//2) (c&d) superlattices grown by MBE (a&c) and PLD (b&d) on LSAT. The MBE-grown samples show well-defined blocks caused by 3D-Ruddlesden-Popper faults. The PLD-grown samples exhibit a higher interface roughness and less over-all homogeneity than the corresponding MBE samples, but hardly any 3D-Ruddlesden-Popper faults are found. The read lines are integrated intensity profiles from the boxed areas in images a)–d). They visualize the regularity of the superlattices.

shifted region to accommodate the RP fault. In PLD growth the cation stoichiometry is largely predetermined macroscopically by the composition of the target. In MBE growth stoichiometry control takes place on the level of individual atomic layers and is therefore less accurate, hence a higher density of 3D-RP faults results.

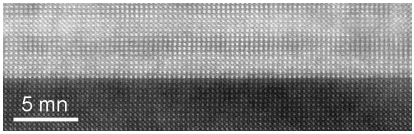

Figure 4.17: The annular dark field (ADF) image of an MBE-grown sample – 8x(4//4) – on STO shows a sharp substrate-superlattice interface. NiO precipitates, which had been observed in a similar sample grown by PLD, [59] were not found. Instead, 3D-RP faults are visible (not shown), similar to the ones shown in Figure 4.16.

At the substrate-film interface, the images show a bright layer indicating the accumulation of heavier atoms in both samples. In the MBE sample, only one atomic layer right at the interface is affected whereas in the PLD sample 2 - 3 layers appear brighter. Two scenarios are possible. First, atoms could migrate from the bulk to the surface if the new surface was more stable than the original. For example, Ngai et al. [55] reported that SrO mounds form upon annealing LSAT substrates at temperatures ≥ 1100°C. However, our samples were grown well below 1100°C and an enrichment of Sr at the interface would lead to a reduced intensity, contrary to our observation. Hence we exclude this scenario.

Second, a scenario where statistically distributed vacancies are filled with lanthanum or nickel appears very likely. LSAT is a solid solution with statistical occupation of Sr and La cations at A sites and Al and Ta on B cation sites of the perovskite ABO_3 structure, hence the termination of the substrate surface is chemically not well defined. During the MBE growth of the first atomic La layer the vacancies are filled resulting in one bright atomic layer. The extended bright region in the PLD-grown sample can be understood if one takes into account that the energy of impinging particles is much higher, thus more atomic layers are affected.

The high energy of the impinging particles is suspected to cause rougher interfaces. Indeed, the MBE sample appears to have flatter interfaces than the PLD sample. We assigned each unit cell of the 8x(4//4) superlattices grown on LSAT (Figure 4.16a&b) to either an LNO or an LAO layer to provide a rough estimate of the average lateral step spacing in the interfaces. It is approximately 12 (33) nm for the PLD (MBE) sample. The images are 2D representations of 3D structures. So a difference in thickness between the two samples could lead to a difference in the number of steps. Thick-

ness measurements of multi-species, wedge polished samples are often not very accurate. [71] Nonetheless, the attempt was made using the t/λ technique [72] which gives an approximate thickness of 40 ± 14 nm for the PLD sample. TEM foils of other MBE-grown layered structures, prepared in the same way as the sample shown in Figure 4.16a, were measured giving thicknesses of 34 ± 10 nm and 77 ± 32 nm. For the difference in the separation of steps between the MBE image and the PLD image in Figure 4.16a&b to arise from thickness differences the MBE sample would have to be on the order of 14 nm thick, which is much thinner than the similar sample measured. Hence, we conclude that the observed difference is indeed inherent to the samples and not to the specimen preparation or imaging quality.

Although the above analysis provides a solid proof that the interfaces of the MBE sample are smoother, it is difficult to discern these differences by only looking at the images themselves because the image of the PLD sample is lower in quality. To make the differences visible by eye and support our findings, images of superlattices with thinner LNO and LAO layers – 20x(2//2) – were taken (Figure 4.16c&d). Here, the image quality is approximately equal and one can see by eye that the interfaces of the MBE sample are sharper but come at the price of having a higher density of 3D-RP faults.

Differences between the two growth techniques become visible also for LNO/LAO grown on STO substrates. It was previously reported that nanometer-sized NiO precipitates form at the LNO/STO interface due to the difference in polarity. [59] These precipitates have not been observed in MBE-grown samples (Fig. 4.17. A possible explanation is the difference in deposition sequence. During a laser pulse La, Ni and O are deposited simultaneously on the substrate. The electric potential at the polar interface is not screened so NiO is a favored phase, and precipitates form irreversibly. During thermal evaporation the first La layer is deposited before any Ni is deposited. The LaO layer acts as buffer that reduces the driving force for the formation of NiO precipitates. Instead, a smooth layer forms and the polar discontinuity can be alleviated through, e.g., the formation of oxygen vacancies.

The local scale differences observed by TEM of samples grown by MBE and PLD explain differences observed in their transport properties. Note that the resistivity measurements were performed on thinner superlattice samples, 3x(4//4) structures,

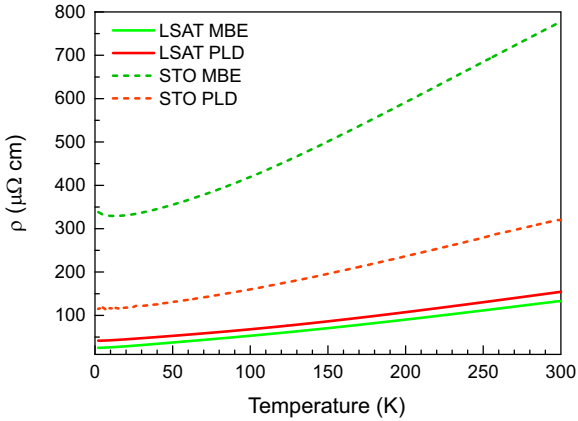

Figure 4.18: Resistivity of four 3x(4//4) SLs grown by MBE (green) and PLD (red) on LSAT (solid line) and STO (dashed line). The corresponding room temperature resistivities are 133 (MBE, LSAT), 155 (PLD, LSAT), 778 (MBE, STO) and 320 (PLD, STO) $\mu\Omega$·cm. The residual resistivity ratios (RRR, $[\rho_{300K}/\rho_{4K}]$ or $[\rho_{300K}/\rho_{min}]$ if the resistivity shows a minimum) are 5.3 (MBE, LSAT), 3.7 (PLD, LSAT), 2.4 (MBE, STO) and 2.8 (PLD, STO), respectively. All samples remain metallic down to low temperatures.

representing the well-ordered part of the samples with no or little RP faults. The resistivity of the PLD sample grown on LSAT is higher than its MBE equivalent (see Figure 4.18). Moreover, it shows a minute upturn at low temperatures that is not present in the MBE sample. This is also reflected in the residual resistance ratio [ρ(300K)/ρ(2K)] (RRR) which is higher for the MBE sample (5.3 vs. 3.7). A 25 u. c. thick film grown by MBE shows an RRR as high as 18.4 and a room temperature resistivity as low as 78 $\mu\Omega$·cm (see Figure 4.8) which exceeds previously reported values for both ceramic and thin film samples. [7, 8]

Apparently, the presence of 3D-RP faults does not significantly influence the electric transport which can be explained by the fact that the faults rarely start at the sample-substrate interface but mostly after 16 unit cells. Moreover, the size of the faults is larger than the mean free path determined for similar superlattices. [1] On the other hand, the PLD sample shows a higher interface roughness and less homogeneity which obviously increases resistivity.

The resistivity of the MBE grown superlattice on an STO substrate is strongly en-

hanced compared to the PLD analogue, possibly related to the formation of oxygen vacancies in the vicinity of the substrate. LNO grown on STO creates a polar interface which leads to the formation of NiO precipitates in PLD-grown samples but not in MBE-grown samples. Hence, another mechanism to avert the polar catastrophe is required. Since LNO is, in general, prone to the formation of oxygen vacancies, it appears likely that they indeed form. Possibly, the first four u.c. of LNO are affected. Oxygen vacancies in the LAO layers appear unreasonable. In this scenario, the first 4 u.c. of LNO form a dead layer that does not conduct electricity. If one assumes an overall reduced thickness of the conducting layers (12 u.c. LNO versus 8 u.c.) to calculate the resistivity, the remaining 8 u.c. have a resistivity of ~220 $\mu\Omega$·cm which is still significantly higher than the resistivity of the PLD sample. Moreover, comparing the RRR values of both samples, which are unaffected by uncertainties regarding the thickness of the conducting layer, one finds that the RRR value of the PLD sample is higher. Hence, the oxygen vacancies at the interface alone cannot explain the different resistivities.

In addition, the oxygen vacancies at the interface between substrate and sample can lead to inhomogeneities also in the top layers of the sample and thus giving a possible explanation for the high resistivity of the MBE sample.

Another possible origin is the less well controlled La:Ni ratio. Zhu et al. [73] made the observation that $LaNi_{1-x}O_3$ films grown by PLD on STO show an order of magnitude higher resistivity when grown slightly nickel deficient (x = 0.02 and 0.08) compared to films with an excess of nickel (x = -0.2). They speculate that the existence of a small number of nickel vacancies influences the resistivity of samples grown under large tensile strain much more than under compressive or small tensile strain, a scenario which would also explain the elevated resistivity of the MBE sample grown on STO compared to the one on LSAT.

To further explore the differences and similarities between the two growth methods, x-ray absorption spectra at the nickel $L_{2,3}$-edges were taken with linearly polarized light (Figure 4.19). It is visible at first glance that there is a considerable difference in the lineshapes between PLD and MBE samples. The L_3-edge consists of two main peaks. In the MBE samples these two peaks appear to be equal in intensity whereas the peak at lower energies is strongly reduced in PLD samples. Moreover, the shoulder

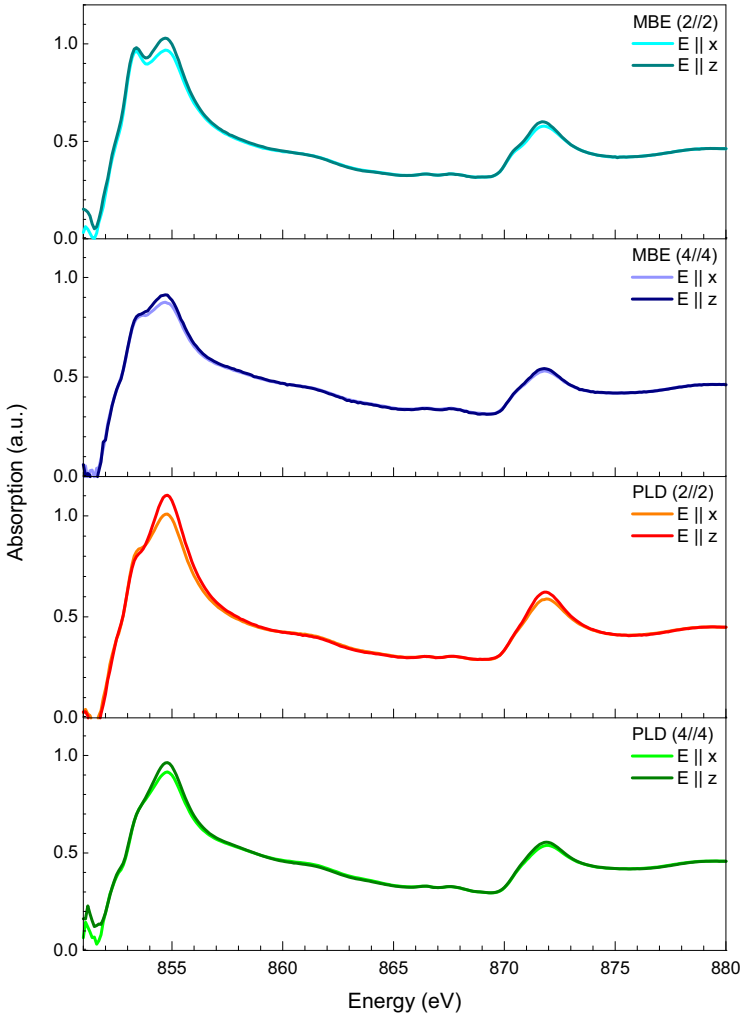

Figure 4.19: XAS spectra for E || x (in-plane) and E || z (out-of-plane) at the Ni $L_{2,3}$-edges of four samples: 8x(4//4) and 20x(2//2) superlattices either grown by MBE or PLD.

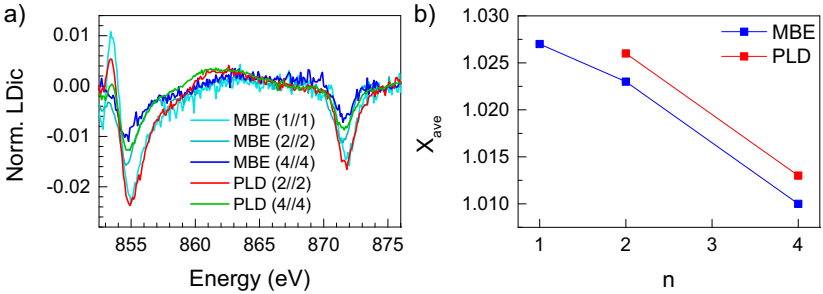

Figure 4.20: a) Normalized dichroic signal $[I_x(E) - I_z(E)]/[(2 \cdot I_x + I_z)/3]$ at the Ni $L_{2,3}$-edges for the same samples as in Figure 4.19 plus an MBE-grown 40x(1//1) SL. The signal is smaller for the MBE samples than for the PLD samples. b) Average hole ratios X_{ave} derived from the sum rules (Equation 3.8) for the same samples as in a) where "n" denotes the nickelate layer thickness.

on the low-energy side of the L_2-edge is more pronounced in the MBE samples. The features observed in the MBE samples are often related to an oxidation state lower than +III (see Chapter 5.3.1).

However, the lineshapes of other bulk samples in the series of *RE*NiO_3 are quite similar to our MBE samples. [67–69] Moreover, the low resistivity of the MBE samples basically rules out a significant contribution of oxygen vacancies. Another obvious explanation is an influence of interface roughness on the spectra. One has to consider the effect of exchanging a neighboring nickel ion for an aluminum ion on the crystal field of a nickel ion. Such an exchange can be an explanation for the observed lineshapes but theoretical calculations are needed to corroborate this idea.

From the polarized spectra, we obtained the average hole ratios, X_{ave}, via the sum rules for x-ray linear dichroism (Equation 3.8). They are shown in Figure 4.20b. The average hole ratio and therefore the orbital polarization is higher in PLD samples (see also Figure 4.20a for the dichroic signal). Since orbital polarization is an effect that is enhanced at the interface through confinement in the out-of-plane direction, one would naively expect that interface roughness lowers the orbital polarization. On the other hand, the aluminum ion that replaces a nickel ion in the case of interface roughness is smaller than nickel which possibly affects the bond angles and lengths of the Ni–O bonds. These distortions can have a similar impact as the strain exerted by

the substrate. Whether the effect of confinement in the out-of-plane direction or the distortions of the in-plane Ni–O bonds through the exchange of ions dominates is not clear a priori.

In conclusion, our comparative study of LNO-LAO superlattices grown by MBE and PLD shows the advantages and disadvantages of both methods and demonstrates the successful growth of perovskite oxide heterostructures. While the atomic layer-by-layer deposition in MBE yields on average sharper interfaces, the cation stoichiometry is more difficult to control. Depending on the chemistry of the material, the latter can give rise to a complex intergrowth of different phases, as demonstrated by the RP faults occurring in the LNO layers in the MBE film. Despite the local differences, the average electrical transport and structural properties are nearly identical for samples grown by both techniques. A significant difference regarding the lineshapes and orbital polarization is observed in XAS but its origin has to be studied in further detail.

4.4 Evolution of x-ray absorption spectra with LNO thickness

As we have already seen in the previous section (Chapter 4.3), where we discussed the difference in absorption spectra between MBE and PLD samples, there is not only an effect due to sample preparation but also related to the thickness of the LNO layer. In Figure 4.21, the polarization averaged spectra of a thin film and superlattices with decreasing thickness of the nickelate layer are shown. Both, the L_2- and L_3-edge consist of two main peaks. As the thickness of the nickelate layers is decreased, the splitting of the peaks increases, which is best visible if one takes the black, vertical lines in Figure 4.21 as a reference which indicate the peak positions in the LNO film. Moreover, the first peak at the L_3-edge (at ~853.5 eV) and the shoulder on the low-energy side of the L_2-edge become more pronounced upon decreasing the nickelate layer thickness. If one estimates the splitting based on the extremal points of the L_3 peak, one obtains values of 1.00, 0.85 and 0.80 eV for the (1//1), (2//2) and (4//4) sample, respectively.

A very similar evolution of XAS was observed for the series of RENiO$_3$ with decreasing size of the rare earth ion, RE. [67–69] A similar procedure as above gives

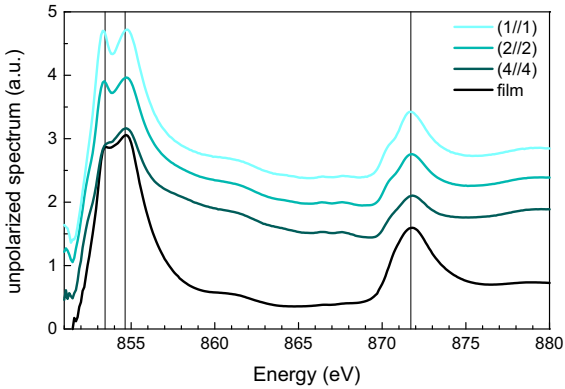

Figure 4.21: The polarization-averaged XAS spectra of samples with decreasing LNO layer thickness (22 u.c. thick film; 8x(4//4), 20x(2//2) and 40x(1//1) superlattices) show a very similar evolution as spectra of samples with decreasing rare earth ion in bulk *RE*NiO_3. The black, vertical lines indicate the peak positions of the LNO film and make the splitting of the two main peaks at the L_2- and L_3-edge better visible.

peak splittings of 1.00, 0.92, and 0.7 eV for $LuNiO_3$, $EuNiO_3$ and $PrNiO_3$, respectively.

Based on this comparison our superlattice with the thinnest nickelate layers, 40x(1//1), resembles the XAS of $LuNiO_3$ which is insulating and charge-ordered already at room temperature. [68] Although the origins of this evolution might be quite different, namely a rotation of the octahedra concomitant with a decrease of the bond angles in the case of *RE*NiO_3 and two-dimensional confinement in the case of our superlattices, it is remarkable that they resemble each other so closely.

Piamonteze *et al.* [68] attributed the evolution of lineshapes in the series of *RE*NiO_3 to a change in the value of 10 Dq, the splitting between e_g and t_{2g} states caused by the cubic crystal field, which leads to a ground state transition from a metallic, more hybridized (less $3d^7$, more $3d^8\underline{L}$ contribution) low-spin state to a mixed high-spin and low-spin, less hybridized insulating ground state with predominantly $3d^7$ character. The smaller 10 Dq in the insulating state is explained by the two inequivalent nickel sites and the overall increase of the average Ni–O bond distances. The single cluster calculation of Piamonteze *et al.* [68] shows for the full 10 Dq range considered a

dominant $3d^7$ contribution to the ground state and a significant, but smaller contribution of $3d^8\underline{L}$ and $3d^9\underline{L}^2$ states where $\underline{L}$ denotes a hole on the ligand oxygen. For the metallic state, which has a large 10 Dq, the contributions of $3d^7$ and $3d^8\underline{L}$ are almost equal. Novel models, however, treating nickelates based on a negative charge transfer energy, show a dominant $3d^8\underline{L}$ contribution to the ground state. [13]

Moreover, a charge-ordered state (site- or bond-centered) has been proposed for insulating rare earth nickelates and is nowadays widely accepted to be the origin for the MIT although its true nature is still under debate. [13, 65, 69, 74]

Recently, Lu *et al.* [75] studied a (2//2) SL (comprised of LNO and LAO grown by PLD on STO) with resonant x-ray scattering at the nickel *K*-edge and found a rigorous upper bound for the bond disproportionation of 0.01 Å. Since our SLs are quite similar to the ones studied by Lu *et al.*, we do not expect any charge order. Yet, the (1//1) superlattices are insulating and it is obvious that the charge carriers are localized. This may lead to the observed evolution of absorption spectra upon decreasing the nickelate layer thickness.

The second apparent effect upon decreasing the nickelate layer thickness is the increase of orbital polarization. Through the decrease of the nickelate layer thicknesses and through sandwiching them between an insulator, the hopping in that direction is suppressed, i.e., the electrons are confined in two dimensions. The in-plane delocalization and the out-of-plane localization lead to a stabilization of the in-plane-orbital. This effect acts in addition to epitaxial strain and Chaloupka *et al.* [3] and Hansmann *et al.* [4] predicted a large orbital polarization for (1//1) superlattices in a magnitude of 70:30 or 80:20 (= population of the $3d_{x^2-y^2}$-orbital : population of the $3d_{x^2-y^2}$-orbital) and a single-sheeted Fermi surface as in the cuprates. Moreover, Han *et al.* [76] suggested a strong influence of the separating insulator on orbital polarization. Such high values have never been reached in experiment. [16, 17, 77] Neither do the samples presented here get close to these values.

In the course of this work, we obtained an average hole ratio, X_{ave}, of at most 1.027 (Figure 4.20) which is equivalent to an orbital polarization, *P*, of about 4% whereas the values predicted by Hansmann *et al.* [4] are an order of magnitude larger.

Apparently, antagonistic effects are at work. Hansmann *et al.* [4] assumed a d^7 configuration whereas theory and experiment suggest an admixture of a $d^8\underline{L}$ state where $\underline{L}$

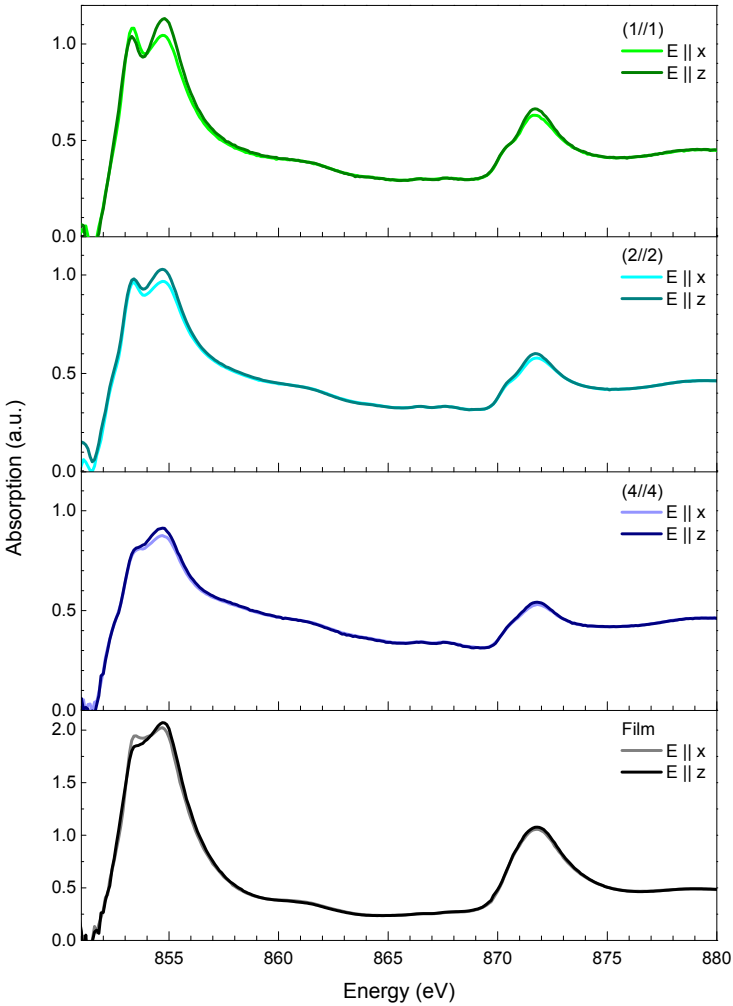

Figure 4.22: XAS spectra for E || x and E || z of samples with decreasing LNO layer thickness (22 u.c. thick film; 8x(4//4), 20x(2//2) and 40x(1//1) superlattices).

denotes a ligand hole. [13, 67, 78–80]. This state does not have any orbital polarization

and the initially assumed value has to be reduced accordingly.

In summary, we observed that the evolution of lineshapes with decreasing nickelate layer thickness in our superlattices follows a similar trend as the lineshapes of rare earth nickelates with reducing the size of the rare earth ion. The orbital polarization is small but increases upon decreasing the nickelate layer thickness.

4.5 Transport coefficients of a pure LNO film

In the present chapter, we will leave the discussion on superlattices and instead go back to an LNO thin film. The scaling of the resistivity ρ with temperature is closely related to the different types of scattering events that may happen to electrons. In an ordinary metal, the dominant scatterers are phonons or impurities but in correlated metals electrons can, for example, scatter from each other or from magnetic fluctuations if present. Therefore, the scaling of resistivity with temperature allows for conclusions on electronic correlations.

A prerequisite for such a study are high quality samples to minimize the contribution of impurities. Although their contribution to the resistivity is usually constant with respect to temperature, the impurities can lead to localization effects at low temperatures which perturbs the proper determination of the scaling coefficient. The thin film that was measured to obtain the data presented in this chapter is of such a high quality. But before we turn towards the data and its analysis, we need to briefly recall some useful relations.

As discussed earlier (Chapter 3.2.1), resistivity originates from different types of scattering. According to *Matthiessen's rule* these types contribute independently to the resistivity. [32]

$$\rho = \rho_1 + \rho_2 + ... \tag{4.1}$$

Alternatively, this rule can be written in terms of the relaxation time:

$$\frac{1}{\tau} = \frac{1}{\tau_1} + \frac{1}{\tau_2} + ... \tag{4.2}$$

In normal metals the main contribution to scattering are imperfections in the crystal

lattice, either originating from structural defects and impurities or phonons. Due to the Pauli exclusion principle electron-electron interactions may be neglected in many cases. Scattering from structural defects and impurities is in general temperature independent. As a consequence, resistivity is constant at very low temperatures when no phonons are excited and at higher temperatures its temperature dependence is governed by the phonon contribution. According to Bloch-Grüneisen law, the contribution of phonons to resistivity scales with T^5 at low temperatures and with T at high temperatures. The temperature, which is dividing the two sections of the diagram, is the Debye temperature Θ_D.

In some materials, i.e., correlated electron systems, the interactions between electrons become so strong that the above mentioned assumption does not hold anymore and the electron-electron scattering becomes the dominating contribution to resistivity at low temperatures. At high temperatures, the scattering off phonons will always be dominant. Instead of treating particles and interactions individually, one can consider "dressed" quasiparticles with renormalized properties, e.g., an effective mass $m^* \geq m$ rather than the electron mass m. [32, 81] If these quasiparticles behave equivalent to independent electrons, one speaks of a *Fermi liquid* (FL) and the contribution of quasiparticle-quasiparticle scattering to resistivity scales with T^2. Although this description appears to be a very crude approximation at first glance, it holds for a wide range of metals.

There are, however, numerous examples where the Fermi liquid theory breaks down. Any kind of static order like magnetism or charge order does not comply with Fermi liquid-like behavior. But already before static order sets in, materials that are close to such a transition might behave in a "strange" way and are called *strange metals* or *non-Fermi liquids* (NFL). There is no general description for the behavior of such materials. However, theories for certain kinds of non-Fermi liquids do exist. For example, a $4/3$- (2D) or $5/3$-scaling (3D) of the resistivity with temperature is predicted in the case of a *Pomeranchuk instability*. [82] Furthermore, Rosch proposed, for the case of a nearly antiferromagnetic metal, a scaling of the resistivity with $3/2$ at very low temperatures that comes along with a scaling of the magnetoresistance with B^2 at low fields, with B at intermediate fields and which saturates at high fields. [83]

Turning now to examples of $LaNiO_3$ that were reported in literature, one finds dif-

fering reports for the scaling behavior. Let us first have a look on *bulk ceramic* samples. Several groups found that ρ is proportional to T^2 at low temperatures. [7, 84, 85] However, they disagree on the temperature T^* below which this scaling law is valid. Values for T^* are 50 K, 80 K and 30 K, respectively. Moreover, Gayathri *et al.* [9] observe an exponent of 1.5 over the whole temperature range. However, sample quality varies significantly. Judging by the room temperature resistivity and the residual resistance ratio (RRR), the data presented by Zhou *et al.* [7], who observed a T^2-scaling below 30K̇, are the most reliable (for an overview see Table 4.1).

For *thin films* of 100 Å grown under tensile and compressive strain, i.e., on $LaAlO_3$, LSAT and $DyScO_3$ substrates, Son *et al.* [5] found a T^2 scaling up to temperatures of 80 K. Scherwitzl *et al.* [6], who investigated 35 Å thick films grown on STO, observed a T^2 scaling, however, only below 25 K. On the contrary, Moon *et al.* [86] fitted their data with a scaling law that includes, in addition to the T^α-term, a term correcting for weak localization and another term for electron-electron interactions (Equation 4.3).

$$\rho(T) = \frac{1}{\sigma_0 + a_1 T^{p/2} + a_2 T^{1/2}} + AT^\alpha \tag{4.3}$$

Here, a_1 accounts for 3D weak localization (WL). 2D WL would follow a logarithmic temperature dependence. [87] The criterion for three-dimensionality is that the inelastic scattering length is smaller than the system size. The parameter a_2 in Equation 4.3 accounts for electron-electron interactions. Following this procedure, Moon *et al.* [86] attained a temperature exponent of about $\alpha = 1.3$.

Finally, Mikheev *et al.*, [88] included an additional term, ρ_{SAT}, which acts as a parallel resistor, in their fitting procedure (Equation 4.4) and they find an exponent of $5/3$ for a variety of nickelate samples:

$$\rho^{-1}(T) = \rho_{NFL}^{-1}(T) + \rho_{SAT}^{-1}, \tag{4.4}$$

where

$$\rho_{NFL}(T) = \rho_0 + AT^\alpha \tag{4.5}$$

is the temperature dependence that is commonly referred to as non-Fermi liquid behavior.

Again, sample quality is an issue, especially when compared to the best bulk samples (see for comparison Table 4.1). Our films, however, even exceed the quality of the latter ones, with a room temperature resitivity of 78 $\mu\Omega$·cm and an RRR of 18.

If we aim to follow the analysis of Moon *et al.* [86], it does not make sense to include the WL term because WL would also lead to negative magnetoresistance which is not what we observe (see Chapter 4.6). With a_1 set to zero, a_2 also converges towards zero, leaving behind the standard FL scaling which, just by itself, does not lead to a good fit.

If we use instead of $(a_1 T^{p/2} + a_2 T^{1/2})$, which arises from 3D behavior, the logarithmic dependence found for 2D systems, the fit strongly deviates at low temperature.

The reason behind the failing of this fitting procedure is that both corrections to the T^{α}-term describe localization and lead to an increase of resistivity with decreasing temperature. Apparently, there is no such additional contribution to resistivity in our sample.

Also the fitting procedure used by Mikheev *et al.* [88] introduces a term that adds to the resistivity. And when fitting our data with their formula, ρ_{SAT} tends towards infinity, i.e., it is in the order of 10^{15} Ω·cm with $\alpha \approx 1.4$. That means that we can also neglect such a parallel-resistor-like contribution.

Group	ρ_{300K}	**RRR**	δ	***t* (Å)**	**substrate**	**preparation**
Sreedhar *et al.* [84]	1800	4	NA	bulk	–	via nitric acid
Xu *et al.* [85]	380	11	< 0	bulk	–	via nitric acid/ nitrates
Gayathri *et al.* [9]	790	6	0.02	bulk	–	via carbonates/ nitrates
Zhou *et al.* [7]	105	16	~0	bulk	–	high-pressure
Son *et al.* [5] / Mikheev *et al.* [88]	150	2.5	NA	100	LSAT	rf magnetron sputtering
Scherwitzl *et al.* [6]	270	2.7	NA	35	STO	rf magnetron sputtering
Moon *et al.* [86]	~500	2	NA	38	LSAT	PLD
King *et al.* [8]	140	>11	NA	95	LAO	ozone-assisted MBE
This work	78	18	NA	95	LSAT	ozone-assisted MBE

Table 4.1: Comparison of resistivity data reported in literature for $LaNiO_3$. ρ_{300K} is the resistivity at 300 K and is given in $\mu\Omega$·cm. The residual resistivity ratio (RRR) is ρ_{300K}/ρ_{4K} or ρ_{300K}/ρ_{min} if the resistivity shows a minimum. Whenever the exact values are not given in the reference, they were estimated from the presented graphs. δ is a value for the oxygen deficiency as in $LaNiO_{3-\delta}$. t is the thickness of the film samples.

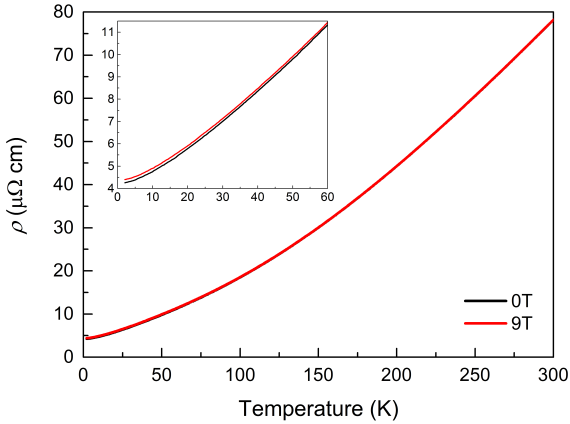

Figure 4.23: Temperature dependent resistivity ρ for a film that is 25 unit cells, i.e. ~95 Å thick. Data are shown without applied field (black) and a field of 9 Tesla applied along the surface normal (red). The inset illustrates the small, positive magnetoresistance at low temperatures.

Overall, we conclude that our sample does not follow any of the above described temperature dependencies. Hence, we chose another approach to determine the underlying scaling behavior. Without fitting a scaling law, one can calculate the exponent n in the following way:

$$\alpha = \frac{d(\log \Delta\rho)}{d(\log T)} \tag{4.6}$$

where $\Delta\rho = \rho(T) - \rho_0$. At low temperatures, Eqution 4.6 is extremely sensitive to small changes of ρ_0. To determine this quantity as accurately as possible, we measured the resistivity down to 0.4 K. These measurements were conducted by Andreas Rost (Department Takagi, MPI-FKF, Stuttgart, Germany) using a PPMS system equipped with a He^3 cryostat. The result of these measurements is presented in Figure 4.24. As we can see, the function $d(\log \Delta\rho)/d(\log T)$ is only constant below ~3 K. Above, we observe strong variations and only above ~140 K it remains close to 1.5.

Below 140 K, we also observe a suppression of charge carrier density n (see Chapter 4.6.1). The resistivity depends directly thereon and the function $d(\log \Delta\rho)/d(\log T)$ is only (approximately) constant where n is constant as well. Consequently, the change

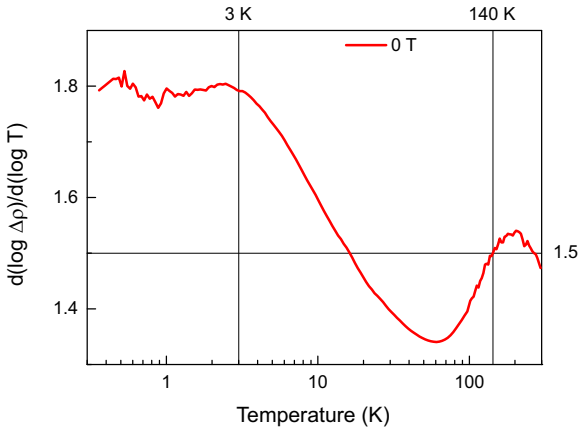

Figure 4.24: Plot to determine the scaling exponent $\alpha = d(\log \Delta\rho)/d(\log T)$ in different temperature regimes. Note that the data presented here is combined from two different data sets, one for the low- (below 100 K) and one for high-temperature regime.

of the exponent is possibly related to the change of n and one needs to find the origin of the latter before being able to draw conclusions on the former. Therefore, fitting a scaling law across the temperature regime with the changing carrier density will not yield a meaningful result.

Instead, we focus now on the regime below 3 K. For a meaningful fit of a scaling law, one should fit at least over one order of magnitude. This condition is not given here, nonetheless it is to be assumed that $d(\log \Delta\rho)/d(\log T)$ remains constant upon further cooling. At the lowest temperatures measured, we obtain an exponent of ~1.8. Although many different theories exist that predict a plethora of specific exponents, 1.8 is not among them.

One explanation could be that there is a mixing of different exponents, e.g., $\alpha = 2$ for FL behavior and $\alpha = 3/2$ for the case of a nearly antiferromagnetic metal. On the other hand, there is a theoretical prediction that suggests that in two dimensions, one can easily obtain a scaling factor that deviates from 2 although the system still behaves Fermi-liquid-like. [89] Depending on the band structure and the band filling, Buhmann *et al.* suggested that any kind of scaling exponent from about 1 to 6 is possible. [89] However, to the best of our knowledge, LNO films still maintain their

three-dimensional Fermi surface and cannot be regarded as two-dimensional.

However, there are other indications that LNO behaves like a FL. Fermi-liquid-like quasiparticles have been observed in angle-resolved photoemission spectroscopy (ARPES). [8] And the ceramic sample with the lowest resistivity and highest RRR reported in literature obeys the T^2-scaling of a FL. [7] Although the sample used for ARPES measurements was grown on LAO, which exerts a small compressive strain, and grain boundaries might affect the conductivity of the ceramic sample, they both have similar room temperature resistivities and similar RRRs as the LNO film grown under a small tensile strain investigated here. Hence, it could be that the underlying physics for all three samples are similar and that the deviation of the scaling exponent α from the FL-value of 2 originates from the two-dimensionality of the system.

To conclude, our 95 Å thick film exhibits a lower resistivity (78 $\mu\Omega$·cm) and a higher RRR (18) than any other sample reported in literature (for an overview compare with Table 4.1). [7, 8] The scaling of the resistivity with temperature does not follow that of a typical FL which would scale with T^2. Trying to fit the data with scaling laws that were used before for LNO thin films does not yield a meaningful result. [86, 88] Calculating $d(\log \Delta\rho)/d(\log T)$ with $\Delta\rho = \rho(T) - \rho_0$, which directly gives the scaling exponent α, we find that α is only constant below 3 K and above 140 K. The change of exponent with temperature is possibly related to the change of carrier density which occurs in the same temperature regime. Below 3 K, α is equal to ~1.8 which displays a deviation from typical FL-like behavior. Buhmann *et al.* [89] suggest that, in a two-dimensional system, the scaling exponent can deviate from 2 although the FL picture still holds. This interpretation is supported by ARPES data collected on an LNO film grown on LAO and by resistivity data on a bulk, ceramic sample. [7, 8] In both cases typical FL-like behavior is observed and in contrast to other examples reported in literature these two cases have similar resistivities as our sample.

4.6 Magnetotransport

Measuring electrical transport while applying a magnetic field yields information that is complimentary to the temperature dependence. In the following chapter, two phenomena will be discussed, namely the Hall effect for samples with varying nickelate

layer thickness and magnetoresistance.

4.6.1 Hall measurements

When applying a magnetic field perpendicular to the current flow the charge carriers are deflected due to the Lorentz force and a voltage can be measured that is perpendicular to both, the electric and the magnetic field (Chapter 3.2.2). In the simplest case, the change of this voltage with temperature is proportional to the charge carrier density. This relation is not valid on general grounds. In particular, a large hole Fermi surface (FS) and a small electron FS exist for LNO and naturally, one would assume that both contribute to conductivity with independent carrier densities n_i and mobilities μ_i leading to a non-trivial dependence of the Hall resistance on the magnetic field. Nonetheless, we will stick to the simple picture in the beginning and discuss deviations later on. Moreover, the Hall resistance ρ_{H}, is linear in the fields measured here. Hence, the calculation of the charge carrier density based on Equation 3.19 is at least a reasonable starting point and yields a demonstrative parameter.

We measured the temperature dependence of the Hall resistance for a series of samples with varying nickelate layer thicknesses and calculated the carrier density based on Equation 3.19, assuming that only nickelate layers contribute to conductivity and consequently we used the total thickness of LNO as the thickness t in Equation 3.18. Representative examples are shown in Figure 4.25.

All samples show a positive sign of the Hall coefficient, indicating that the majority of carriers has hole character. This observation is in agreement with most literature data where positive Hall coefficients have been reported by four groups. [5, 9, 60, 90] Only one group found a negative sign of the Hall coefficient. [54] ARPES measurements show a large hole FS (together with a small electron FS) supporting the dominance of hole conduction. [8, 91–93]

Samples with 4 or more consecutive nickelate layers show a strong, nonlinear temperature dependence of the carrier density. The room temperature value of the 25 u.c. film corresponds to a carrier density of ~2.3 holes per u.c LNO and the low-temperature value to a density of ~0.75 holes per u.c. The low-temperature behavior (below 150 K) with its strong temperature dependence resembles very closely the one reported in literature for a 2000 Å thick film grown on LAO. In the high-temperature

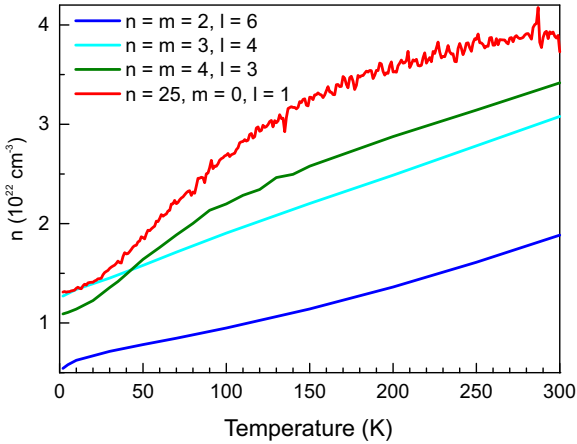

Figure 4.25: Temperature dependence of the charge carrier density n for a thin film and superlattices with different LNO thicknesses, $[(LaNiO_3)_n(LaAlO_3)_m]_l$, grown on LSAT.

regime (above 150 K) our films show a stronger increase in carrier density than the one measured by Gayathri *et al.* [9]

The temperature dependence has been either attributed to an anisotropy of the scattering times, the existence of two different carriers with a differing temperature-dependence of their scattering times or to a localization of carriers at low temperatures because of defects, for example oxygen vacancies. [5, 9, 60] We can exclude the latter based on the observation that all samples with at least 4 u.c. thick LNO layers, independent of their individual quality and independent of the growth technique (PLD or MBE), show this strong temperature dependence. Moreover, among all the sample that show the above mentioned behavior with slightly different ratios of high- to low-temperature carrier density, the sample with the highest quality, which should obviously have the lowest defect density, exhibits the most pronounced temperature dependence.

To determine the (an)isotropy of the scattering times lies without the scope of the thesis but we will discuss the possibility of two different types of charge carriers being present in LNO later on, in the second half of the present chapter.

Another possibility for the strong temperature dependence of charge carriers are

thermal excitations of charge carriers from a band that does not contribute to conductivity into the conduction band. Moreover, Allen *et al.* [94] have recently found a pseudo-gap in an LNO film grown on LAO below a temperature of 100 K. The opening of such a gap could also be connected to the reduction of charge carrier density.

Upon reducing the thickness of the LNO layers to only two u.c., the charge carrier density is strongly reduced and is less dependent on temperature. The sample with three LNO layers behaves borderline. It still shows a high charge carrier density but is as little temperature dependent as the sample with two LNO layers.

Simultaneously, we observe a clear change in resistivity between 2 and 4 unit cell thick LNO layers, while the variations are small for thicker LNO layers (Chapter 4.2, Figure 4.8). These data are in accordance with literature data that show a similar dimensional crossover. [1, 8, 95] Namely, a crossover from a paramagnetic metallic state to a weakly insulating, antiferromagnetic state has been observed in LNO-based superlattices and thin films on various substrates. [1, 2, 6] This crossover was also related to changes at the Fermi level seen in photoemission. [8, 15, 92] Although the critical thickness below which these changes occur is under dispute, similar phenomena have been observed in all experiments, on ultra-thin films and superlattices alike. While samples with thick LNO layers can be described as strongly interacting Fermi liquids, with coherent quasiparticles and 3-dimensional Fermi surfaces, the coherence is strongly reduced, the spectral weight at the Fermi level decreased and the Fermi surface becomes 2-dimensional for thin layers.

The abrupt change in carrier concentration is in contrast to a gradual reduction of carriers reported by Scherwitzl *et al.* [60] for thin films but is in good agreement with the reduction of spectral weight at the Fermi level observed in photoemission studies of superlattices by Berner *et al.* [15]

The ARPES data mentioned above show that LNO has a big hole and a small electron FS. From the Hall data in Figure 4.25 and from literature data, we know that it is mainly the holes that contribute to conductivity. To determine whether there is also a contribution from the electron FS, we conducted Hall measurements in fields up to 33 T. The measurements were conducted at the High Field Magnet Laboratory in Nijmegen, The Netherlands with a Bitter Magnet that can reach a maximum field of 33 T. We acknowledge the support of the HFML-RU/FOM, member of the European

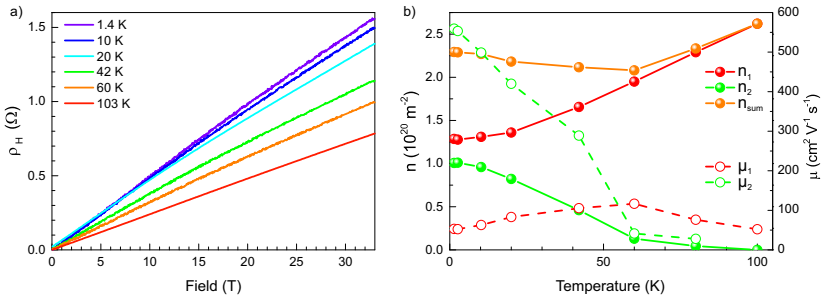

Figure 4.26: a) At high fields (we measured up to 33 T), the Hall resistance ρ_H deviates from linear behavior. b) Temperature dependence of the charge carrier densities n_1 and n_2 and their sum n_{sum} for a thin film after fitting ρ_{xy} to a two-band model (Equation 3.20) together with their mobilities μ_1 and μ_2.

Magnetic Field Laboratory (EMFL).

The results are shown in Figure 4.26a. As we can see, there is indeed a small deviation from linear behavior at high fields. This non-linearity sets in at about 20 T at 60 K.

We fitted the data with a two-band model (Equation 3.20), while fixing the longitudinal resistivity measured in zero field, $\rho_{xx,0T}$, according to Equation 3.22. Since there is only a small change in the slope, we fixed n_1 to the value obtained from a linear fit to the low-field region (below 5 T) to reduce ambiguity and to obtain a consistent fit of the data at the different temperatures.

This procedure leads to good fits of the data and its result is shown in Figure 4.26b. We see that below 100 K a second carrier type, n_2, evolves and its density rises together with its mobility. Simultaneously, the density of the first carrier type, n_1, decreases but its mobility remains constant. As we can see, the sum of both carrier types, n_{sum}, remains constant as well which leads us to the interpretation that charge carriers are transferred from the band hosting the n_2-carriers to the band hosting the n_1-carriers as the temperature is increased.

Interestingly, both carriers have hole character. Attempts to artificially introduce electrons as carriers into the equation, did not result in a good fit. Indeed, Eguchi *et al.* [91] found that the effective mass, m^*, of the electron-like band is enhanced unlike m^* of the hole-band. Later studies found that also the hole-band has an enhanced

effective mass but the authors did not elaborate on the difference between the two bands. [8, 96] Moreover, strain and strain-induced symmetry changes have a strong impact on the mass renormalization and the samples that were investigated in the references mentioned above were grown on STO and LAO, respectively. The two substrates exert tensile and compressive strain, respectively which could lead to quite different behavior. Our sample was grown under small tensile strain, namely on LSAT, and might therefore follow a behavior closer to that of the sample grown on STO that did show the electron-hole asymmetry.

To cut a long story short, ARPES measurement have shown that there is an asymmetry of the electron- and hole-like bands. [91] This asymmetry could be large enough to lead to a mass enhancement that is that much stronger for the electron band that the contribution of electrons to conductivity becomes negligible.

Although the above described interpretation is quite intriguing one has to be aware of certain pitfalls. In particular, it has been noted that one can fit a two-band model to almost any dataset while still obtaining reasonable parameters. [49] Moreover, it is a rather crude model that bears the danger of oversimplifying the sometimes complicated conduction process. In addition, the deviation from linearity is rather small and occurs only at very high fields which adds to the uncertainty.

In summary, we measured the temperature dependence of the Hall coefficient for varying LNO layer thicknesses.

For samples with at least 4 consecutive LNO layers, we observe a strong temperature dependence, implying a strong reduction of the carrier density at low temperatures. The drop of carrier density occurs simultaneously with the opening of a pseudogap that was recently observed in an LNO thin film grown on LSAT. [94]

Measurements of the Hall resistance at high fields up to 33 T show a small deviation from linearity. The data can be fitted with a two-band model which indicates a second type of charge carrier below 100 K. It is remarkable that both carriers have hole character as one would expect from ARPES experiments that both, holes and electrons, contribute to conductivity.

Superlattices with as few as two consecutive LNO layers show a strongly reduced carrier density which is less temperature dependent compared to samples with 4 or more LNO layers. ARPES data on both, thin films and superlattices, support the idea

that there is a dimensional crossover at exactly the same layer thickness. [8, 15]

To further elucidate the puzzle of the change in charge carrier density and its possible connection to the pseudo-gap, low-temperature scanning tunneling microscopy (STM) would be helpful. Due to its polar nature, the LNO surface will buckle which is detrimental STM measurements. [95] However, a single atomic layer of lanthanum oxide is enough to remove the buckling while still allowing tunneling. [97] As there appear to be significant changes of the FS with temperature, a comparison of ARPES measurements at high and low temperatures might give some new insights.

4.6.2 Magnetoresistance measurements

Within the free electron picture, a magnetic field forces electrons on helical trajectories. If the field is high enough and the sample clean enough, the electrons are able to complete a full circle before scattering occurs. This is the case when the cyclotron frequency ω_c times the scattering time τ is larger than one, where the product can be calculated in the following way: $\omega_c\tau = B/\rho_0 ne > 1$ [50]

Where B is the magnetic field, ρ_0 the resistivity without magnetic field, n is the charge carrier density and e is the elemental charge. Let us keep in mind for now that $\omega_c\tau$ is an important quantity when measuring resistance in a magnetic field, i.e., magnetoresistance (MR) and note that an ideal free electron metal does not have any MR. [50]

In a material that cannot be described within the free electron picture the trajectories do not necessarily describe helices but they may describe quite arbitrarily shaped paths that depend on the symmetry of the FS. This has an influence on the measured magnetoresistance and is the reason why this technique has been widely used to determine the shapes of Fermi surfaces (FS). [50]

Depending on the material and its purity, MR measurements can reveal other details of the electronic structure. For example, in the case of weak localization (WL) and antilocalization (WAL, Chapter 3.2.3).

In Figure 4.27, we show the change of the MR behavior – with the field applied perpendicular to the sample surface, $B \parallel c$ – for different LNO thicknesses. A thin film that is 25 u.c. thick shows a positive MR, i.e., +3.65% at 9 T. By reducing the LNO layer thickness, the MR is reduced and becomes negative for a superlattice with 4 u.c.

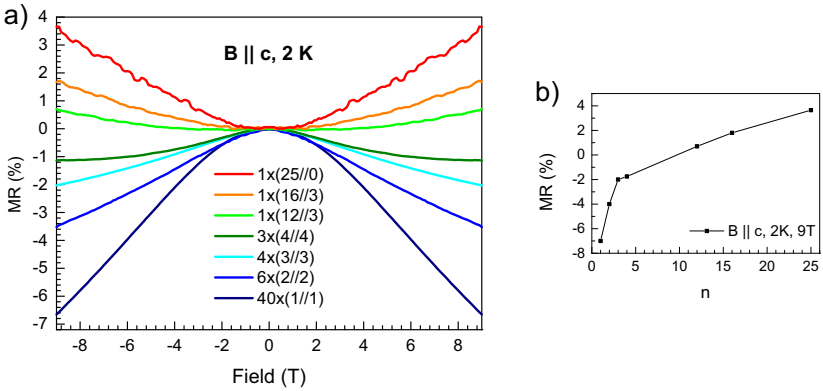

Figure 4.27: a) Transverse MR with the field applied perpendicular to the sample surface for decreasing thickness of the LNO layer at 2 K. The data of positive and negative fields were averaged to correct for the contribution of Hall resistance. b) Plot of the transverse MR, extracted from the data in a), at 2 K and 9 T against the thickness of the LNO layer.

thick LNO layers. The trend for the MR at 9 T appears to be approximately linear in thickness (see Figure 4.27b) until a layer thickness of 3 u.c. is reached. At 2 u.c., the MR drops significantly which is probably related to the onset of antiferromagnetic order since the magnetic field aligns the nickel moments which reduces scattering.

For other LNO thin films and also for bulk ceramic samples, mostly a negative, isotropic MR has been observed and was explained by 3D-WL. [5, 6, 98] There is only one report of a positive MR by Gayathri *et al.* [98] who studied the MR of ceramic bulk samples in dependence of the oxygen stoichiometry and found a positive MR at low temperatures only for their sample with highest oxygen content, i.e., $LaNiO_{2.98}$. In samples with a higher concentration of oxygen vacancies they found negative MR. The MR for the sample with the highest oxygen content is +1% at 4.2 K and 6 T. At 6 T and 2 K, our 25 u.c. film has a transverse MR of ~2.5% with the magnetic field applied along the *c*-axis and of ~3% with the magnetic field applied in the *ab*-plane (see Figure 4.28). An increase of temperature by 2.2 K should not reduce the MR dramatically. Hence, we can claim that our thin film has a similar or bigger MR. The high, positive MR of our film is another – in addition to the low resistivity and high residual resistance ratio that were discussed in Chapter 4.5 – indication for its high

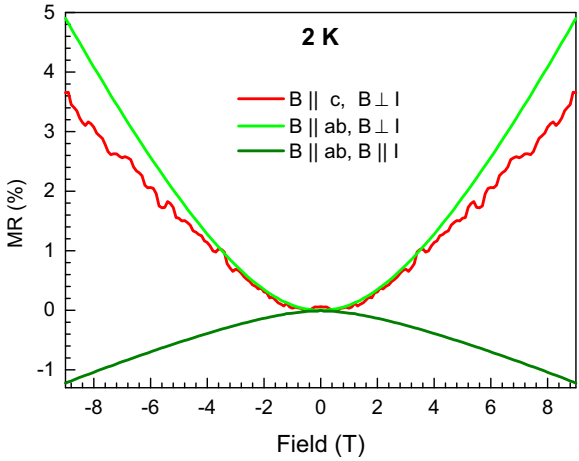

Figure 4.28: Transverse MR with the field applied perpendicular (red) and parallel (bright green) to the film surface and longitudinal MR (dark green). All curves were measured at 2 K. The data of positive and negative fields were averaged to correct for the contribution of Hall resistance.

quality and high oxygen content. Moreover, the isotropic, negative MR observed in LNO thin films was attributed to the contribution of Ni^{2+} ions to scattering. [6]

The small, negative longitudinal MR can be attributed to a finite size effect. The winding up of the electron orbits caused by the magnetic field can reduce the effect of surface scattering, giving rise to a negative MR. [50]

Lead by the hope to find quantum oscillations that are often observed in clean samples at low temperatures and high magnetic fields, namely with $\omega_c\tau \gg 1$, and that allow for conclusions on the shape of the FS, we aimed for higher fields. In the highest fields measured, i.e., 33 T, $\omega_c\tau \approx 0.4$ which is below the critical value. Reminding ourselves of the discussions in the previous chapter (Chapter 4.6.1), we know that the carrier density determined from the slope of the Hall resistance in magnetic field might not be an accurate value and that there is a second FS that could have a smaller carrier density and fulfill the criterion that $\omega_c\tau$ should be much larger than one.

The measurements were conducted at the High Field Magnet Laboratory in Nijmegen, The Netherlands with a Bitter Magnet that can reach a maximum field of 33 T. We acknowledge the support of the HFML-RU/FOM, member of the European

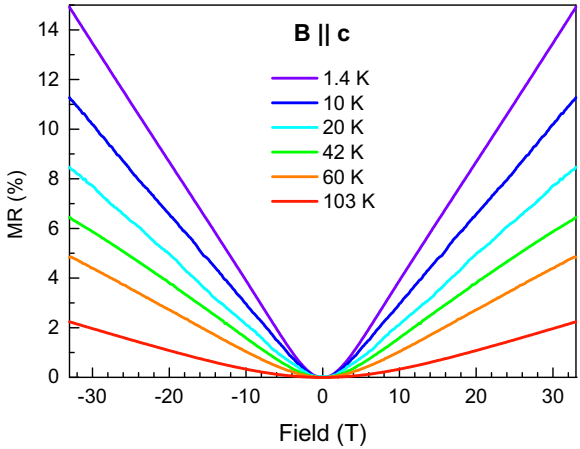

Figure 4.29: Transverse MR with the field applied perpendicular to the film surface at temperatures between 1.4 and 103 K. The data of positive and negative fields were averaged to correct for the contribution of Hall resistance.

Magnetic Field Laboratory (EMFL).

However, we did not observe any oscillations up to fields of 33 T (see Figure 4.29) with the biggest obstacle probably being the high charge carrier density. Instead, we find a resistivity that is proportional to B^2 at low fields and which is quite normal for metals. [32, 49, 50] In fact, due to the curved trajectories of the electrons, the magnetoresistance would usually rise with B^2 until it reaches $\omega_c\tau = 1$ or, in the case of an open FS, the MR would saturate at some point.

Already well below $\omega_c\tau = 1$ and without having an open FS, we observe a deviation from the usual behavior, namely a linear scaling of the resistivity with the magnetic field which does not saturate up to 33 T. This behavior is rather unusual and possible origins shall be discussed in the following.

A classical treatment of the problem leaves only one possibility for the observation of a linear MR, namely a polycrystalline sample with an open FS. [99] In the present case, however, we have a single-crystalline sample with a closed FS, ruling out this possibility.

A quantum route to linear MR, developed by Abrikosov and coined *quantum linear*

magnetoresistance, gives the following dependence of the transverse magnetoresistances ρ_{xx} and ρ_{yy}: [99]

$$\rho_{xx} = \rho_{yy} = \frac{N_i B}{\pi n_0^2 e} \tag{4.7}$$

Note that ρ_{xx} and ρ_{yy} are here the magnetoresistances and not the resistivities. N_i is the concentration of scattering centers, n_0 the carrier concentration derived from the Hall coefficient, B the magnetic field and e the elementary charge.

Two conditions need to be fulfilled for Equation 4.7 to be valid:

$$n_0 \ll \left(\frac{eB}{\hbar}\right)^{3/2}, \quad T \ll \frac{eB\hbar}{m^*} \tag{4.8}$$

$\hbar$ is the Planck constant ($\hbar = 6.626 \cdot 10^{-34}$ J· s), T is the temperature and m^* the effective mass. The first criterion requires a carrier density less than $\approx 10^{18}$ cm^{-3} and is far from being fulfilled in the case of LNO. Moreover, the enhanced effective mass m^* further hinders the fulfillment of the Equation 4.8.

Other availabe theories that predict a linear MR usually treat semiconductors and small carrier concentrations. [99–101] These conditions are not met in the case of LNO.

There appear to be only two exceptions. First, there is another theory developed by Abrikosov for the case of rare earth diantimonides, e.g., $LaSb_2$. [99] Members of this group of materials are, like LNO, metallic with large a FS but are, in contrast to LNO, layered materials with two-dimensional transport behavior (the resistivity along the *c*-axis is more than an order of magnitude higher than the resistivity within the *ab*-plane). [102] The prerequisites for the validity of this model are single crystalline metals with small pockets of FS for which the criteria requested in Equation 4.8 are fulfilled. Such pockets are most likely to occur in layered materials like graphite or rare-earth diantimonides and are unlikely to occur in LNO.

Another exception is the case of a nearly antiferromagnetic metal proposed by Rosch which is able to explain the behavior of heavy Fermion systems. [83] LNO is also close to an antiferromagnetically ordered state. Hence, the principal conditions are met. Although the observed MR is in agreement with this theory, the scaling of resistivity with temperature that is simultaneously predicted does not agree with our

measurements.

The only system reported in literature that appears to behave in a similar way as our LNO thin film is $SrIrO_3$. [103] The authors attribute the linear MR to the opening of a pseudo-gap due to large structural distortions yet the cited model is based on a gapless semiconductor with small carrier concentrations. [100] It is unclear whether the conditions required by the theoretical model are met in the case of $SrIrO_3$.

In summary, we found a positive MR of ~4% at 2 K and 9 T in a 25 u.c. thick LNO film. By reducing the LNO thickness, the MR is gradually reduced and even becomes negative due to the onset of 2D weak localization. This trend continues until a thickness of 3 u.c. is reached. Below this thickness, the effect of magnetic field increases significantly since the spins of the antiferromagnetically ordered electrons are aligned in the magnetic field which reduces scattering and therefore reduces resistivity. [1, 2]

The positive MR of the 25 u.c. thick LNO film is an indication for its high quality and oxygen content. [98]

An investigation of the MR of this high-quality film at various temperatures and high magnetic fields led to the discovery of linear MR that does not saturate, not even in a field of 33 T. At low fields the MR shows a quadratic field dependence which is expected for ordinary metals. [50] The occurrence of the linear MR is puzzling, however. After considering various theories on magnetotransport, we conclude that within the existing ones, one could only explain the observed field dependence if there were small pockets of FS where the carriers had a small effective mass m^*. [99] The small electron FS that is known to exist for LNO comprises most likely too heavy carriers. Possibly, the observed linear, non-saturating MR cannot be explained within existing theories.

4.7 Conclusions

In the present chapter, we elaborated on the MBE growth and the physical properties of $LaNiO_3$ thin films and superlattices (SLs) that consist of $LaNiO_3$ (LNO) layers with varying thickness sandwiched between an insulating layer, for example $LaAlO_3$ (LAO). Such a superlattice has the composition $[(LaNiO_3)_n(LaAlO_3)_m]_l$ or short lx(n//m) and was grown epitaxially on either $(LaAlO_3)_{0.3}(Sr_2AlTaO_6)_{0.7}$ (LSAT),

$SrTiO_3$ or $GdScO_3$ (GSO). Samples on GSO have $LaScO_3$ as an insulating layer. Because of its small lattice mismatch with LNO and LAO, most samples were grown on LSAT.

First, we showed how to optimize the growth conditions for LNO. LNO is prone to the formation of oxygen vacancies and a nickel deficiency can easily lead to the formation of other phases within the Ruddlesden-Popper series, $La_{n+1}Ni_nO_{3n+1}$. To ensure a high oxygen content, high ozone pressures and relatively low temperatures are needed. We used a chamber pressure of ~$3{\cdot}10^{-5}$ mbar and a growth temperature of ~550°C. To control the lanthanum-to-nickel ratio, we combined in-situ RHEED with ex-situ feedback measurements, i.e., x-ray diffraction (XRD), their x-ray reflectivity (XRR), atomic force microscopy (AFM) images of their surfaces, transport properties, transmission electron microscopy (TEM) images and x-ray absorption spectroscopy (XAS). The studied characteristics lay the basis to judge the quality of a film or a superlattice.

Overall, we can confirm the behavior that was reported in literature for similar samples grown by other deposition techniques, i.e., pulsed laser deposition (PLD) and off-axis rf magnetron sputtering. Namely a dimensional crossover from a paramagnetic, metallic state to a weakly insulating, antiferromagnetic state upon reducing the thickness of the LNO layers. [1, 2, 5, 6, 8] Moreover, we also observe an increased occupation of the $3d_{x^2-y^2}$-orbital with respect to the $3d_{3z^2-r^2}$-orbital, i.e., an increased orbital polarization, upon increasing tensile strain. [16, 17]

Compared to samples reported in literature, our films and superlattices show a lower resistivity and a higher residual resistivity ratio (RRR, $\rho_{300\,K}/\rho_{4\,K}$) which indicates a high sample quality. [5, 8, 86, 95] In particular, our LNO film with the highest quality shows a room temperature resistivity of 78 $\mu\Omega$·cm and a RRR of 18 and thereby exceeds any other values reported before, even that of bulk, ceramic samples. [7, 8] Moreover, we observe a positive magnetoresistance (MR) in our thin films which is indicative of a high oxygen content whereas so far, only a negative MR, which is indicative of oxygen vacancies, has been observed in LNO thin films. [5, 6, 98]

To investigate the influence of the growth technique on the sample quality, we chose to grow nominally identical samples by PLD and MBE. The PLD samples were grown by Georg Christiani in collaboration with the Technology Group, MPI-FKF, Stuttgart,

Germany. Their properties widely agree with respect to XRD and XRR. TEM images show a slightly higher interface roughness and less homogeneity for the case of the PLD samples likely due to the high deposition energy during PLD growth. In MBE samples, and very rarely in PLD samples, we observe 3D-Ruddlesden-Popper faults, i.e., shifts of the SL by half a unit cell in growth direction due to an extra layer of lanthanum oxide. These faults reflect an offset in the lanthanum-to-nickel ratio and it is reasonable that they are less abundant in PLD samples where the stoichiometry is better determined by the target. Moreover, in contrast to PLD samples shown in literature, [59] we do not observe nickel oxide precipitates at the interface between STO and LNO superlattices. The resistivity for an MBE sample grown on LSAT is slightly lower than for a nominally identical PLD sample, indicating better structural quality and / or a higher oxygen content. The resistivity of an MBE-grown superlattice on STO is, however, higher than for the corresponding PLD sample. In the absence of nickel oxide precipitates, possibly oxygen vacancies are formed at the interface between STO and the superlattice, leading to a higher resistivity. The biggest difference is yet observed in XAS. There is a remarkable difference in the lineshapes between MBE and PLD samples. Moreover, the orbital polarization is higher in PLD samples. Both effects are probably related to interface roughness and not to oxygen vacancies. An exchange of a neighboring nickel ion for an aluminum implies a change of the coordination geometry which will modify the lineshapes and orbital polarization.

Continuing with the XAS studies, we investigated the changes in the spectra upon reducing the LNO thickness. The evolution of the lineshapes is similar to the series of rare earth nickelates (RENiO$_3$) with reducing the size of the rare earth ion, [68, 69] namely an increased splitting of the two main features at the nickel L_3-edge. The origin of this transition is quite different for the two cases, a change in bond angles and charge ordering in the case of RENiO$_3$ and a localization of carriers without charge order upon reducing the LNO thickness. The confinement in one direction, leads to a localization of carriers along that direction and a delocalization in the other direction which, in turn, leads to a stabilization of the in-plane orbital. The observed polarization is rather small compared to values predicted by theoretical calculations. This discrepancy is likely due an admixture (or even prevalence) of a $3d^8\underline{\mathrm{L}}$ state, where $\underline{\mathrm{L}}$ denotes a hole on the ligand and a $3d^8$ ion does not have any orbital polarization in the

ground state.

Temperature dependent, electrical transport shows a deviation from the typical Fermi liquid (FL) behavior. Instead of a scaling of the resistivity with T^2, we find that the resistivity scales with $T^{1.8}$ below 3 K followed by a wide transition temperature regime where one cannot find a constant scaling exponent before the resistivity scales with $T^{3/2}$ above ~140 K. This behavior does not comply with any theory predicting a specific exponent. However, Buhmann *et al.* [89] argue that one can obtain scaling exponents between 1 and 6 in a two-dimensional system and within the FL theory.

Hall measurements show hole-like carriers with a strong temperature dependence of the charge carrier density for samples with at least 4 u.c. of LNO. High-field measurements and a fit to a two-band model indicate the presence of a second type of charge carrier, also with hole character. It is well-accepted that LNO has a large hole and a small electron Fermi surface (FS). Hence, one might have expected also the contribution of electrons to conductivity. This is not the what we observe.

Upon reducing the thickness of the LNO layer such that only two consecutive layers remain, we observe a sharp decrease of the charge carrier density. This change occurs simultaneously with the sharp increase in resistivity, the onset of magnetic order and an enhanced negative MR. The reduction of carrier density is another hint for the dimensional crossover in the LNO system.

The MR is positive for a thin film of 25 u.c. and gradually decreases with decreasing LNO thickness, probably because of the onset of weak localization (WL). Yet, there is a sharp drop in MR when going from a 3 u.c. sample to a 2 u.c. sample.

The MR of the thin film increases with B^2 at low fields and linearly at high fields without saturating. Whereas the former is a behavior that is expected and often seen in metals, the linear MR without saturation is unusual. Within the existing theories, it can only be explained in case of a small FS pocket with carriers that have a small effective mass.

Chapter 5

Nickelate-cuprate hybrid structures: Design and characterization of a novel material

In the previous chapter, materials were investigated that had already been grown before by other depositon techniques. Here, we demonstrate to show that the growth method does not only have an influence on sample quality but that by exploiting the versatility of the MBE system it is possible to design novel, artificial materials on the atomic scale.

The present chapter is dedicated to such a novel structure type, namely hybrid structures consisting of cuprate and nickelate layers separated by one ore two lanthanum oxide layers where the thickness of cuprate and nickelate layers is varied. As can be seen in Figure 5.1, which shows a stereotypical unit cell (a) and the corresponding layer sequence (b), the cuprate layers are separated from each other and from the nickelate layers by two lanthanum layers. That means that their direct chemical environment is the same as in La_2CuO_4. On the contrary, the inner nickelate layers are separated by only one lanthanum oxide layer, setting them in the same local chemical environment as in $LaNiO_3$. The outer nickelate layers are separated from the cuprate layers by two lanthanum oxide layers which means that on the side pointing towards

the cuprate layer they have an environment as in La_2NiO_4 and on the side pointing towards the nickelate layer as in $LaNiO_3$. Overall, the structure of the nickelate layers resembles that of the Ruddlesden-Popper phases (RP phases). Figure 5.2 illustrates how $La_5Ni_4O_{13}$ (a) and La_2CuO_4 (b) form $[(La_2CuO_4)_2LaO(LaNiO_3)_4]$.

Attempts were made to grow structures where the last cuprate layer is separated from the following nickelate layer by only one lanthanum oxide layer. However, it was observed in TEM images that in these cases the layers rearrange in such a way that one cuprate layer is always surrounded by two lanthanum oxide layers. The preference of the 214-structure over the perovskite 113-structure in the case of lanthanum cuprate can be easily understood if one realizes that $LaCuO_3$ requires high temperatures and pressures to grow. [7, 104]

The properties of this novel, layered strucure are investigated thoroughly. One question that shall be answered in this chapter is whether the nickelate and cuprate layers are decoupled and behave as in the corresponding RP phases and in La_2CuO_4, respectively or whether they interact with each other.

5.1 Growth

In Chapter 4.1, it was described how to optimize the growth of $LaNiO_3$–$LaXO_3$ (X = Al, Sc) superlattices. In principle, the central points still hold true for the system discussed in the present chapter. That means that one has to find the optimal parameters for oxygen/ ozone pressure, temperature and cation stoichiometry and the standard tools for judging the sample quality are RHEED, AFM, XRD, XRR and electrical transport measurements. Similarities and differences in growth optimization will be discussed in the present section.

The first difficulty in growing the nickelate-cuprate hybrid structures is that one has to bring two materials together that grow under different conditions. In the previous chapter, we adjusted only the growth conditions for $LaNiO_3$ and luckily $LaAlO_3$ and $LaScO_3$ grow well for a wide range of parameters. This is not the case in the present example. Both materials grow at chamber pressures – i.e., a mixture of ozone, molecular oxygen and oxygen radicals – of ~$3 \cdot 10^{-5}$ mbar but require quite different temperatures. LNO grows best at low temperatures of ~550°C, forms oxygen vacancies above

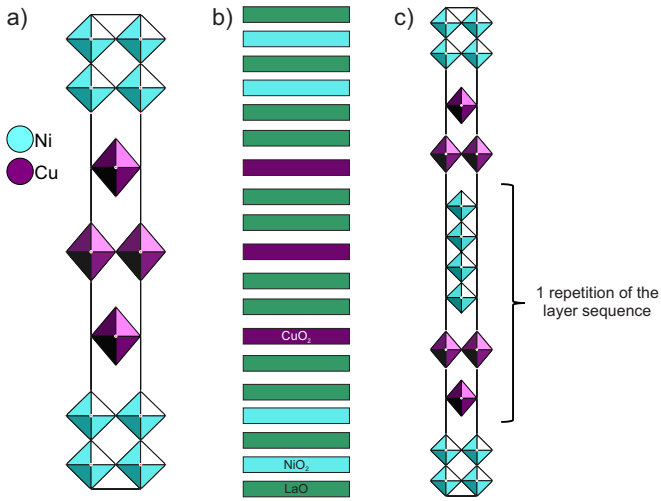

Figure 5.1: a) Sketch of a stereotypical unit cell of a lanthanum cuprate – lanthanum nickelate hybrid structure. Copper-oxygen octahedra are drawn in purple and nickel-oxygen octahedra in blue. Lanthanum and oxygen atoms are omitted for clarity. b) Corresponding atomic layer sequence of the structure depicted in a). Lanthanum oxide layers are shaded in green, nickelate layers in blue and cuprate layers in purple. c) The thickness of nickelate and cuprate layers was varied in order to determine the influence on physical properties. Note, that for an even number of cuprate layers, the nickelate layers above and below are shifted by $\left(1/2\,\vec{a} + 1/2\,\vec{b}\right)$ with respect to each other. This leads to a doubling of the unit cell in c direction as can be seen in the structure shown here.

and decomposes into La_2NiO_4 and NiO at high temperatures. La_2CuO_4 however, requires rather high temperatures of at least 630°C. We chose a growth temperature of about 600°C and a pressure of $3 \cdot 10^{-5}$ mbar for our samples, knowing that these conditions can lead to the formation of oxygen vacancies, especially in the nickelate layers.

Besides the difficulty to find the right growth conditions, the adjustment of stoichiometry is at least as challenging as in the $LaNiO_3$–$LaXO_3$ superlattices discussed in the previous chapter. Here, the approach to find the correct shutter opening times was to first grow single films of La_2CuO_4 and $LaNiO_3$. As in the previous example (Chapter 4.1), we kept the shutter opening time for lanthanum constant at the value determined by QCM calibration and varied the shutter opening time for the B site cation

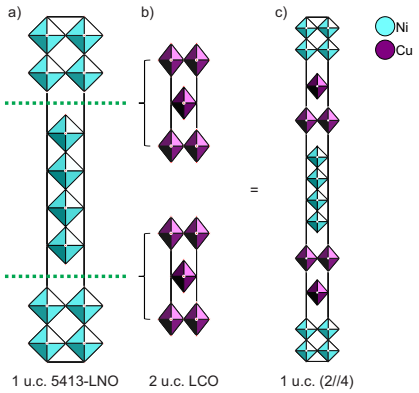

Figure 5.2: Sketch to illustrate how one u.c. of $La_5Ni_4O_{13}$ (a) and 2 u.c. of La_2CuO_4 (b) form one u.c. of $[(La_2CuO_4)_2LaO(LaNiO_3)_4]$ (c). Ni and Cu octahedra are drawn in blue and purple, respectively.

such that RHEED amplitude and intensity are maximal. In this way, we obtained optimal rates, r_{opt}, for copper and nickel. We then used these values to grow the hybrid structures.

Excursion: Growth of the Ruddlesden–Popper series, $La_{n+1}Ni_nO_{3n+1}$

To crosscheck, we used the same approach to grow the Ruddlesden–Popper series of lanthanum nickelate, i.e., $La_{n+1}Ni_nO_{3n+1}$ (with n = 2, 3 and 4). That means, we found r_{opt} by growing an LNO thin film and then repeated a sequence of, e.g., La–La–Ni–La–Ni to obtain $La_3Ni_2O_7$. These structures grow in a high quality which will be discussed in the following sections.

Note here that Lee *et al.* [105] claimed that it is impossible to grow the members of the RP series by depositing the atomic layers in the sequence as they will occur in the final structure. They showed through theoretical calculations and in-situ x-ray diffraction experiments that the layers will always rearrange in a way such that the top layer is lanthanum oxide and the one next to it is nickel oxide. For example, if one grows a sequence of La–La–Ni, the layers will rearrange and form instead La–Ni–La. They conclude that one has to deposit a sequence of La–La–La–Ni–Ni in order to

grow $La_3Ni_2O_7$. Our results disagree with their conclusion. We could show that by setting the shutter opening times for nickel correctly it is possible to use the "natural" layer sequence and still obtain high-quality $La_{n+1}Ni_nO_{3n+1}$ with $n = 2$, 3 and 4. Their diffraction patterns will be shown and discussed in the following section (Chapter 5.2, Figure 5.8).

RHEED during LNO–LCO deposition

For this kind of structure, one has to rely more or less on the rates obtained from growing an LCO or LNO thin film since the RHEED oscillations are even more ambiguous as in the case of LNO-LAO SLs.

Figure 5.3a shows RHEED oscillations for the growth of $[(La_2CuO_4)_3LaO\text{-}(LaNiO_3)_4]_6$. For comparison, RHEED oscillations and images for a sample that was not grown in optimal stoichiometry are shown in Figure 5.4.

In Figure 5.3 and Figure 5.4, we can see that the intensity of the directly reflected beam is in general lower for the LCO layers than for the LNO layers. The reason

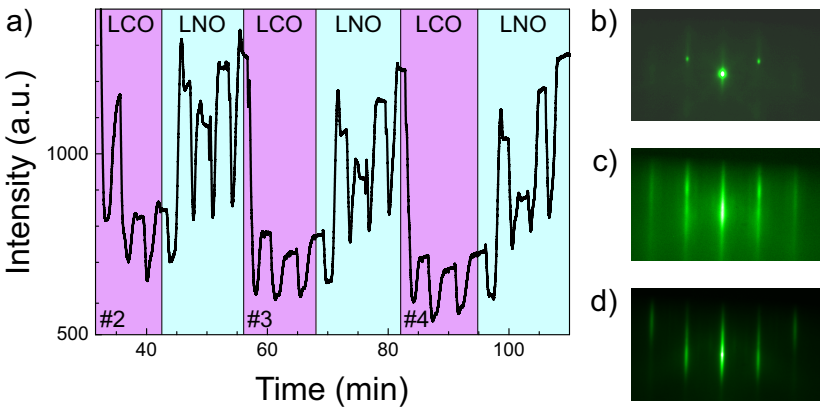

Figure 5.3: a) RHEED intensity oscillations of the directly reflected beam observed during the growth of $[(La_2CuO_4)_3LaO(LaNiO_3)_4]_6$. Out of the six repetitions, only the second to fourth (indicated by the numbers # 2 – # 4) are shown for clarity. Purple-shaded areas mark the deposition of La_2CuO_4 and blue-shaded areas mark the deposition of $LaNiO_3$. b) RHEED image of the as-received LSAT substrate at growth temperature. c) RHEED image at the end of La_2CuO_4 deposition. d) RHEED image at the end of the growth.

behind could be a surface reconstruction. Indications for such a surface reconstruction are the additional streaks between the (00) and (01) trunkation rod (Figure 5.3c).

What is puzzling about the oscillations during nickelate deposition is that the second nickelate layer is always reduced in intensity which could be related to a layer rearrangement or a surface reconstruction. At the end of the fourth nickelate layer, the intensity of the reflected beam is high, the additional streaks between the (00) and (01) rods are barely visible and the rods appear very sharp (Figure 5.3d). These are indications for coherent diffraction from a smooth surface and hence for a well ordered heterostructure.

On the contrary, if samples were found by XRD to be of low quality and to contain impurity phases, their truncation rods had been very broad at the end of the growth. Figure 5.5 shows such broad truncation rods (a&b) and the corresponding XRD pattern (c). Figure 5.6 compares line profiles parallel and perpendicular to the truncation rods of two samples, 6x(3//4) and 7x(2//2). The first sample, 6x(3//4), shows high structural quality when probed by XRD and the rods are sharper than for the second

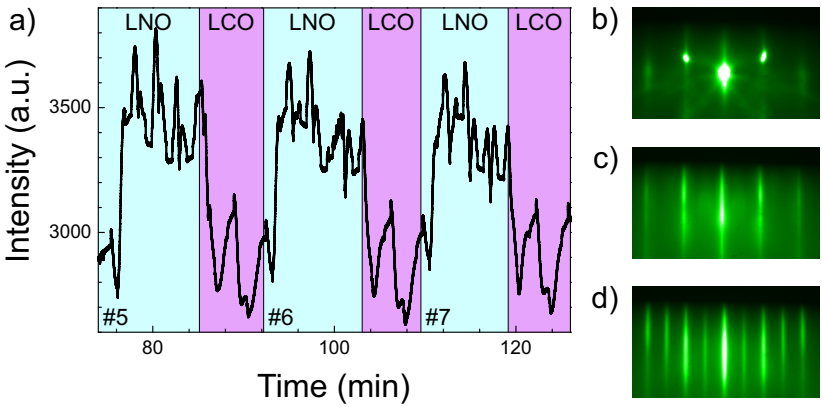

Figure 5.4: a) RHEED intensity oscillations of the directly reflected beam observed during the growth of $[(LaNiO_3)_4(La_2CuO_4)_2]_{10}$. Out of the ten repetitions, only the fifth to seventh (indicated by the numbers # 5 – # 7) are shown for clarity. Purple-shaded areas mark the deposition of La_2CuO_4 and blue-shaded areas mark the deposition of $LaNiO_3$. b) RHEED image of the as-received LSAT substrate at growth temperature. c) RHEED image at the end of La_2CuO_4 deposition. d) RHEED image at the end of the growth.

sample, 7x(2//2) which shows impurity phases and asymmetric peak shapes in XRD (Figure 5.5c).

It is advisable to adjust the shutter opening times towards the end of a lanthanum cuprate or lanthanum nickelate sequence, respectively. If there is a surplus or deficiency of the *B* site cation, the off-stoichiometry of the individual layers will add up and towards the end of the sequence the tendency whether there is a surplus or deficiency will be more evident.

Moreover, if the shutter in front of an effusion cell is closed for a long time, i.e., while the respective other *B* site cation is deposited, vapor pressure builds up which is released as soon as the shutter is opened again. As a consequence, more material is deposited in the first layer than in the following although the shutter opening time

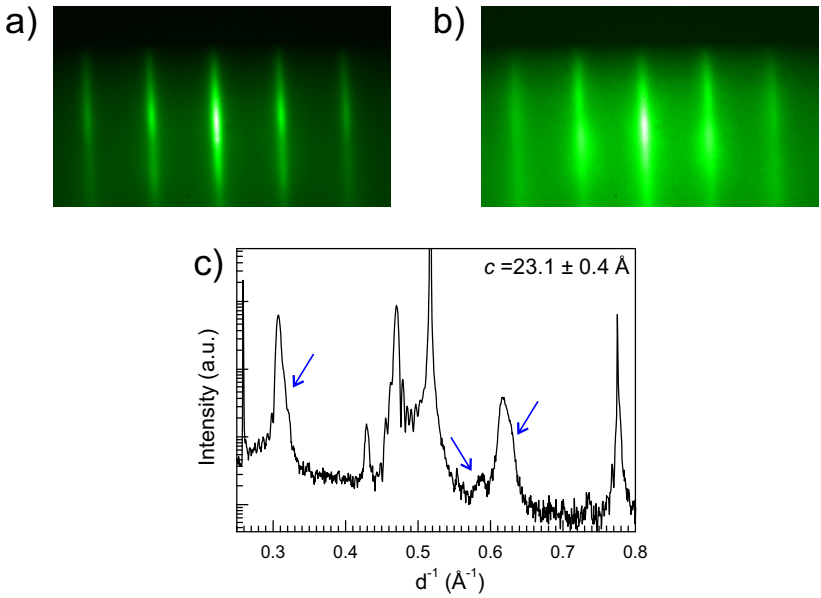

Figure 5.5: Growth of $[(La_2CuO_4)_2LaO(LaNiO_3)_2]_7$, 7x(2//2). a) RHEED image at the end of a nickelate layer. b) RHEED image at the end of a cuprate layer. c) The corresponding diffraction pattern shows impurity phases (blue arrows) and the *c* axis parameter of the hybrid structure determined from an analysis according to Nelson-Riley is 23.1 ± 0.4 Å.

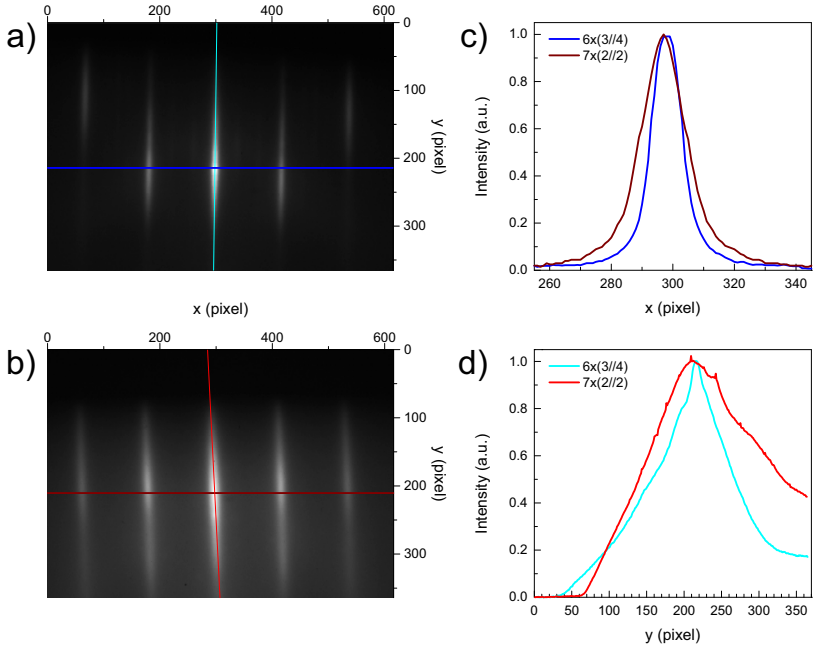

Figure 5.6: Comparison of RHEED profiles. a) RHEED image of 6x(3//4) at the end of the growth shows sharp rods. The blue and cyan line indicate the directions of the line plots shown in c) and d). b) RHEED image of 7x(2//2) at the end of the growth shows broad rods. The dark red and red line indicate the directions of the line plots shown in c) and d). c) Line plot perpendicular to the central (00) rod as indicated in a) and b). d) Line plot parallel to the central (00) rod as indicated in a) and b).

remains the same. This effect makes it difficult to control the amount of deposited material accurately and particularly effects the growth of samples with only few atomic layers of cuprate or nickelate and there is a tendency to deposit more material than intended.

5.2 Structural characterization

After optimizing sample growth, their structural characterization is the basis for all further measurements. When combining information obtained from XRD and TEM,

one gains a profound knowledge of the well ordered parts, the defects in a sample and their density.

The well ordered parts of a sample contribute to sharp peaks in the diffraction pattern and the lattice parameters and the strain state can be determined. As will be shown below, it is rather cumbersome to determine the layering of novel heterostructures through XRD only since XRD gives direct access to the average periodicity of the layered structure but not to the individual stacking of the layers. In such a case, direct space, local imaging by TEM reveals information about the layer stacking and, in addition, about stacking faults.

Defects and impurities in the structure lead to a broadening and intensity loss of diffraction peaks or to additional peaks. However, amorphous defects are not visible in XRD. And an outgrowth of a crystalline impurity phase leads to additional peaks but its composition is basically impossible to guess by XRD alone. Again, TEM can deliver the microscopic details of a defect and give important hints on how to improve the growth.

In the following, we will combine XRD and TEM in order to attain an in-depth knowledge of the structural properties which are the basis to understand the physical properties discussed afterwards.

5.2.1 X-ray diffraction

The structure of the samples was probed by off-resonant XRD. Every sample was measured in-house with a four-circle diffractometer equipped with a Cu K_α source. Two samples were investigated at the MPI-MF Surface Diffraction beamline of the ANKA light source of the Karlsruher Institute of Technology in Germany, using a photon energy of 10 keV which is equivalent to a wavelength of 1.2398 Å. Both instruments were equipped with a 2-dimensional MYTHEN detector enabling the fast measurement of reciprocal space maps (RSM). [35]

The two samples, which are discussed in the following, are grown on LSAT and have the following structures:

- $[(La_2CuO_4)_3LaO(LaNiO_3)_4]_6$, i.e., 6x(3//4)
- $[(La_2CuO_4)_2LaO(LaNiO_3)_4]_{10}$, i.e., 10x(2//4).

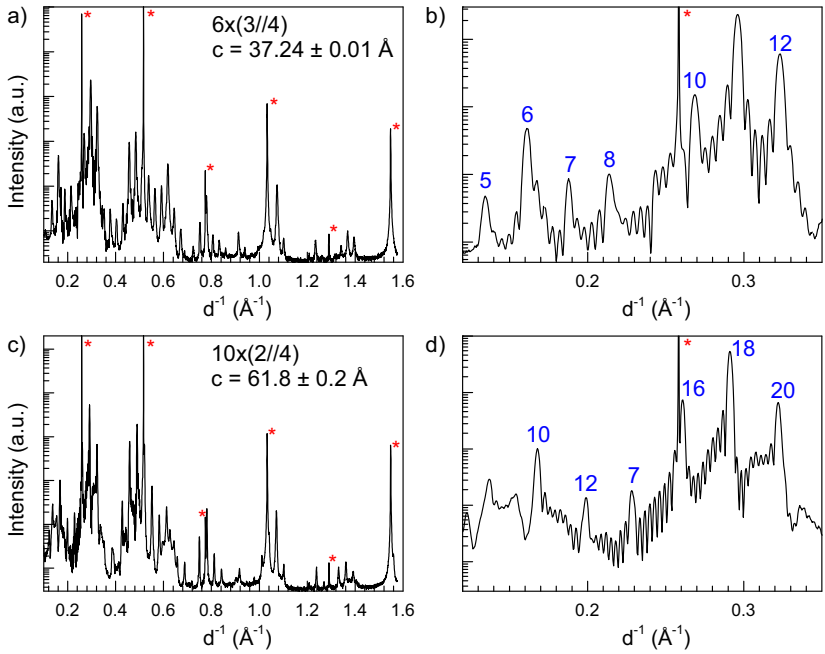

Figure 5.7: XRD scans along the $(00l)_{pc}$ direction of two samples – $[(La_2CuO_4)_3LaO(LaNiO_3)_4]_6$ (a & b) and $[(La_2CuO_4)_2LaO(LaNiO_3)_4]_{10}$ (c & d) – grown on LSAT. The first sample is the same sample for which the RHEED oscillations and images are shown in Figure 5.3. Substrate peaks are indicated by red asterisks. The blue numbers indicate the l values of the hybrid structures. The data were taken using photons with an energy of 10 keV, i.e., λ = 1.2398 Å at the ANKA synchrotron of the KIT in Germany. a) Overview scan of $[(La_2CuO_4)_3LaO(LaNiO_3)_4]_6$. b) Close-up around the (001) substrate peak. c) Overview scan of $[(La_2CuO_4)_2LaO(LaNiO_3)_4]_{10}$ d) Close-up around the (001) substrate peak.

Figure 5.2 shows how one unit cell of $La_5Ni_4O_{13}$ and two unit cells of La_2CuO_4 add up to form one unit cell of $[(La_2CuO_4)_2LaO(LaNiO_3)_4]$.

A scan along the $(00l)_{pc}$ direction (Figure 5.7a&b) of the 6x(3//4) sample shows Bragg peaks of the hybrid structure up to high l values which indicates a single phase of high structural quality. Moreover, Laue fringes are visible (Figure 5.7b) which are a proof that the interfaces are smooth and that six repetitions of the unit cell were deposited as intended.

An analysis of the Bragg reflections according to Nelson-Riley (see Chapter 3.1.1) results in a c axis of 37.24 ± 0.01 Å which is very close to the value one would expect if one simply adds the c axes of $La_5Ni_4O_{13}$, i.e., 5413-LNO, and La_2CuO_4 grown on LSAT:

$$\tfrac{1}{2}\, c_{5413-LNO} + \tfrac{3}{2}\, c_{LCO} = \tfrac{1}{2} \cdot 35.71\,\text{Å} + \tfrac{3}{2} \cdot 13.05\,\text{Å} = 37.43\,\text{Å}$$

The second 10x(2//4) sample shown in Figure 5.7c&d, is not as well ordered as the first one. It does show impurity phases, for example, there is some additional intensity at $d^{-1} \approx 0.3\,\text{Å}^{-1}$ and the Laue fringes are not clearly distinguishable below $d^{-1} \approx 0.16\,\text{Å}^{-1}$. Nonetheless, film peaks are also visible up to high l values.

An analysis of the Bragg reflections according to Nelson-Riley (see Chapter 3.1.1) results in a c axis of 61.8 ± 0.2 Å (note that the error is an order of magnitude higher as for the first sample) which is, within the error bar, the value one would expect if one simply adds the c axes of 5413-LNO, and La_2CuO_4 grown on LSAT:

$$c_{5413-LNO} + 2 \cdot c_{LCO} = 35.71\,\text{Å} + 2 \cdot 13.05\,\text{Å} = 61.81\,\text{Å}$$

The data to calculate the expected c parameters were taken from the NR analysis of the specular Bragg reflections of $La_5Ni_4O_{13}$ grown on LSAT (Figure 5.8).

In order to determine the strain state of the samples, reciprocal space maps (RSM)

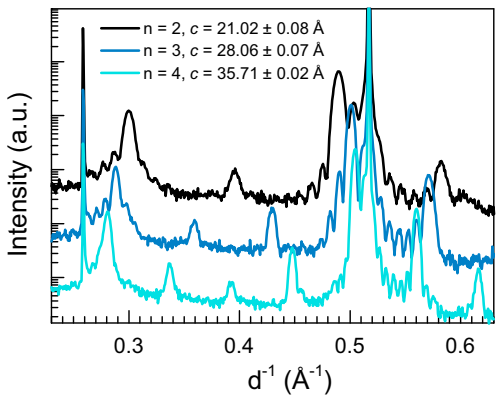

Figure 5.8: Specular crystal truncation rods of the RP phases, $La_{n+1}Ni_nO_{3n+1}$, with n = 2, 3 and 4. The c axis parameters, which were obtained from a NR analysis are shown in the legend. The data were taken with a Cu $K_{\alpha 1}$ source.

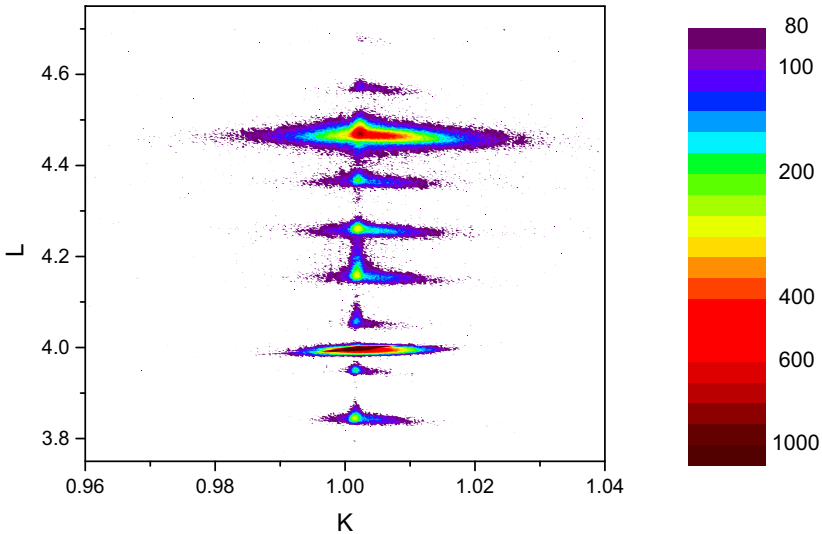

Figure 5.9: Reciprocal space map around the $(104)_{pc}$ substrate peak with 6x(3//4) grown on top taken at ANKA. The intensity is given in counts per second and the x- and y-direction are given in units of the reciprocal lattice of the substrate. The film peaks show a small shift towards higher K values which implies a partial relaxation of the tensile strain. The in-plane lattice parameters are $a = b \approx 3.85$ Å.

around the $(10l)_{pc}$ reflections were taken. We used an in-house diffractometer for standard feedback measurements. However, the small strain relaxation could only be observed in data taken at the ANKA synchrotron (Figure 5.9). The center of the in-plane peak is determined as K ~1.004, resulting (according to the calculation presented in Chapter 4.2) in an in-plane lattice parameter for 6x(3//4) of 3.85 Å.

5.2.2 STEM

The microstructure of three samples was investigated by Scanning transmission electron microscopy (STEM) at the Stuttgart Center for Electron Microscopy at Max Planck Institute for Solid State Research. The data collection and analyses were performed by Dr. Yi Wang and the STEM specimen were prepared by U. Salzberger. STEM specimens were prepared by a standard procedure which included mechanical

grinding, tripod polishing, and argon ion beam milling in a stage cooled with liquid nitrogen. Before STEM experiments, samples were plasma-cleaned by a Fischione plasma cleaner in a 75% argon – 25% oxygen mixture for 4 min to eliminate hydrocarbon surface contamination. STEM investigations were performed using a JEOL JEM-ARM 200CF scanning transmission electron microscope equipped with a cold field emission electron source, a DCOR probe corrector (CEOS GmbH), a 100 mm^2 JEOL Centurio EDX detector, and a Gatan GIF Quantum ERS electron energy-loss spectrometer (EELS). The microscope was operated at 200 kV, a semiconvergence angle of 20.4 mrad, giving rise to a probe size of 0.8 Å. 75 – 309 mrad and 11 – 24 mrad collection angles were used to obtain the high-angle annular dark field (HAADF) and annular bright field (ABF) images, respectively. A collection semi-angle of 111.5 mrad was used for EELS elemental mapping. For lattice and oxygen octahedra distortion quantification, in order to improve the signal-to-noise ratio (SNR) and to minimize the image distortion of HAADF and ABF images, 7 frames were acquired with a short dwell time (2 μs per pixel). The frame series was aligned by a Gatan image alignment plug-in in Digital Micrograph. The diagnosis of the sample drift between the frames was performed on the HAADF and the removal of the drift parameters were applied to both HAADF and ABF images. The aligned frames were then superimposed. The image analysis was performed by Oxygen Octahedra picker software. [106]

The investigated samples were deposited on LSAT with the following layer sequences:

- $[(LaNiO_3)_4(La_2CuO_4)_2]_{10}$, i.e. 10x(4//2); note that in this particular case, $LaNiO_3$ was deposited as the first layer and no additional lanthanum oxide layer was inserted between nickelate and cuprate layers.
- $[(La_2CuO_4)_2LaO(LaNiO_3)_3]_{10}$, i.e., 10x(2//3)
- $[(La_2CuO_4)_3LaO(LaNiO_3)_4]_6$, i.e., 6x(3//4)

The approach regarding the TEM measurements is the following: First, we will focus on the overall-structure, the evolution of sample quality and the nature of the defects. Based on that, we will make a connection between sample growth and the resulting quality. Later, we will discuss structural details, i.e., the position of oxygen atoms in the lattice.

ADF images and EELS

At this place it is first necessary to explain what will be referred to as *coherently* and *incoherently* grown areas. For STEM, very thin slices are cut out of the sample. When measuring in transmission through these slices, several atomic columns behind each other are mapped and one sees a projection of these columns on top of each other. If the columns in the front and in the back have grown in the same fashion and the layers are not shifted with respect to each other, i.e., the columns have grown *coherently*, the image directly depicts the crystal structure. If, however, the layers are somehow shifted with respect to each other, i.e., the columns have grown *incoherently*, the image shows a projection of different structures behind each other and hence appears to be blurry. These *incoherent* areas can, for instance, appear if a layer is not completed during growth before the next layer is started. Alternatively, a step in the substrate

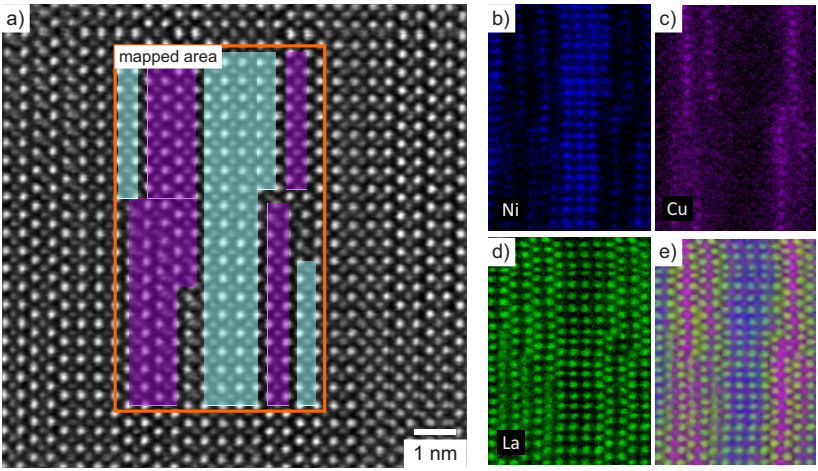

Figure 5.10: HAADF-STEM image and EELS mapping of 10x(4//2). a) HAADF image. The orange box marks the area that was mapped with EELS. The blue- and purple-shaded rectangles mark the areas that grew coherently in the perovskite (113) or K_2NiF_4 (214) structure type, respectively. b-d) Atomic column resolved nickel $L_{2,3}$-edges, copper $L_{2,3}$-edges and lanthanum $M_{4,5}$-edges elemental maps. e) Overlay of the three maps with nickel (blue), copper (purple) and lanthanum (green).

surface can also shift columns grown on top with respect to each other.

The very first sample of the series of lanthanum nickelate – lanthanum cuprate hybrid structures was grown by repeating 10 times a sequence of 4 layers of $LaNiO_3$ and 2 layers of La_2CuO_4. During growth, we noticed that the RHEED pattern did not follow the usual oscillations but it followed a regular pattern and hence there was no adjustments to the shutter opening times.

In hindsight, the unusual pattern was probably due to a dynamical layer rearrangement during growth. Through a STEM analyis coupled with EELS (Figure 5.10), we realized that the cuprate layers were always separated by two lanthanum oxide layers from each other and from the nickelate layers. In Figure 5.10 it can be seen clearly that areas that grew coherently in the perovskite structure (blue-shaded rectangles) contain only nickel whereas the the areas that grew coherently in the K_2NiF_4 structure type (purple-shaded rectangles) contain mostly copper.

In another experiment, we tried to replace some of the nickel in $LaNiO_3$ with copper. The RHEED intensity decreased immediately and the reflected, diffracted spots and the truncation rods became very broad.

Hence, we can conclude that copper does not form bonds where it is connected to the next *B* site cation via one oxygen atom under MBE conditions meaning that it does not form octahedra that are connected via their corners in growth direction.

After realizing that one cannot force the system to form these bonds, we started to grow these heterostructures directly in the way they grew naturally. The result can be seen in Figure 5.11. Again, the coherently grown areas are shaded in blue (perovskite structure type) or purple (K_2NiF_4 structure type), respectively.

The first image (Figure 5.11a) shows the first sample, 10x(4//2), (a larger area than in Figure 5.10). Here, we can see that significant parts of the sample did not grow coherently. And those parts that do show a coherent structure vary a lot with respect to their thickness.

The second image (10x(2//3), Figure 5.11b) shows only few incoherently grown parts. And also the thicknesses of the layers are mostly as intended either two consecutive lanthanum cuprate or three consecutive lanthanum nickelate layers. There are, however, some additional layers inserted into the structure.

The last image (6x(3//4), Figure 5.11c) is free from non-coherent parts and also

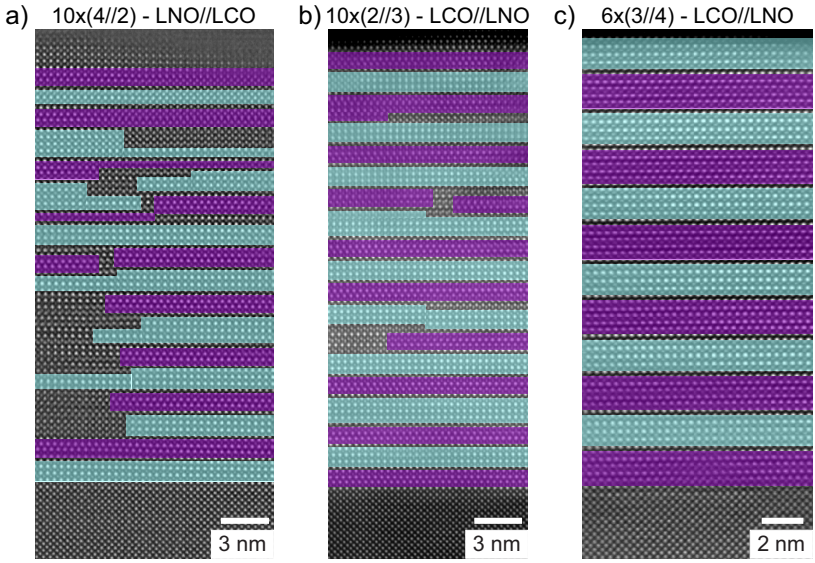

Figure 5.11: HAADF-STEM images of three different samples. The blue- and purple-shaded rectangles mark the areas that grew coherently in the perovskite (113) or K_2NiF_4 (214) structure type, respectively. a) 10x(4//2). b) 10x(2//3). c) 6x(3//4).

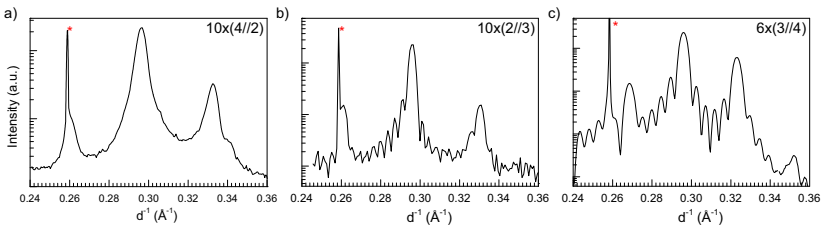

Figure 5.12: XRD scans close to the $(001)_{pc}$ substrate peak (marked with a red asterisk) confirm the improvement of sample quality seen in STEM images (Figure 5.11).

free from additional or missing layers at least in the small mapped representative area. This interpretation is further supported by XRD measurements which also show the same improvement in sample quality.

Despite the improvement in sample quality, there are still defects. Figure 5.13

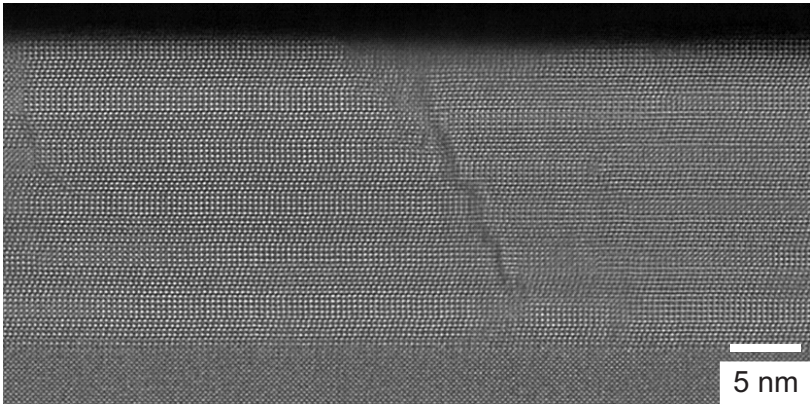

Figure 5.13: TEM of 6x(3//4). The image shows a big crack close to the middle of the image, starting above the first unit cell. And a small crack on the left side of the image, starting in the middle of the sample. Besides, there are large defect-free areas.

shows a large overview image of the sample with the highest quality, 6x(3//4). Two cracks are visible – a big one close to the center of the image which starts above the first unit cell and extends to the surface of the sample and a smaller one at the left side of the image which starts in the middle of the sample. The latter one doesn't seem to extend to the surface. Next to the two cracks, there are (small) areas that did not grow coherently.

It is likely that the occurrences of the two different type of defects are connected. An off-stoichiometry could create shifts in the structure which then exert some extra strain on the sample which in turn leads to the formation of a crack. On the other side, we cannot fully exclude that the observed cracks stem from the TEM sample preparation.

The large defect-free areas enabled us to conduct a more detailed analysis, namely to study the intermixing at the interface by EELS and a measurement of the oxygen–oxygen distances by ABF imaging.

Figure 5.14 shows elemental maps of lanthanum, copper and nickel (b-e) in such a defect-free area. Although one can clearly distinguish the nickelate and cuprate layers, it is also obvious that there is an intermixing at the interface. The line plot in

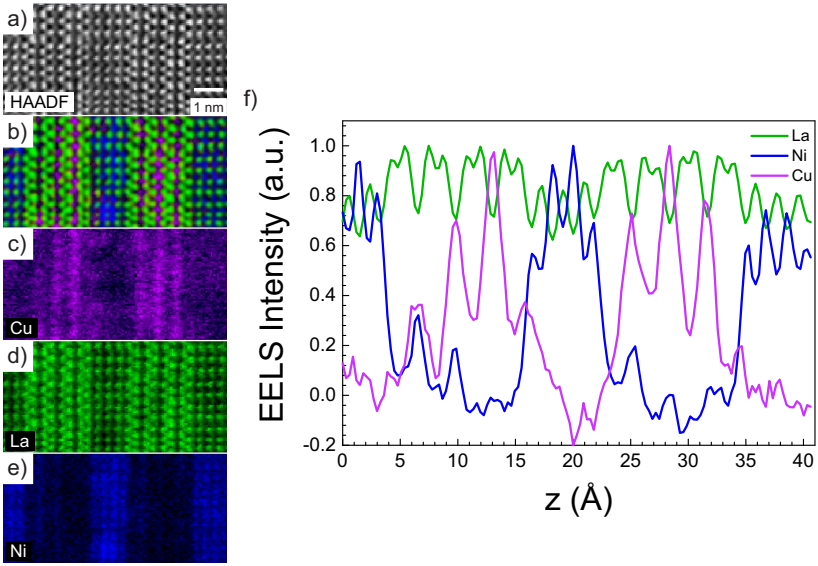

Figure 5.14: EELS mapping of a defect-free area of 6x(3//4). a) HAADF image. b) Overlay of the three following elemental maps with nickel (blue), copper (purple) and lanthanum (green). c-e) Atomic column resolved copper $L_{2,3}$-edges, nickel $L_{2,3}$-edges and lanthanum $M_{4,5}$-edges elemental maps. f) Averaged line profiles from the EELS spectrum imaging along the out-of-plane direction.

Figure 5.14f visualizes the amount of intermixing. For entropic reasons, it is impossible to eliminate this intermixing completely. A lower growth temperature would probably reduce the exchange of atoms across the interface since the role of diffusion will be reduced but would also lead to island growth because of the low mobility of the adatoms which, in turn, increases the interface roughness again and also reduces the structural in-plane coherence length.

Local lattice distortions: O–O & La–La distances

The physical properties of a transition metal oxide are strongly connected to the length of the metal-oxygen bonds and sensitive to small local distortions of the lattice. Standard STEM technique is usually most sensitive to heavy atoms and least sensitive

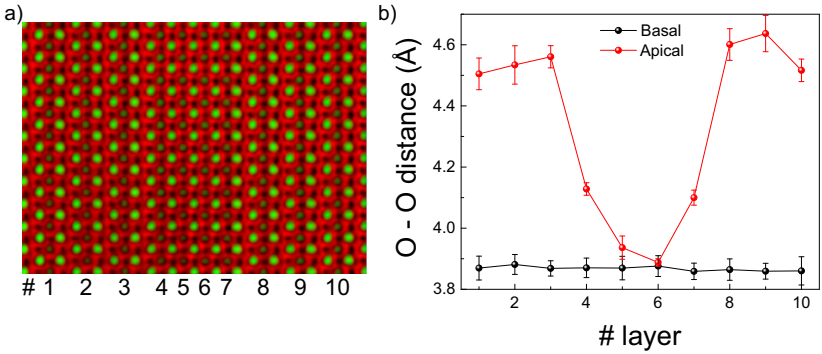

Figure 5.15: a) Superimposed ABF (red) and HAADF (green) images of 6x(3//4). Lanthanum atoms appear bright green, copper and nickel atoms dark green and oxygen atoms black. The copper and nickel layers are numbered from 1 to 10. Layers 1 –3 and 8–10 are copper layers and layer 4–7 are nickel layers. b) Basal (black) and apical (red) oxygen-oxygen distances for the layers 1 to 10.

to light atoms like oxygen. With modern techniques, however, it is possible to even determine the position of oxygen atoms in a structure. Since defects distort the structure and their impact can extend over a certain length, it is necessary to find a defect free area to do a proper analysis of oxygen positions. Alongside, we also trace the lanthanum-lanthanum distances.

Figure 5.15a shows an overlay of ABF and HAADF images of such a defect free area. Oxygen atoms are clearly visible and the distances between them could be measured (Figure 5.15b). The dependence of oxygen-oxygen distances on their position along the growth direction shall be discussed here.

The first thing to notice is that the basal distances remain unchanged across the layer within the error bar which was expected because of the strain exerted by the substrate. The small relaxation of the in-plane lattice parameter measured with x-ray diffraction ($a = b = 3.85$ Å) lies within the error of the measurement. Moreover, the copper-oxygen octahedra are much longer (average apical O–O distance = 4.56 ± 0.05 Å) than the nickel-oxygen octahedra (average apical O–O distance of the inner nickel-oxygen octahedra = 3.91 Å and average apical O–O distance of the interfacial nickel-oxygen octahedra = 4.11 Å).

This is not surprising because copper in an octahedral ligand field is with its $3d^9$ electronic configuration Jahn-Teller active and the octahedron is therefore elongated. In bulk La_2CuO_4 and $La_{2-x}Sr_xCuO_4$ the apical oxygen-oxygen distances are even bigger than the ones obtained for our hybrid structures. Here are selected values for comparison:

- bulk LCO: c = 13.14 Å, apical O–O distance = 4.84 Å [107]
- bulk $La_{1.87}Sr_{0.13}CuO_4$: c = 13.18 Å, apical O–O distance = 4.81 Å [108]
- thin film LCO on LSAT: c = 13.05 Å (data obtained in the course of this work); the apical O–O distance is not known

Compared to the above-mentioned values, the copper-oxygen octahedra are compressed. The magnitude of this effect (~4%) cannot be explained by strain alone. If the LCO unit cell would conserve its volume when going from bulk to epitaxially strained thin film on LSAT, the c axis should be 12.70 Å. By scaling the apical O–O distance based on this value, one would expect the apical O–O distance to be 4.64 Å. If one scales to the measured LCO thin film c-axis, one would expect an octahedron size of ~4.76 Å. The measured apical O–O distances are smaller than both values.

An effect acting in addition to the epitaxial strain could be a charge transfer from copper to nickel which drives the copper towards a higher oxidation state. Higher charged ions are smaller than their less charged counterparts and the bond distances shorter. Furthermore, a charge transfer would imply the formation of trivalent copper which does not exhibit a Jahn-Teller effect. In addition, a diffusion of nickel into the cuprate layers can also lead to a reduced octahedron size.

The nickel octahedra are also elongated, although not as much as the copper octahedra and there is a significant difference between inner and outer (interfacial) nickelate layers. The inner layers are in a similar environment as in bulk $LaNiO_3$ and in an unstrained sample, one would expect equal basal and apical oxygen-oxygen-distances. In an LNO film grown on LSAT, the tensile strain leads to a small compression of the octahedron. Interestingly, it is the opposite in the hybrid structure.

The outer layers are on one side in an environment as in bulk $LaNiO_3$ and on the other side as in bulk La_2NiO_4. Consequently, the octahedron is slightly elongated

which one could also relate to the fact that nickel nominally has a charge of +2.5 which makes the ion bigger than in Ni^{3+}.

Since the inner and outer nickel layers share an oxygen atom, it seems likely that the additional electrons stemming from the extra lanthanum layer at the interface are shared to some extent between inner and outer layers, thereby explaining the slightly enlarged apical O–O distances within the inner nickelate layers.

A question that cannot be answered here is the occurrence of oxygen interstitials or vacancies. They can easily form during growth, it is extremely hard to determine their amount and they would impact unit cell and octahedron size independently – causing, for example, an elongation of the unit cell and a compression of the copper octahedron at the same time due to oxygen interstitials.

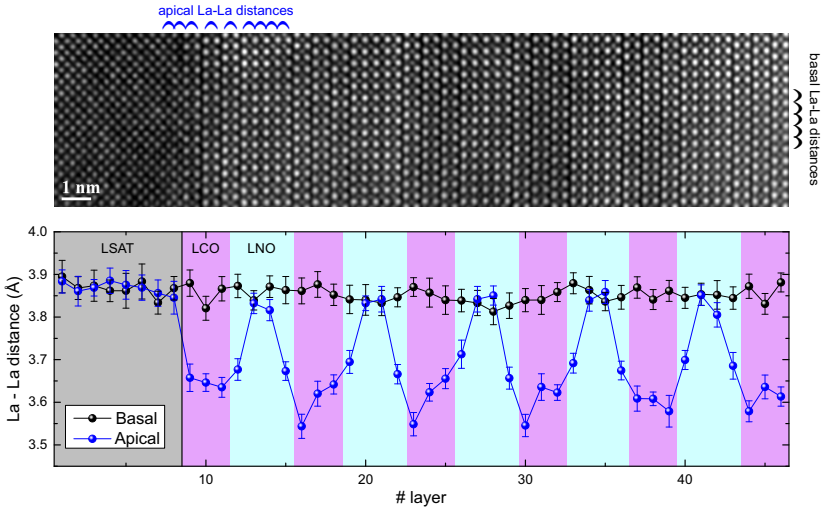

Figure 5.16: La–La distances along the in-plane (basal, black) and out-of-plane (apical, blue) direction together with the corresponding HAADF image. Only the distances between a pair of lanthanum atoms that surrounds the same metal-oxygen octahedron are shown. The black and blue brackets on the right side and the top clarify what is meant with “basal” and “apical” La–La distances. The gray-shaded area marks the substrate, LSAT, and the purple- and blue-shaded areas mark cuprate and nickelate layers, respectively. The modulation of La–La distances is opposite to the modulation of the oxygen-oxygen distances (Figure 5.15) but the changes are much smaller than in the case of oxygen.

Compared to the O–O distances, the apical La–La distances change less along the layers (Figure 5.16). However, they behave exactly opposite to the O–O distances, namely they are smaller in the cuprate layers and larger in the nickelate layers. For the inner nickelate layers, they are the same as the basal distances and for the interfacial layers, they are adopt an intermediate value. The basal distances do not change across the sample indicating that the amount of strain relaxation is smaller than the error bar.

The overall lattice constant as determined from these images is 37.55 ± 0.03 Å which deviates slightly from the value obtained from XRD (37.24 ± 0.01 Å). This small difference can be explained with the different probing volumes of the two techniques. While XRD probes a large sample volume and therefore delivers good statistics but also averages over defects, TEM measures only a small volume. An inhomogeneity of the sample or the averaging over defects could lead to the observed deviation.

5.3 Physical properties

After setting the basis with an in-depth structural characterization, we can now turn towards the physical properties. In particular, we aim to find out whether the nickelate and cuprate layers act as separate units or whether they interact with each other, e.g., via charge transfer from one to the other layer or magnetic exchange interactions. Therefore, we probed the orbital distribution of electrons by x-ray absorption (XAS) and x-ray linear dichroism (XLD) and the ordering of magnetic moments by x-ray magnetic circular dichroism (XMCD) and SQUID measurements. Moreover, we relate these results to electrical transport.

5.3.1 X-ray absorption and linear dichroism

From XAS, which probes the site and symmetry projected empty density of states, one can draw conclusions on the occupied density of states. Using polarized light, it is possible to distinguish between orbitals that point into the different crystallographic directions. All this information is essential to understand the macroscopic behavior of materials, namely electrical transport and magnetism.

Therefore, we investigated the XAS and XLD spectra of two different samples, both grown on LSAT:

- $[(La_2CuO_4)_3LaO(LaNiO_3)_4]_6$, i.e., 6x(3//4)
- $[(La_2CuO_4)_2LaO(LaNiO_3)_4]_{10}$, i.e., 10x(2//4)

And we discuss their copper and nickel $L_{2,3}$-edges in comparison with those of La_2CuO_4 and $LaNiO_3$ thin films, respectively.

As discussed earlier, the growth conditions greatly influence the amount of oxygen in the sample and consequently the oxidation state of the transition metals which, in turn, can be seen in the absorption spectra. It is useful to keep in mind that the two hybrid structures were grown under similar conditions, i.e., ~600°C and ~$3\cdot10^{-5}$ mbar ozone pressure. And the thin films were grown under optimal conditions for the respective material, i.e., ~640°C and ~$3\cdot10^{-5}$ mbar for La_2CuO_4 and ~550°C and ~$3\cdot10^{-5}$ mbar for $LaNiO_3$. All samples were cooled at growth pressure in ozone atmosphere.

Before discussing the actual sample spectra, it is necessary to review typical spectra of cuprates and nickelates that were reported in literature. First, we will review the unpolarized [109–114] and polarized [115–117] spectra of different copper compounds, thereby focusing on La_2CuO_4 and its derivatives. Afterwards, we will turn towards unpolarized [67–69, 118, 119] and polarized [16, 17, 77] spectra of nickel compounds without going into too great details since an extensive discussion can be found in Chapter 4.3 and 4.4.

Literature review of XAS and XLD at the Cu $L_{2,3}$-edges

At the Cu $L_{2,3}$-edges $2p$-electrons are excited into unoccupied states close to the Fermi energy and therefore they are very sensitive to the electronic structure of the cuprates. Unpolarized spectra are useful to evaluate the oxidation state and polarized spectra examine the distribution of holes among the different e_g orbitals. The t_{2g} orbitals are low in energy, fully occupied and consequently do not play a role in x-ray absorption. A summary of measured XAS spectra at the Cu L_3-edge is shown in Figure 5.17 and a summary of initial and final states as well as of the corresponding transitions together with their respective energies is presented in Table 5.1.

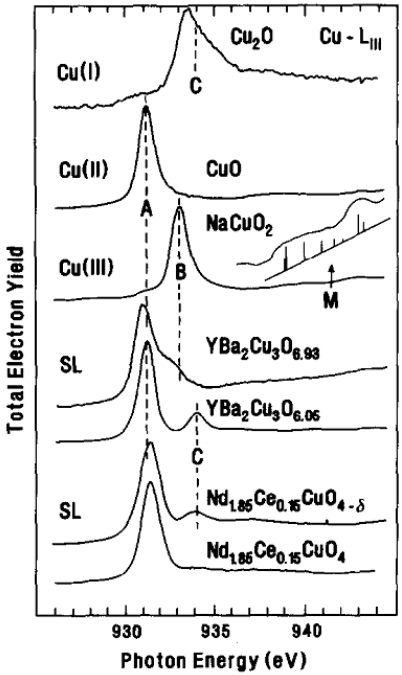

Figure 5.17: XAS spectra at the Cu L_3-edge of different HTSCs together with mono-, di- and trivalent reference compounds reprinted from Ref. [120], with permission from Elsevier. The letters A, B and C indicate peaks corresponding to di-, tri- or monovalent copper. M indicates the multiplet expected for a $2p^6 3d^8 \rightarrow 2p^5 3d^9$ transition.

In a purely ionic picture, *mono-, di- and trivalent* copper would have an [Ar]$3d^{10}$, [Ar]$3d^9$ or [Ar]$3d^8$ ground state configuration, respectively. As we will see in the following, this picture does not describe the electronic structure well. With its relatively high electronegativity and strong electronic correlations, copper bonds exhibit a strong covalent character, there is a mixture of different ground states and the filling of the copper d orbitals does not agree with the filling assuming an ionic picture. Nonetheless, it is helpful to use this terminology and below, we will discuss what these terms imply for the actual electronic structure close to the Fermi level and the consequences for the XAS spectra. Since most of the available literature covers only the L_3-edge

	Cu(I)	**Cu(II)**	**Cu(III)**
initial states	$\mathbf{3d^{10}}$, $3d^9 4s^1$, $3d^{10}4s^1\underline{L}$	$\mathbf{3d^9}$, $3d^{10}\underline{L}$	$3d^8$, $\mathbf{3d^9\underline{L}}$, $3d^{10}\underline{L}^2$
final states	$2p^5 3d^{10}4s^1$	$\mathbf{2p^5 3d^{10}}$, $3d^{10}4s^1\underline{L}$	$2p^5 3d^9$, $\mathbf{2p^5 3d^{10}\underline{L}}$
main transition	$3d^9 4s^1 \rightarrow 2p^5 3d^{10}4s^1$	$3d^9 \rightarrow 2p^5 3d^{10}$	$3d^9\underline{L} \rightarrow 2p^5 3d^{10}\underline{L}$
white line	~934 eV	~931 eV	932-933 eV

Table 5.1: Summary of possible initial and final states of mono-, di- and trivalent copper as well as the main transition observed in XAS (and EELS) at the L_3-edge and the position of the corresponding absorption peak. The most relevant states are printed in bold. [109–113, 120, 121]

and all derived conclusions also hold true for the L_2-edge, the focus of the following discussion will be on the former.

In the ionic picture, *monovalent copper* would has an electronic configuration of [Ar]$3d^{10}$ and hence one would expect the main peak in XAS to be derived from a $3d^{10} \rightarrow 2p^5 3d^{10}4s^1$ transition. One can calculate, however, that the probability of such a transition is rather low. [122] Nonetheless, a strong excitonic line occurs at ~934 eV for Cu_2O and other monovalent cuprates. [111, 123] The reason behind is a hybridization of the Cu $3d$ states with $4s$ states and ligand holes, $\underline{L}$. In this picture, the observed peak can be assigned to a $3d^9 4s^1 \rightarrow 2p^5 3d^{10}4s^1$ transition. [121]

Divalent copper has an electronic configuration of [Ar]$3d^9$ but can also be described as [Ar]$3d^{10}\underline{L}$. Consequently, transitions into the upper Hubbard band (UHB), i.e., a $2p^5 3d^{10}$ final state, or into a $2p^5 3d^{10}4s^1\underline{L}$ final state are allowed. For the same reason as mentioned above, [122] the latter transition is very weak and is not observed. For CuO and other divalent cuprates, the L_3-edge occurs at an energy of ~931 eV. [111, 113]

For *trivalent copper*, the ionic picture predicts a $3d^8$ ground state. Due to the strong Coulomb interaction of two holes in the Cu $3d$ orbitals, this state is suppressed. There is a debate whether the corresponding $3d^8 \rightarrow 2p^5 3d^9$ transition is observable in XAS. Strebel *et al.* [120] conclude that it is not detectable while Sarma *et al.* [110] do see minute peaks corresponding to the respective transition at energies of ~941 eV and ~944 eV. There is a general agreement, however, that the strongest absorption line, which appears at an energy of 932-933 eV, can be assigned to a $3d^9\underline{L} \rightarrow 2p^5 3d^{10}\underline{L}$ transition. [109, 110, 120]

In a hole-doped, divalent copper compound a contribution of divalent and trivalent copper is expected. Since the corresponding two absorption lines lie very close to each other, one usually observes a strong peak at ~931 eV that has a more or less pronounced shoulder. The intensity of the shoulder was found to be roughly proportional to the amount of dopant or trivalent copper and the energy difference between the two peaks increases with T_c. [124]

One feature in the spectra that is still not fully understood is the spectral weight observed above ~940 eV (Figure 5.18). Sarma *et al.* [110] attributed this weight to $3d^8 \rightarrow 3d^9$ transitions. However, the lack of doping dependence rules out such an explanation. Another explanation would be $2p \rightarrow 4s$ transitions but their matrix elements are too small to explain the observed intensity. [125] An alternative is a hybridization of $3d$ states with $4s$ states which reduces the occupation of the $3d_{3z^2-r^2}$ orbital. [111] Theoretical calculations support this interpretation. [126]

The observation that this hybridization mainly affects the $3d_{3z^2-r^2}$- and not the $3d_{x^2-y^2}$-orbital leads towards the next part of this literature review, namely *linearly polarized spectra*. Sorrow investigations of divalent and hole doped cuprates have been undertaken and the ones on La_2CuO_4 and its derivatives shall be discussed here. [115–117] Figure 5.18 shows exemplary spectra of $La_{2-x}Sr_xCuO_4$. In general, one finds that the holes mainly reside in the in-plane, $d_{x^2-y^2}$-orbital, in fact, the orbital polarization is almost complete which is due to the Jahn-Teller effect.

An electron configuration with nine electrons in the d-shell is highly Jahn-Teller-active. To lift the degeneracy of the e_g-orbitals and acquire a state that is overall lower in energy, the copper-oxygen octahedra are elongated, thereby lowering the $3d_{3z^2-r^2}$-orbital with respect to the $3d_{x^2-y^2}$-orbital. For an undoped, divalent cuprate this leads to a full occupation of the $3d_{3z^2-r^2}$-orbitals and to one hole on the $3d_{x^2-y^2}$-orbitals. Deviating from this simple picture, hybridization and correlation effects can alter the orbital occupation. This simple picture, however, makes it easy to understand the high orbital polarization observed in La_2CuO_4.

As mentioned above, the spectral weight between 935 and 945 eV, whose main contribution stems from $E_h \parallel c$, is likely due to strong hybridization of the Cu $3d_{3z^2-r^2}$ states with Cu $4s$ and $4p$ states. In the analyses of Núñez Regueiro *et al.*, [117] this part of the spectra was treated as background and was not included in the sum-rule

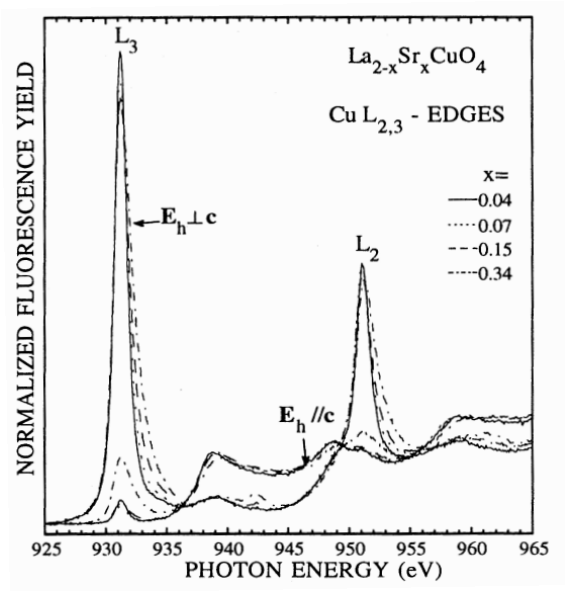

Figure 5.18: XAS spectra with the polarization of the incoming light $E_h \parallel c$ and $E_h \perp c$ at the Cu $L_{2,3}$-edges of $La_{2-x}Sr_xCuO_4$. Reprinted figure with permission from Ref. [117]. Copyright (1995) by the American Physical Society. The original data first appeared in Ref. [116].

analyses.

Upon doping La_2CuO_4 with Sr ($La_{2-x}Sr_xCuO_4$), the polarization does not change much in the beginning. Only when reaching the overdoped regime at x = 0.34 the polarization increases from ~3% to ~7% as determined via sum rules. [117, 127] At this point also the *c*-axis conductivity increases drastically, turning $La_{2-x}Sr_xCuO_4$ from a semiconductor (undoped) or two-dimensional metal (low doping, $x < 0.25$) to a three-dimensional metal. [128, 129]

There are two mechanisms that lead to a reduction of orbital polarization upon doping. First, the occurence of holes on the oxygen atoms shrinks the copper-oxygen octahedra (compare with structural data from Ref. [107] and Ref. [108]), shifts the ligand energies, and consequently alters the crystal field splitting. Moreover, an increased delocalization of electrons along the *c*-axis which stabilizes the out-of-plane

orbitals.

When phenomenologically discussing lanthanum cuprate XAS spectra the experimental findings can be summarized in the following way: a peak at 931 eV is observed for the divalent parent compound La_2CuO_4. Electron doping leads to an additional peak at 934 eV whereas hole doping leads to shoulder of the peak at 931 eV. An overview can be found in Table 5.1.

The parent compound La_2CuO_4 and the superconducting hole-doped $La_{2-x}Sr_xCuO_4$ show almost complete orbital polarization which is reduced only in the over-doped regime (x = 0.34), namely at the same point when *c*-axis electrical conductivity becomes metallic.

Literature review of XAS and XLD at the Ni $L_{2,3}$-edges

In Chapters 4.2, 4.3 and 4.4, we discussed the impact of geometric configuration and charge order on the XAS lineshape at the nickel $L_{2,3}$-edges. Here, we will focus more on the impact of the oxidation state on the spectra.

First of all, we need to remind ourselves that the lineshapes of the nickel $L_{2,3}$-edges are more complicated than in the case of copper because of multiplet-effects, i.e., the interaction of the core-hole with a valence-hole. Moreover, the ground state is a mixture of $3d^7$, $3d^8\underline{L}$ and $3d^9\underline{L}^2$. The contribution of each state to the ground state has been discussed literature based on experiments and calculations. [13, 67, 78–80] It is widely agreed that $3d^7$ and $3d^8\underline{L}$ have the highest contribution but there is a debate on which state dominates. Multiplet splitting and the different ground states are the reasons why a certain peak cannot be directly linked with a certain $2p^6 3d^n \rightarrow 2p^5 3d^{n-1}$ transition as was the case for cuprates. It requires a lot of computational power to take into account these multiplet effects and up to now, no theoretical calculations are available that accurately reproduce the observed spectra.

Nonetheless, a comparison of lineshapes of well-known compounds with those under investigation is still useful to evaluate their oxidation states. Figure 5.19 shows the absorption spectra of $NdNiO_3$, $PrNiO_3$ and NiO, reproduced from literature. [67] They depict the different lineshapes for divalent nickel (NiO) and trivalent nickel ($NdNiO_3$, $PrNiO_3$).

Here, we can see that the first peak in the absorption spectrum of NiO, labeled "a",

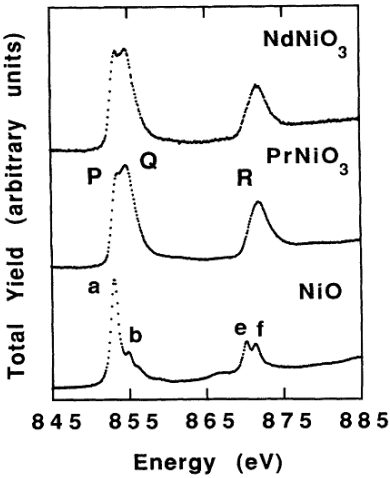

Figure 5.19: Room-temperature XAS spectra at the Ni $L_{2,3}$-edges of trivalent $NdNiO_3$ and $PrNiO_3$ together with NiO as a reference sample for a divalent Ni compound. Reprinted figure with permission from Ref. [67]. Copyright (1992) by the American Physical Society.

is much stronger than the second, labeled "b" whereas the intensities are almost equal for the two peaks, labeled "P" and "Q", at the L_3-edge of the trivalent compounds. And the L_3-edges of divalent and trivalent compounds occur at almost the same energies. Hence, the ratio of the two peak intensities gives a valuable hint towards the nickel oxidation state. Albeit this ratio should not be over-interpreted since the intensity ratio of the trivalent compounds varies somewhat with exchanging the rare earth ion, i.e. with changing the geometric configuration.

Moreover, the L_2-edge of NiO is shifted to lower energies compared to the trivalent compounds and it consists of a double-peak (features labeled "e" and "f") whereas the L_2-edges of $PrNiO_3$ (labeled "R") and $NdNiO_3$ consist of a single peak. However, the latter is ambiguous since a shoulder develops at the L_2-edges of trivalent compounds when the geometric configuration is changed, i.e., praseodymium and neodymium are exchanged for smaller rare earth ions and the shoulder could be mistaken as a sign for divalent nickel.

Therefore, evaluating the ratio of intensities at the L_3-edge is the most straightfor-

ward way to estimate the ratios of di- and trivalent nickel.

Unfortunately, the nickel L_3-edge overlaps with the very intense lanthanum M_4-edge which complicates the analysis. For the spectra shown in the course of this work, we subtracted a Lorentzian fitted the lanthanum M_4-line.

For the sake of completeness, we need to mention that transitions from $2p$-states into $4s$-states are also allowed in principle. But the probability for such a transition to occur is rather low for the same reasons as in the cuprates discussed above. And therefore these transitions can be neglected.

Unlike in the cuprates, the e_g-states in perovskite-type nickelates are degenerate. The degeneracy can be lifted with the application of epitaxial strain or two-dimensional confinement as was already discussed before (Chapters 4.2, 4.3 and 4.4).

XAS and XLD at the Cu $L_{2,3}$-edges in nickelate-cuprate hybrid structures

Figure 5.20 shows the unpolarized spectra of the two samples – 6x(3//4) and 10x(2//4) – in direct comparison with an LCO thin film. Most prominent are the two white lines at ~931 eV and ~951 eV which are ascribed to the $3d^9 \rightarrow 2p^5 3d^{10}$ transition of

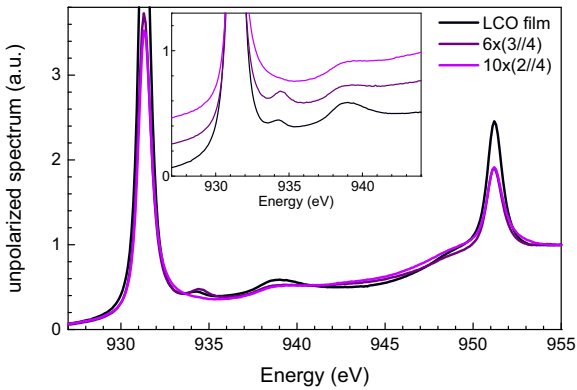

Figure 5.20: Comparison of the unpolarized, edge-normalized spectra of three different samples at the Cu $L_{2,3}$-edges: an LCO thin film (black); 6x(3//4) (dark purple); 10x(2//4) (magenta). The inset, where the data are offset by a constant value, shows a close-up of the high-energy side of the L_3-edge to emphasize that part of the spectrum that changes the most upon small changes of the copper oxidation state.

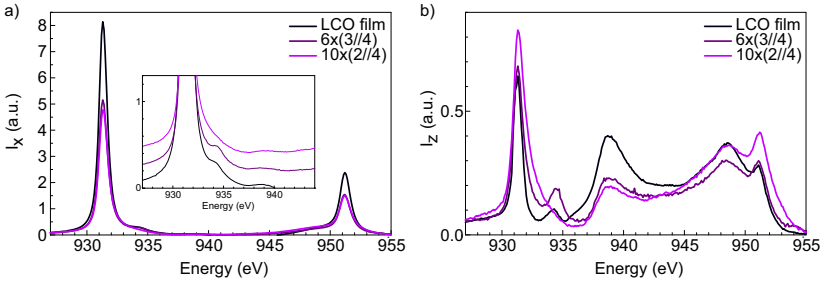

Figure 5.21: Comparison of the polarized spectra of the same three samples as above (Figure 5.20) at the Cu $L_{2,3}$-edges. a) Spectra with E ∥ x (in-plane) polarization. The inset shows a close-up of the high-energy side of the L_3-edge to emphasize that part of the spectrum that changes the most upon small changes of the copper oxidation state. b) Spectra with E ∥ z (out-of-plane) polarization.

divalent copper.

On the high-energy side of the L_3-edge, we can see some additional structure in the spectrum which is related to different oxidation states of copper (see literature review above). The inset highlights this region and for the thin film and 6x(3//4), we can see a small peak at ~934 eV which corresponds to a $3d^9 4s^1 \rightarrow 2p^5 3d^{10} 4s^1$ (or $3d^{10} \rightarrow 2p^5 3d^{10} 4s^1$ with the s states hybridizing strongly with the d states) transition and consequently to monovalent copper. This observation implies that the samples are not fully oxygenated and hence electron-doped.

Although the other sample, 10x(2//4), was grown under the same conditions as 6x(3//4), it does not show a peak at ~934 eV. Instead, the L_3-peak has a shoulder on the high-energy side which is linked to the occurrence of additional holes, i.e., trivalent copper and to a $3d^9\underline{L} \rightarrow 2p^5 3d^{10}\underline{L}$ transition. Moreover, the absorption peak is slightly shifted (931.35 eV) in comparison to 6x(3//4) and the thin film (931.33 eV).

There are several reasons that can lead to the above observation. Extrinsic factors are differing growth conditions, stacking faults and interface roughness or overall sample quality while intrinsic factors are charge transfer across the interface and an alteration of the formation energy of oxygen vacancies or interstitials.

As far as we can judge, the *growth conditions* for the two hybrid samples were exactly the same. That does not only include the growth temperature of ~600°C and a

chamber pressure of ~$3 \cdot 10^{-5}$ mbar but also the measured partial pressures of atomic oxygen (~$1 \cdot 10^{-6}$ mbar), molecular oxygen O_2 (~$2 \cdot 10^{-5}$ mbar) and ozone O_3 (~$3 \cdot 10^{-9}$ mbar). The LCO film was grown at 640°C but the chamber pressure and the partial pressures were identical with the other two samples.

Moreover, no major maintenance was undertaken before or between the growths of the samples investigated here.

The only issue that is related to the growth conditions, was an instability of the ozone still pressure and therefore also the chamber pressure at the end of the growth of sample 6x(3//4). However, even after cooling the sample to almost room temperature (80°C), the chamber pressure was still at ~2.5 mbar, i.e., not deviating significantly from the initial pressure. No issues occured during the growth of 10x(2//4) or the LCO film.

Hence it seems unlikely but cannot be fully excluded that the chamber conditions during growth were somewhat different, causing different oxidation states. The consequence would be an overall higher concentration of oxygen in the sample 10x(2//4).

Interface roughness means that there are copper atoms on nickel sites and vice versa. Such an exchange of ions has two effects on the electronic structure: For copper on a nickel site, the chemical environment (the amount of lanthanum and oxygen atoms in its vicinity) would be changed in such a way that it is pushed closer towards trivalent copper, creating holes on surrounding oxygen atoms and a shoulder on the high-energy side of the white line.

Moreover, the exchange implies that the position of the ligand oxygen ions is changed with respect to the LCO layers and that the copper orbitals can hybridize with the nickel orbitals via in-plane oxygen. This leads to a change in crystal field and the energy of the absorption peak shifts. [123, 130] Or, depending on the amount of copper on nickel sites, a shoulder develops.

Thus, the observation of the shoulder and the tiny energy shift in the sample 10x(2//4) can be understood, in the scenario of intermixing at the interface, as a sign for a contribution of trivalent copper and a shift of the absorption peak due to the altered crystal field. It is unclear how much intermixing is needed to create a shoulder or a measurable shift. One way to estimate the amount of intermixing is to grow LCO (LNO) and statistically replace copper (nickel) with nickel (copper) and determine the

energy shift depending on the nickel (copper) concentration.

Moreover, as discussed above (Chapter 5.2.1 and Figure 5.7), the XRD pattern of the sample 10x(2//4) shows imperfections which supports the interpretation of the contribution of intermixing.

For 6x(3//4), however, the situation is different. Compared to the LCO film, we do not observe any peak shift or shoulder. Therefore, we can conclude that intermixing plays at most a minor role in this sample. Apart from the growth conditions and sample quality, the only difference between the two hybrid samples is one bulk-like cuprate layer.

Another way to explain the spectra is to assume a *charge transfer* across the interface towards the nickelate layers, removing electrons from cuprate layers, introducing ligand holes and at the same time reducing the charge on nickel. Obviously, such an effect would have a bigger impact on the XAS spectra of the sample with the lower number of cuprate layers.

Yet another explanation would be that the *formation energy of oxygen vacancies* or *oxygen interstitials* is altered at the interface. A higher concentration of oxygen vacancies in bulk-like cuprate layers, or interstitial oxygen at the interface can explain our spectra at the Cu $L_{2,3}$-edges. As we will see in the discussion of the nickel spectra in the following section, sample 10x(2//4) is, overall better oxygenated which is in support of the latter scenario.

The difference of the sample spectra becomes even more visible if one compares the *polarized spectra* (Figure 5.21), in particular with E ∥ z. One could argue that the changes in orbital occupancy mainly take place in the out-of-plane orbital. However, the corresponding features in the E ∥ x spectra are masked by the intense main line at ~931 eV. One would have to deconvolute the spectra and compare the respective intensities. Different groups pursued this way of analysis but the error of the fits is quite large and the obtained values of different groups disagree. [109, 110, 113, 124, 131]

Regarding the oxidation state, we can conclude that in all the samples the main contribution stems from divalent copper and that the LCO film and 6x(3//4) show signs of monovalent copper whereas the shoulder observed for 10x(2//4) indicates additional holes, i.e., nominally trivalent copper. Responsible for the differing lineshapes at the

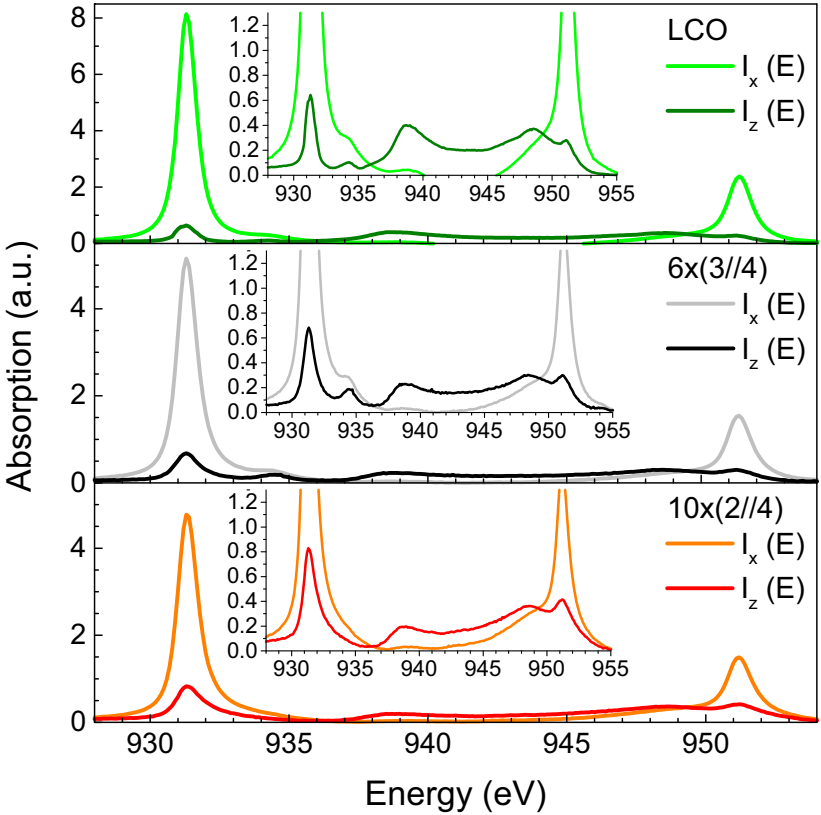

Figure 5.22: XAS spectra for E || x (in-plane) and E || z (out-of-plane) of the same three samples as above (Figure 5.20), i.e., an LCO film (top, green), 6x(3//4) (middle, black/gray) and 10x(2//4) (bottom, red/orange) at the Cu $L_{2,3}$-edges.

Cu $L_{2,3}$-edges can be a higher interface roughness of the sample 10x(2//4), charge transfer from copper to nickel, oxygen interstitials at the interface or a combination thereof.

Copper oxides are well known for their high *orbital polarization*. In the polarized spectra, Figure 5.22, we can see that all samples – LCO film, 6x(3//4) and 10x(2//4) – show a huge dichroic signal. However, the orbital polarization is clearly reduced

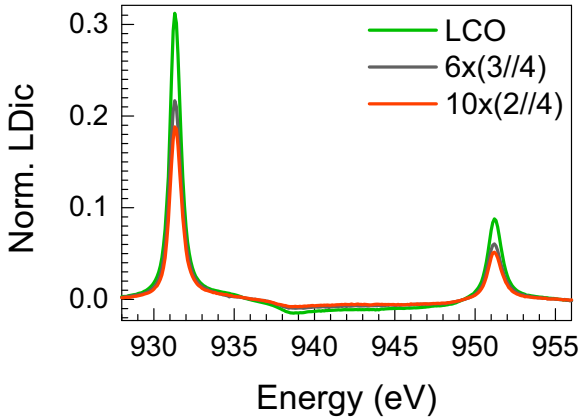

Figure 5.23: Normalized difference spectra $[I_x(E) - I_z(E)]/[(2 \cdot I_x + I_z)/3]$ at the Cu $L_{2,3}$-edges at 300 K for an LCO film (green), 6x(3//4) (gray) and 10x(2//4) (red). One can directly see that the orbital polarization in the hybrid samples is reduced with respect to the LCO film.

in the hybrid samples compared to the LCO film (see also the normalized dichroic signal, Figure 5.23). There are several possibilities that would lead to such a behavior, namely a compression of copper octahedra relative to the thin film, a delocalization of electrons along the *c*-axis or interface roughness.

As explained above, holes on oxygen would reduce the size of the copper-oxygen octahedra. In the case of the sample 6x(3//4), we do not observe an indication for ligand holes but rather the opposite (Figure 5.20). However, we know from TEM imaging (see section 5.2.2) that there is indeed a *compression of the octahedra* in direction of the *c*-axis compared to the bulk values. In principle, one should compare the O–O distances from a thin film and a hybrid sample grown on the same substrates. Unfortunately, no TEM images of LCO films are available to date.

Hence, the best approach is to compare distances measured with TEM with the ones one would expect in case of a conservation of the u. c. volume or if one uses the *c*-axis parameter obtained from XRD as a scaling factor. Note that bulk LCO has a slight orthorombic distortion. For simplicity, we use the pseudo-tetragonal (*pt*) values for our comparison:

- bulk lattice parameters: a_{pt} = 3.805 Å, c_{pt} = 13.143 Å, apical O-O distance =

4.842 Å [107]

- with conservation of u. c. volume: a_{pt} = 3.868 Å, c_{pt} = 12.705 Å → apical O-O distance = 4.679 Å
- with scaling to the measured c-parameter of an LCO film: a_{pt} = 3.868 Å, c_{pt} = 13.046 Å → apical O-O distance = 4.808 Å

The apical O–O distances determined by TEM are 4.56 ± 0.05 Å which is considerably smaller than any of the two values expected from the considerations above. The origin for this discrepancy is unclear. Theoretical calculations will be necessary to provide a deeper understanding of this phenomenon and whether the observed compression of the octahedra is big enough to explain the decrease in orbital polarization.

Furthermore, an *increased delocalization along the c-axis* – compared to the LCO film or bulk LCO – leads to a lowering of the $3d_{3z^2-r^2}$-orbital and can also contribute to the decrease in polarization. Although an undoped thin film and bulk LCO are insulating, transport data (see below, Chapter 5.3.3) at least support the view that the LCO layers in the hybrid structure are not inactive, meaning that their conductivity is comparable to that of the nickelate layers. Measurements of the c-axis conductivity will have to confirm or deny that also the c-axis resistance shows metallic behavior.

In addition to the above mentioned, intrinsic effects, *interface roughness* likely plays a role. Certainly, its role is bigger in 10x(2//4) than in 6x(3//4). As we have seen in TEM images (Chapter 5.2.2 and Figure 5.15), the apical oxygen-oxygen distances are much smaller in the nickelate layers. And as a consequence, the e_g-splitting should be reduced. Hence, if a copper ion occupies a nickel position, it is expected that the orbital polarization is reduced. Such an effect can explain the small difference between the two hybrid samples.

In summary, we found – regardless of the oxidation state – a lowering of the orbital polarization with respect to bulk or thin film LCO. The reason behind is either a compression of the copper-oxygen octahedra or an increased c-axis delocalization or a combination of both effects. To distinguish between the different possibilities, theoretical calculations and c-axis transport data are needed. The small difference between the two hybrid samples is likely due to interface roughness.

XAS and XLD at the Ni $L_{2,3}$-edges in nickelate-cuprate hybrid structures

First, we have a look at the unpolarized spectra of two samples – 6x(3//4) and 10x(2//4) – in direct comparison with an LNO thin film (Figure 5.24). The lineshapes of the $L_{2,3}$-edges are more complicated than in the case of the Cu-edges because of multiplet splitting. [37] One cannot assign an absorption peak to a certain transition and the assignment of specific lineshapes to a certain oxidation state is rather a qualitative than a quantitative approach. Cluster calculations have been made, e.g., Ref. [68], but since LNO is a metal such "local" descriptions do not fully account for all details of the spectra.

By comparing the sample spectra with reference and literature (Figure 5.19) spectra, one can draw conclusions on the oxidation states of the measured samples. For both samples, we find that the first peak labeled "a" in Figure 5.24 at the L_3-edge is higher than the second labeled "b" and the L_2-edge has a shoulder (labeled "c"). Moreover, the center of mass of the L_2-edge is shifted towards lower values compared

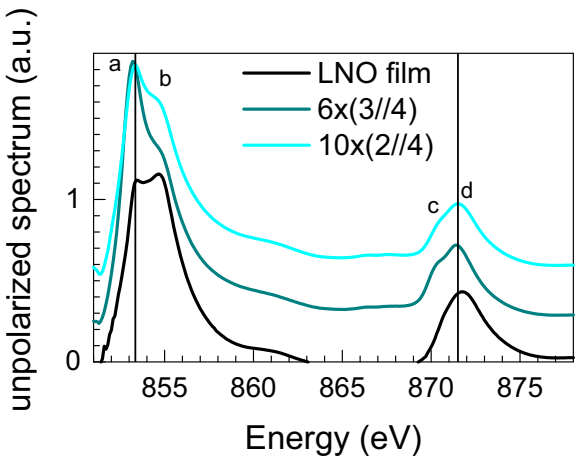

Figure 5.24: Comparison of the unpolarized spectra of three different samples at the Ni $L_{2,3}$-edges: an LNO thin film (black), 6x(3//4) (dark cyan) and 10x(2//4) (cyan) after subtraction of a Lorentzian fitted to the lanthanum M_4 line. The energy scale of all spectra was normalized to the lanthanum M_4 line. The black, vertical lines mark peak positions of the 10x(2//4) sample. The letters a, b, c and d indicate certain spectral features that are discussed in the text.

to a $LaNiO_3$ film. These features can be interpreted as a sign of divalent nickel. All of these observations are more pronounced in the sample 6x(3//4) indicating either a *charge transfer* from the cuprate to the nickelate layers or an increased *density of oxygen vacancies* or *interface roughness*.

A *charge transfer* from cuprate to nickelate layers would imply a reduced charge on nickel and increased charge on copper simultaneously which is not observed. Hence, we can exclude this scenario to be the major cause for the observed difference between the two hybrid samples. Although, a charge transfer could still take place. To measure it, one would have to compare samples of similar quality with La_2CuO_4 and the corresponding RP-phase.

A higher *concentration of oxygen* at the interface would mean a higher charge on nickel and copper simultaneously. This would have a bigger impact on the sample that has the higher number of interfaces per nickelate or cuprate layer which is what we indeed observe. There are more interfaces in 10x(2//4) than in 6x(3//4) and 10x(2//4) is the sample which appears to have a higher overall oxygen concentration.

Moreover, *interface roughness* can have a significant impact. Based on the previous conclusions, we would expect a higher impact of interface roughness on the sample 10x(2//4). One way to explain the sample spectra is to assume a nickel deficiency and a copper surplus which would bring copper atoms to the interfacial nickel sites and which would imply that more nickel ions can be found inside a layer than at the interface. It is assumed that the interfacial nickel sites have a lower positive charge than the inner nickel sites due to their chemical environment being on one side as in $LaNiO_3$ (trivalent nickel) and on the other side resembling La_2NiO_4 (divalent nickel). In this scenario, both copper and nickel would be closer to a trivalent state than in bulk LCO or in the corresponding RP-compound ($La_{n+1}Ni_nO_{3n+1}$), respectively.

To distinguish between the two scenarios (oxygen concentration or interface roughness), more sophisticated measurements are necessary, for example resonant soft x-ray reflectivity which enables a layer-selective measurement of the electronic configuration. Moreover, one would have to compare the spectra of the hybrid samples with that of the corresponding RP-phase, namely $La_5Ni_4O_{13}$.

Turning now to the *polarized spectra* (see absorption spectra in Figure 5.25 and normalized dichroism in Figure 5.26), we see that:

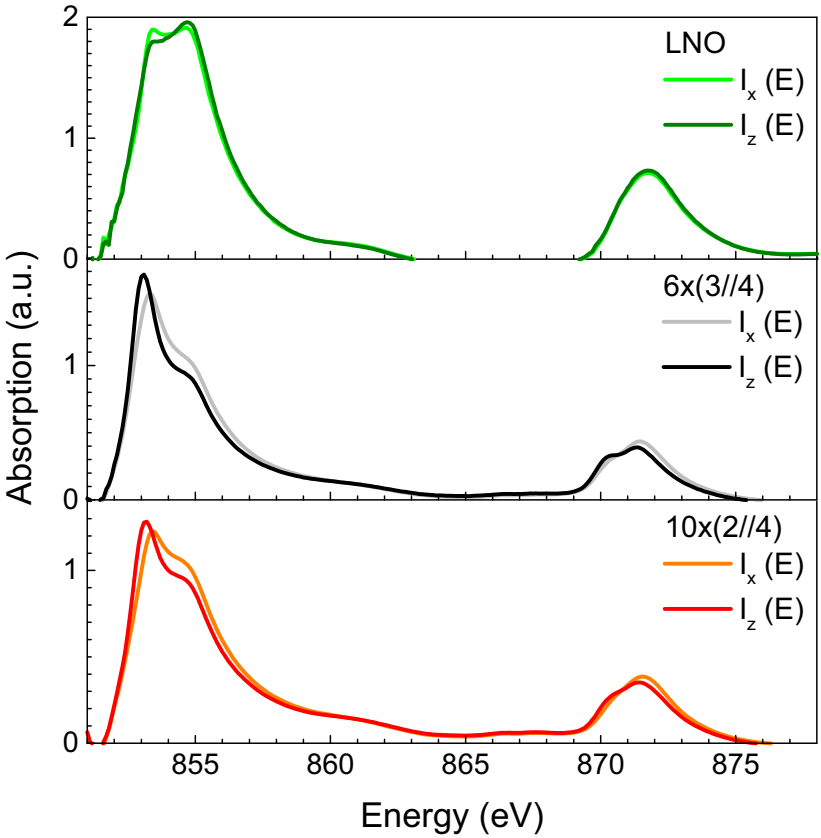

Figure 5.25: XAS spectra for E ∥ x (in-plane) and E ∥ z (out-of-plane) of the same three samples as above (Figure 5.24), i.e., an LNO film (top, green), 6x(3//4) (middle, black/gray) and 10x(2//4) (bottom, red/orange) at the Ni $L_{2,3}$-edges.

- the orbital polarization of nickel in the hybrid samples is opposite to that in the LNO film
- the orbital polarization is higher for 6x(3//4), X_{ave} = 0.94, than for 10x(2//4), X_{ave} = 0.98 (see Chapter 3.1.2)

The first observation can be explained with the elongation of nickel octahedra at the

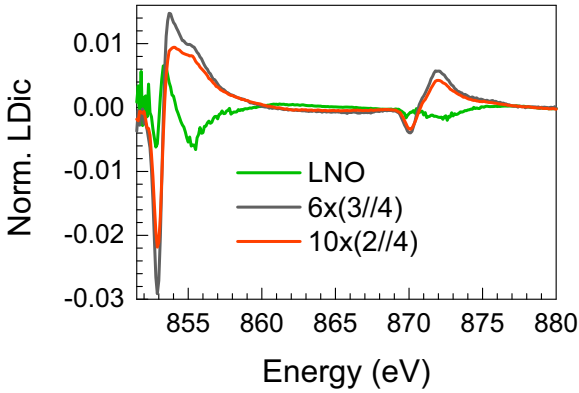

Figure 5.26: Normalized difference spectra $[I_x(E) - I_z(E)]/[(2 \cdot I_x + I_z)/3]$ at the Ni edge at 300 K for an LNO film (green), 6x(3//4) (gray) and 10x(2//4) (red). One can directly see that the orbital polarization in the hybrid sample is opposite to the LNO film.

interface observed in TEM images (Figure 5.15). An elongation of octahedra reverses the order of the e_g orbitals compared to the compressed octahedra we find for LNO grown under tensile strain.

The second observation is puzzling for the following reason: Sample 6x(3//4) has more contribution from Ni^{2+}, implying that there is a higher contribution of $3d^8$ in the ground state than for the other sample. Since the e_g splitting is always small compared to the energy needed to create an electron pair in one orbital, i.e., the pairing energy, there will be one electron per e_g-orbital. Such a $3d^8$-system will not show, in contrast do a $3d^7$-system, any orbital polarization in the ground state. Consequently, the increase of $3d$-occupation should lower the orbital polarization. Instead, the opposite is the case. Apparently, the e_g-splitting is that much enhanced in sample 6x(3//4) that the orbital polarization stemming from the remaining $3d^7$ is high enough to overcompensate the loss of polarization due to an increased amount of $3d^8$-states.

The reason behind is likely related to structural effects, i.e., changes in the size of the octahedra. To date, we only have detailed structural data for one of the two samples, namely 6x(3//4) (see Figure 5.15). Hence, considerations regarding the origin of the observed effects are speculative. Possibly, the higher interface roughness in sample 10x(2//4) reduces the crystal field splitting.

Comparison of high and low temperature XAS and XLD at the Ni and Cu $L_{2,3}$-edges in the sample 10x(2//4)

Up to now, we have only considered data taken close to room temperature (300 K). Upon lowering the temperature, the electronic structure is altered in many materials. In the present case of nickelate-cuprate hybrid structures, a magnetic transition occurs in all of the samples at ~165 K. We will discuss the origin of this transition in greater detail in the subsequent section (Chapter 5.3.2). Here, we will take the 10x(2//4)-sample as an example and investigate whether the magnetic transition also manifests itself in the absorption spectra.

Furthermore, in the series of rare earth nickelates (RENiO$_3$) a change of the XAS lineshape is observed upon crossing the metal-insulator transition (MIT). [67–69, 132, 133] Namely, the splitting between the two peaks at the L_3-edge increases and a shoulder develops at the low-energy side of the L_2-edge. A similar trend of the lineshapes is observed when reducing the nickelate layer thickness in LNO-LAO superlattices (see Chapter 4.4 and Figure 4.21). Since our hybrid structures do not undergo an MIT and the investigated sample has four consecutive nickelate layers (a thickness, where we do not observe a significant alteration of the lineshape for an LNO-LAO superlattice), we do not expect such an effect in the present case.

As we can see in Figure 5.27, where the unpolarized spectra at 300 K and 6 K at the Ni (a) Cu (b) $L_{2,3}$-edges are shown, small changes in the lineshapes do indeed occur.

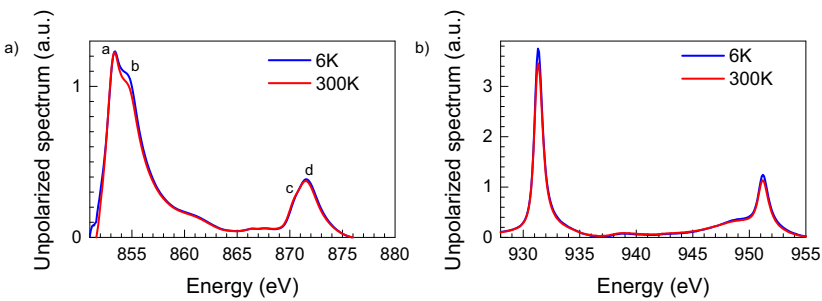

Figure 5.27: Unpolarized spectra of the 10x(2//4) sample at 6 K (blue) and 300 K (red). a) Ni $L_{2,3}$-edges. b) Cu $L_{2,3}$-edges.

On both edges, the intensity is slightly enhanced. On the nickel edge it is the feature labeled "b" in Figure 5.27a that undergoes the biggest change.

At high temperatures, one expects that more states above the Fermi energy are occupied leaving some states at lower energies empty because of thermal excitations (Boltzmann distribution). By lowering the temperature, more electrons will occupy the lower lying states. The observed small enhancement of absorption at low temperatures could therefore be related to such a shift, transferring, for example, holes from oxygen to the transition metal ions. To confirm this assumption, it would be necessary to compare with a spectrum measured at the oxygen K-edge.

More peculiar is the relatively strong enhancement of the feature labeled "b" in Figure 5.27a. A shift of the spectral weights in the unpolarized spectra can be related to magnetism. [134] At first glance, it is counter-intuitive that an ordering of magnetic moments leads to an alteration of lineshapes. However, the tiny exchange interaction in the order of 0.1 eV is indeed able to modify the lineshapes of the unpolarized spectra on top of a multiplet splitting. Since there is no multiplet splitting at the copper $L_{2,3}$-edges, no alteration of the lineshapes can be observed, even in the presence of magnetic ordering.

Magnetism also induces orbital ordering. An alignment of local atomic spins along a preferred axis leads via spin-orbit-coupling (SOC) to an additional anisotropy of the charge distribution which can be probed with x-ray magnetic linear dichroism (XMLD). [41] The magnitude of the XMLD effect depends on the angle θ between the polarization of the x-rays and the magnetic axis. Its dependence follows a $\cos^2\theta$ behavior. Hence, the effect is biggest for light polarized parallel and perpendicular to the magnetic axis.

In the case of nickel oxide, NiO, which is an antiferromagnetic insulator (T_N = 520 K), linear dichroism is observed below the Néel temperature T_N and can therefore be attributed to magnetism. [42, 134] In the present case, linear dichroism is already observed at room temperature but an additional contribution at low temperature at the nickel $L_{2,3}$-edges can possibly be related to magnetic ordering.

In Figure 5.28, we see the XAS with E ∥ x and E ∥ z at 300 K and 6 K at the Cu edge. And Figure 5.29 shows the dichroic signal in comparison with that of an LCO film. Here, we see that there are only small changes with temperature, namely the

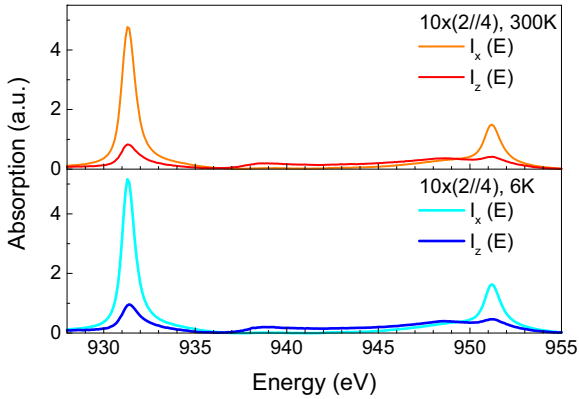

Figure 5.28: XAS spectra of the 10x(2//4) sample at the Cu $L_{2,3}$-edges with E || x (orange/ cyan) and E || z (red/ blue). The scale is arbitrary but comparable for both spectra. In the top panel are room temperature data and the data in the lower panel were taken at 6 K. There are only small changes between the two spectra.

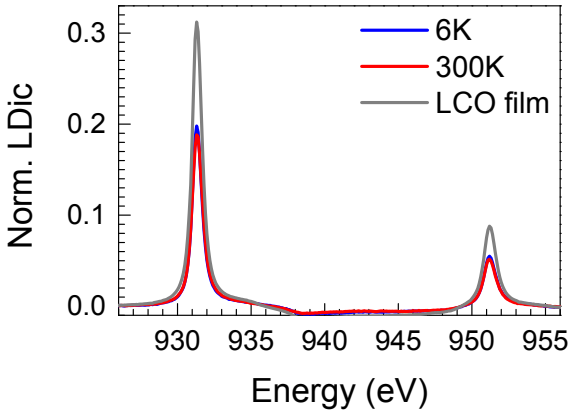

Figure 5.29: Normalized difference spectra $[I_x(E) - I_z(E)]/[(2 \cdot I_x + I_z)/3]$ at the Cu $L_{2,3}$-edges at 300 K (red) and 6 K (blue) of the 10x(2//4) sample. The magnitude of the dichroism is slightly enhanced at 6 K. For comparison the dichroic signal of an LCO film is also shown.

dichroism is slightly enhanced which is expected because of the effect of Boltzmann distribution. As mentioned above, an alteration of the spectra due to magnetism is

not expected (and also not observed) because of the lack of multiplet splitting of the copper $L_{2,3}$-edges.

Figure 5.30 shows low and high temperature data at the Ni $L_{2,3}$-edges and Figure 5.31 shows the dichroic signal in comparison with that of an LNO film. Here, we can see that there are again only small changes with temperature.

However, there is one pecularity: namely the reduction of orbital polarization at low temperatures. At first sight, it appears as though the effect could only be seen on the L_3-edge which would imply an experimental error caused, for example, through the uncertainty of the subtraction of the lanthanum line. However, if one has a closer look, i.e., by subtracting the normalized dichroic spectra from each other, one can see that the effect occurs on both edges and is therefore intrinsic. Usually, one would expect an enhancement because of Boltzmann statistics. The observation of the contrary could be an indication for magnetic correlations. To confirm or disprove such an assumption, field- and temperature-dependent studies are needed.

To sum up the temperature studies, we can say that since the copper $L_{2,3}$-edges are insensitive to the effect of magnetic correlations, we observe only small changes in

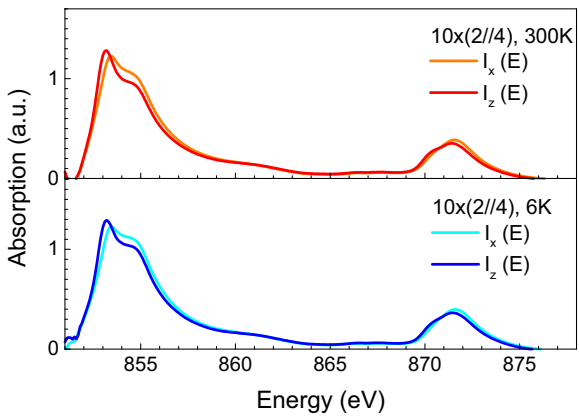

Figure 5.30: XAS spectra of the 10x(2//4) sample at the Ni $L_{2,3}$-edges with E || x (orange/ cyan) and E || z (red/ blue). In the top panel are room temperature data and the data in the lower panel were taken at 6 K. The scale is arbitrary but comparable for both spectra. The changes in the spectra are that small that they are hardly noticeable in these spectra. They are more clearly visible in the unpolarized spectra (Figure 5.27) and in the normalized dichroism (Figure 5.31).

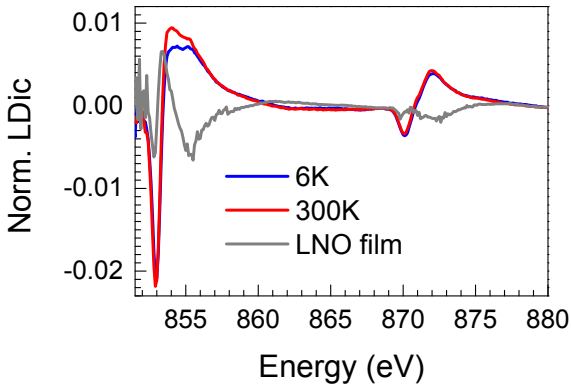

Figure 5.31: Normalized difference spectra $[I_x(E) - I_z(E)]/[(2 \cdot I_x + I_z)/3]$ at the Ni $L_{2,3}$-edges at 300 K (red) and 6 K (blue) of the 10x(2//4) sample and for an LNO film (grey). The dichroism is reduced at low temperature. For comparison, data for an LNO film are also shown.

the spectra upon cooling. The effect at the nickel $L_{2,3}$-edges is more pronounced. In particular, we find that the lineshape of the unpolarized spectrum is altered and that the dichroism is reduced upon lowering the temperature. These observations hint towards magnetic ordering but a detailed temperature-dependence would be necessary to prove this assumption.

5.3.2 Magnetism probed with SQUID and XMCD

While we investigated the distribution of electrons between the different ions and orbitals in the previous section, we turn now towards the characterization of the (magnetic) interactions between the different ions. In all samples, hybrid structures and La_2CuO_4 thin films alike, we observe a transition to a weak ferromagnetic state which probably arises due to antiferromagnetism with the moments canted along the field direction. We will first briefly discuss magnetic properties of La_2CuO_4 and its daughter compounds as well as that of $La_{n+1}Ni_nO_{3n+1}$.

Undoped LCO is antiferromagnetic (AFM) with a T_N close to room temperature. [135] Upon hole or electron doping the magnetism dies off quickly but magnetic correlations remain and are often held responsible for the occurrence of superconductivity

since this behavior is typical for all high-temperature superconductors (HTSC). [136] Moreover, LCO thin films grown on $LaSrAlO_4$ (compressive strain) and on $SrTiO_3$ have Néel transitions of 174 K and 168 K, respectively. [137]

In LCO, the magnetic moments experience strong AFM interactions within the copper-oxygen planes. A further coupling in between the planes leads to a 3D-AFM state with the magnetic moments lying in the copper-oxygen planes. [44]

The Dzyaloshinskii-Moriya (DM) interaction leads to a canting of the magnetic moments out of the copper-oxygen planes. The canted moments either point into the same direction leading to the observation of weak ferromagnetism or couple antiferromagnetically leading to no net magnetization. There is a linear dependence between the magnitude of the DM interaction and the tilting of the copper-oxygen octahedra and the spin orbit of the divalent copper ions. Moreover, the tilt pattern determines the direction of the canted moments and leads either to a net ferromagnetic moment, e.g., LCO in the low-temperature orthorhombic phase, or no moment after all, e.g., barium-doped LCO in the low-temperature tetragonal phase. In the ideal, tetragonal structure there would be no DM interaction. [138]

If the canted moments order antiferromagnetically, they will be polarized perpendicular to the copper-oxygen planes at sufficiently high fields (20 T) and cause weak ferromagnetism. [44] Furthermore the coupling of the canted spins of adjacent layers is removed upon hole doping and therefore the layers act independently.

Along the series of the RP phases, $La_{n+1}Ni_nO_{3n+1}$, the physical properties change drastically with changing n. While bulk $LaNiO_3$, $n = \infty$, remains paramagnetic and metallic in the whole temperature regime, La_2NiO_4, $n = 1$, is an antiferromagnetic insulator. And the situation is somewhat ambiguous for the phases in between. To date, only $n = 2$ and $n = 3$ have been synthesized. [105, 139–143] Fully oxidized samples are quite conductive and metallic over a wide temperature range but an anomaly of the resistivity has been found that occurs simultaneously with an increase of the magnetic susceptibility. [142, 143] Wu *et al.* [143] argue that this anomaly at 128 K ($n = 2$) or 139 K ($n = 3$) is related to the occurrence of a charge density wave (CDW) and use the simultaneous occurrence of the two features as a support for their conclusions.

An indication for weak ferromagnetism has been found for $La_3Ni_2O_{6.35}$, $n = 2$, [140] but could also be caused by nickel metal impurities. Apart from that, pre-

dominantly paramagnetic behavior has been observed and no solid evidence for a long-range magnetic ordering in the RP phases with $n = 2$ or 3 has been found so far. [140, 141, 144]

However, a spin-density wave (SDW) state has been found upon heterostructuring $LaNiO_3$, namely by making the LNO layers only two u. c. thick and separating them with two u. c. $LaAlO_3$ to form $[(LaNiO_3)_2(LaAlO_3)_2]_l$. [1, 2]

In the current section, we will investigate the magnetic behavior of samples where we brought the two compounds, La_2CuO_4 and $La_{n+1}Ni_nO_{3n+1}$, into close vicinity through heterostructuring. We will compare their magnetic properties with those of the respective bulk materials.

SQUID

In the samples studied in the course of this work, the signal measured with a SQUID magnetometer does not only stem from the hybrid structures but the substrate (LSAT) also adds a significant contribution. While paramagnetic impurities dominate the measurement at low temperatures, diamagnetism does so at high temperatures. Fortunately, it is possible to disentangle the respective contributions of a measurement of magnetization versus temperature. For all data shown in the following, a 1/T-law was fitted at low temperatures and then subtracted. Afterwards the diamagnetic contribution, which is constant, was subtracted from the data such that the magnetization at high temperatures is zero. The data shown in the following reflect thus the magnetization of the bare samples.

For an easier access to the size of the moment, the magnetization is given as magnetization per copper or nickel atom in μ_B. To calculate these values from the measured data, we determined the surface area of the sample. Assuming a full coverage, we calculated the number of copper and nickel atoms per surface area based on the intended number of deposited layers. We then converted the magnetization measured in electromagnetic units (emu) to the magnetization per atom in μ_B.

There is a rather large error in this procedure. First of all, the samples had to be cut into pieces to fit into the magnet bore. After cutting, the size of the sample is less well defined and the sample could be damaged at the edges. During growth the samples are fixed to the sample holder with a wire leading over the four corners. Hence, the

corners are not covered with sample. In the case of the hybrid structures, which were grown on 10x10 mm^2 sized substrates, the corners were cut out off the sample and a piece of sample was measured that was fully covered with sample. In the case of the LCO film, which was grown on a 5x5 mm^2 sized substrate, these corners remained, leading to a bigger uncertainty when estimating the moment size.

We assume the full coverage of the substrate with a sample where a) all parts of the sample equally contribute to magnetism and b) exactly the intended amounts of the respective metals were deposited. For a) we note that incoherently grown parts of the sample will not exhibit magnetic order. For thin films, it is not simple to get good statistics on the amount of well-ordered compared to the amount of disordered sample volume. However, we can conclude from our TEM and XRD studies that the quality of the samples is indeed fairly high and that the majority of the sample is well ordered and will consequently contribute to the observed magnetism. Nonetheless, a certain error remains.

For b), we know that it is quite challenging in MBE growth to maintain exact atomic layer control. While in the case of heterostructures the errors in deposition potentially add to each other from layer to layer leading to uncertainty, in the case of thin film deposition, i.e., LCO here, errors possibly level each other leading to less uncertainty regarding the actual composition of the sample.

In addition to the sample related error, the error of the measurement itself is also quite significant. Between different measurements, we observed deviations of the magnetization of about 20%. The alignment of the sample in a field oriented perpendicular to the sample surface where the thickness of the sample is at most ~200 Å with the comparatively huge background of the substrate is everything else but straightforward. To circumvent this difficulty, the sample was cooled well below the magnetic transition temperature to 50 K in a field of 1000 Oe and then aligned in the standard procedure offered within the SQUID-VSM settings. Nonetheless, it seems likely that the measurement is sensitive to a small misalignment which is hard to avoid in the case of thin films with the magnetic field oriented perpendicular to the sample surface.

Overall, we can only be confident about the order of magnitude of the measured magnetic moment but not its exact value. On the other hand, the transition temperature is very consistent across different samples and different measurements.

All data shown here were taken with the magnetic field parallel to the out-of-plane direction (H ∥ c) to enable a comparison with the XMCD shown later on, which were taken with the same field orientation. For a good comparison of the size of the magnetic moments measured with SQUID and XMCD, measurements of the magnetization versus magnetic field would be beneficial. Unfortunately, the sample signal is too small to obtain meaningful data. Even after subtraction of the diamagnetic and paramagnetic contribution, there is no clear signal in magnetization versus field loops.

In all measurements of the magnetization versus temperature we observe a transition to a weak ferromagnetic state below ~165 K. We measured several hybrid structures with varying the nickelate (2–4 consecutive layers) and cuprate (1–3 consecutive layers) layer thicknesses as well as an LCO thin film. All samples show essentially the same behavior, i.e., the transition below ~165 K. The data for a selected set of samples is shown in Figure 5.32. Only field-cooled (FC) data are shown for clarity. Data taken after zero-field-cooling (ZFC) show either the same behavior as FC data only with a smaller magnetization or no transition at all.

The occurrence of the transition in all samples, including the LCO thin film, makes it appear likely that copper moments canted by the DM interaction are responsible therefor. What is remarkable though is that the transition temperature does not change,

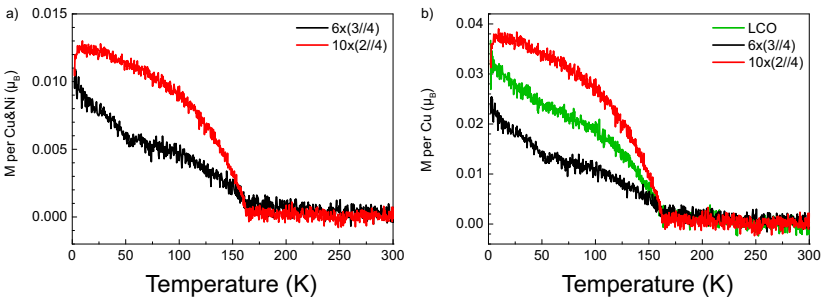

Figure 5.32: Magnetization versus temperature for two samples, 6x(3//4) and 10x(2//4) and an LCO reference film. A field of 100 Oe was applied in the out-of-plane direction, H ∥ c, while cooling to 2 K and while measuring upon warming-up. The paramagnetic and diamagnetic contribution of the substrate was subtracted. a) Magnetic moment in units of μ_B per Cu and Ni, assuming that both ions contribute equally to the magnetic moment. b) Magnetic moment in units of μ_B per Cu, assuming that only Cu ions contribute to the magnetic moment.

neither through heterostructuring nor by making the cuprate layer as thin as one atomic layer. This is remarkable because the magnetic correlations in bulk La_2CuO_4 are greatly influenced by any kind of doping, e.g., with strontium or oxygen. From x-ray absorption measurements we know that there are indeed changes of oxidation state between the different samples which should, in principle, affect the magnetic correlations.

A possible explanation is the occurrence of the same impurity phase in all the samples. Obviously, copper oxide (CuO) is a possible candidate. Bulk copper oxide orders antiferromagnetically below 230 K and undergoes an additional transition from an incommensurate to a commensurate state below 213 K. [145] However, both ordering temperatures are far away (~50 K and ~65 K) from the transition we observe. Taking into consideration that the transition temperature of our samples is that insensitive to any kind of disturbance, it appears unlikely that it is derived from CuO impurities.

This insensitivity hints towards strain being the main player in setting the borders for the magnitude of the antiferromagnetic correlations. To prove this assumption, we will have to grow a similar set of samples on different substrates and realize different strain states.

Although all our observations so far seem to indicate that the magnetism is solely based on the ordering of copper moments, we cannot exclude an ordering of *nickel moments*, either independent from the copper moments or coupled to them. Moreover, it is well known that, upon slight modification of the structural parameters (distortion of the structure through the substitution of the A site cation of $LaNiO_3$ or through heterostructuring), the nickel moments do order antiferromagnetically.

Based on the SQUID magnetization measurement, there is no indication for such an ordering. Neither is an anomaly observed in superlattices of LNO and $LaAlO_3$ with the LNO layers two u. c. thick. Their magnetic ordering, in contrast, is well studied with muon spin rotation and resonant magnetic x-ray scattering. [1, 2]. Hence, further measurement were necessary to test for magnetic ordering of nickel moments, here we studied x-ray magnetic cirular dichroism which will be discussed in the following section.

XMCD

While *SQUID* is very sensitive to even small magnetic moments, *XMCD* is element specific but not that sensitive to small moments. Hence, both methods are complimentary. In order to shed light onto the origin of the moment measured with SQUID, we measured XMCD at the copper and nickel $L_{2,3}$-edges. We do not observe any signal at all at the copper edge, but a weak signal at the nickel edge. We measured the dichroism at the nickel $L_{2,3}$-edges between 4.5 K and 165 K and observed an order-parameter like behavior (cf. Figure 5.36).

Copper $L_{2,3}$-edges

As we can see in Figure 5.33a, no magnetic circular dichroism is observed at the copper $L_{2,3}$-edges of the sample 10x(2//4). The small "wiggle" seen in the difference spectrum is probably due to a small energy shift in between the measurements. Since we did not measure a reference, we cannot adjust for such small energy shifts. The areas under each side of the wiggle cancel out each other, indicating that there is no net moment on the copper sites or that the moment is too small to be measured by XMCD.

In contrast to the hybrid sample, we do observe a small XMCD signal in an LCO thin film (Figure 5.33b) which is likely due to a canting of the spins due to the DM interaction. Since the magnitude of the DM interaction depends on the extent of the distortion away from the ideal, tetragonal structure, and the direction of the canting depends on the tilt pattern, this contrary behavior is an indication for a symmetry

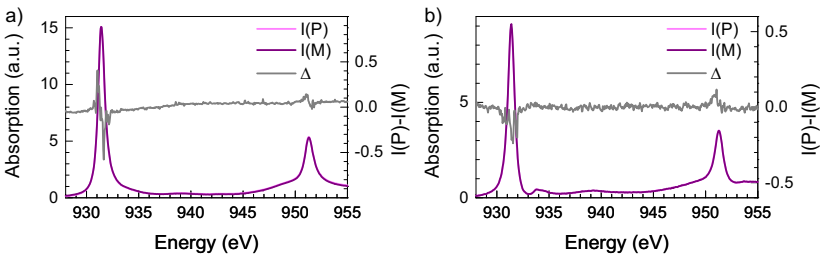

Figure 5.33: XAS measured at 6 K and 6 T with left and right circularly polarized light at the Cu $L_{2,3}$-edges together with the normalized dichroic signal. a) Sample 10x(2//4). b) LCO thin film.

alteration of the copper-oxygen octahedra upon heterostructuring. [138] It could either be that there is no distortion of the copper-oxygen octahedra in the hybrid structure – or only a very small one that would not lead to a measurable canting of the spins – or that the canted moments are coupled antiferromagnetically.

As we can see in Figure 5.34, where we compare reciprocal space maps around the (013) substrate peak of the LCO film and sample 10x(2//4), the LCO film is partially relaxed with an average in-plane lattice constant of ~3.83 Å (note that the pseudo-tetragonal in-plane lattice parameter of bulk LCO is 3.805 Å [107]). In the case of the hybrid sample, the center of the layer peak is at K ~ 1.004 indicating that the sample is slightly relaxed with an average in-plane lattice parameter of ~3.85 Å and that the hybrid sample is better strained to the substrate.

As a consequence, the copper-oxygen octahedra have less space to tilt and the DM interaction should be smaller since its magnitude is directly connected to these small distortions. Moreover, the strain can alter the rotation pattern of the copper-oxygen octahedra such that the spins will be canted in opposite directions due to the DM interaction, also leaving no net moment behind. In such a case, presumably fields of

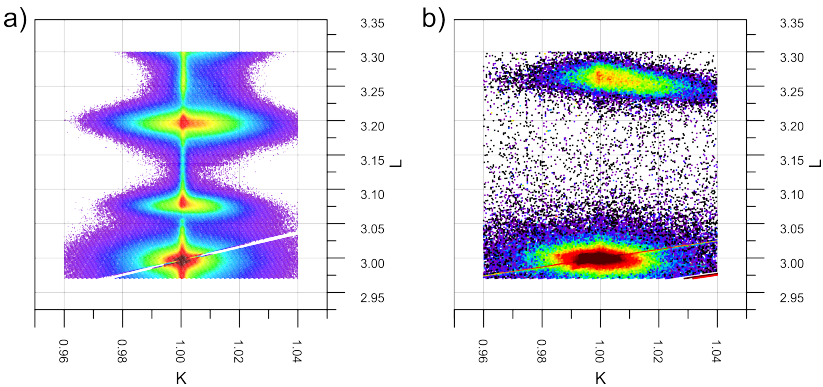

Figure 5.34: Reciprocal space maps around the (013) substrate peak of two samples. The intensity is on a logarithmic scale and in arbitrary units. The x- and y-direction are given in units of the reciprocal lattice of the LSAT substrate. a) Sample 10x(2//4) measured at the ANKA synchrotron at an energy of 10 keV. b) LCO film (same sample as used for the XMCD measurements shown in Figure 5.33b) measured in-house with Cu K_α radiation.

~20 T would be needed to flip the spins and to be able to detect a net ferromagnetic moment. [44]

The weak ferromagnetic signal observed in SQUID measurements supports the idea that there is indeed a canting of the moments caused by the DM interaction. However, the magnetic moments measured with a SQUID magnetometer (see discussion above) are very similar which contradicts the argument that the moment of the sample 10x(2//4) should be to small to be detected with XMCD. As discussed above, the error of our estimation is rather big and leaves enough room for interpretation to assume that the moment is actually smaller in the hybrid structures than in the thin film.

The origin of the possibly smaller magnetic moment in the sample 10x(2//4) can be the difference in the strain state of the two samples which also explains the lack of a measurable dichroism in the hybrid sample. It is possible that, if one manages to reduce the noise in the data, one would observe a dichroic signal also in the hybrid samples.

However, we cannot exclude that not only the magnitude of canting is reduced but also the spins cant in different directions.

Nickel $L_{2,3}$-edges

While there is no measurable circular dichroism at the copper edges, we do observe

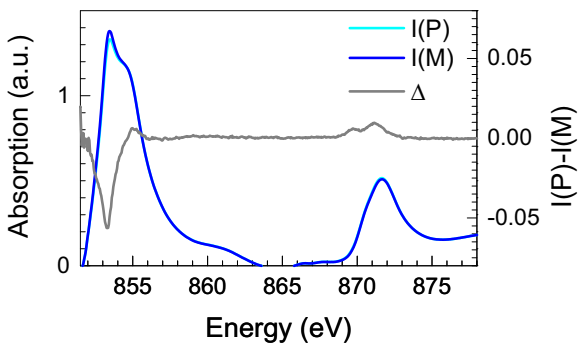

Figure 5.35: XAS of sample 10x(2//4) at Ni $L_{2,3}$-edges measured with circularly polarized light. The data were taken at 6 K and a magnetic field of 6 T perpendicular to the sample surface was applied. Two sets of data were averaged, namely with positive and negative fields. A Lorentzian was fitted to the lanthanum M_4-line, which overlaps with the nickel L_3-edge, and subtracted.

a small signal at the nickel $L_{2,3}$-edges. In Figure 5.35, XAS measured with right and left circularly polarized light together with the difference spectrum are shown. The data were taken at 6 K.

In this particular case, the data were taken with positive and negative fields (+6 T and -6 T) and the averages of the following two couples is shown: P@-6 T & M@+6 T and P@+6 T & M@-6 T. P and M in the legend denote the polarization in positive fields. This averaging leads to a strong improvement of data quality. Since the beamline where we did the experiments, UE46-PGM1 at BESSY Berlin, is not designed for quick field changes – it takes about an hour to go from +6 T to -6 T – we took the following temperature dependence only at positive fields.

Without averaging over positive and negative fields, there is a strong curved background in the difference spectra. To adjust therefor, we fitted those parts of the data, where we do not observe any dichroism, to the reference data set shown in Figure 5.35 with a third-order polynomial:

$$y = k \cdot z + k_0 + k_1 \cdot E + k_2 \cdot E^2 + k_3 \cdot E^3 \tag{5.1}$$

Here, y is the reference spectrum, z is the spectrum of interest, E is the energy and k_i are the fitting parameters. To reduce the number of fitting parameters and to make the fitting less ambiguous, we manually adjusted the spectra such that they are equal to 0 at the start (just before the lanthanum M_4-edge) and equal to 1 at the end (just after the nickel L_2-edge) of the measurement. We then fixed k to 1 and k_0 to 0.

Despite this procedure, the overlap of the nickel L_3-edge with the strong lanthanum M_4-line disturbs the spectra such that it would be difficult to extract useful information from the nickel L_3-edge. This is why we focused our analysis on the L_2-edge. With using only one edge in our analysis, we cannot apply the sum rules for XMCD and cannot determine the spin and orbital magnetic moment. However, the magnitude of the dichroic signal (here, we used the integration of the difference spectra over the L_2-edge) is nonetheless proportional to the magnetization. Thus, by measuring the temperature dependence of the dichroic signal, we can derive conclusions on the temperature dependence of the magnetic moment and hence on the magnetic ordering of the nickel sites.

In Figure 5.36a, the dichroic signal at various temperatures between 4.5 and 100 K

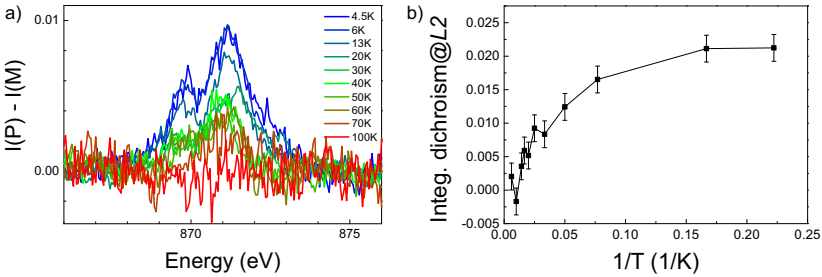

Figure 5.36: XMCD of the 10x(2//4) sample. a) difference spectra of positive (P) and negative (M) polarization at various temperatures. b) Integrated dichroic signal (from (a)), which is proportional to χ, versus the inverse temperature.

is plotted. We can see that the dichroism remains relatively constant at very low temperatures before it starts to decrease and finally vanishes at about 100 K. A plot of the integrated area against the inverse temperature confirms the assumption that the temperature dependence of the magnetization deviates from what one would expect from a paramagnet.

However, the measurements were undertaken at relatively high fields of 6 T. One might assume that the polarization of the (para)magnetic moments saturates at low temperatures and what we see is this saturation due to the low temperatures and high field rather than antiferro- or ferromagnetic behavior. The Curie law is only valid for

$$T \gg \frac{g \cdot \mu_B B}{k_B} \approx 8\,K$$

where T is the temperature, g is the gyromagnetic factor (here $g \approx 2$), μ_B is the Bohr magneton ($\mu_B = 9.274 \cdot 10^{-24}\,\mathrm{J \cdot T^{-1}}$), B the magntic field and k_B the Boltzmann constant ($k_B = 1.381 \cdot 10^{-23}\,\mathrm{J \cdot K^{-1}}$). At the lowest temperatures measured, we are close to that value. In order to determine the validity of our conclusions, one would have to fit the *Brillouin function* to the temperature dependence of magnetization. [32]

On the other hand, the signal for a spin-half or spin-one system (our sample should be somewhere in between) under full polarization of the magnetic moments, should be much larger than the small signal we observe. In principle, the dichroism stemming from a full polarization of magnetic moments, should be as sizable as in other,

ferromagnetic nickel compounds. [146, 147]

A similar trend of magnetization was observed in (2//2) superlattices of LNO and LAO – $[(LaNiO_3)_2(LaAlO_3)_2]_l$. In this case it is known from resonant magnetic x-ray diffraction that these compounds undergo a transition to a SDW state. [2, 148] Hence, we see a strong indication that the nickel moments are indeed ordered below ~100 K.

Conclusion

To sum up our magnetic measurements, we find for all samples, nickelate-cuprate hybrid structures and La_2CuO_4 thin films alike, a magnetic transition in magnetization measurements with a SQUID magnetometer at 165 K. This transition is due to an antiferromagnetic ordering of copper moments where the moments are canted out of the copper-oxygen planes because of the DM interaction. The canted moment is bigger for an LCO film than for the hybrid samples which can be related to a change of symmetry of the copper-oxygen octahedra upon heterostructuring. Such an ordering has been observed in many cuprates. However, the magnetic ordering temperature in the cuprates is usually very sensitive to doping. Hence, it is peculiar that the transition occurs at the same temperature for all investigated materials although we could show in the previous section (Chapter 5.3.1) that the oxidation state does differ between the samples.

With XMCD measurements, we could show that there is an indication for the ordering of nickel moments below ~100 K. Yet, we still have to exclude the possibility that the observed temperature dependence of the dichroic signal is due to a saturation of paramagnetic moments. In particular, since the lack of a transition in SQUID measurements sheds some doubt on our interpretation. To dissipate the doubt, it is worthwhile to mention that no feature is observed in magnetization measurements of nickelate-aluminate superlattices – $[(LaNiO_3)_2(LaAlO_3)_2]_l$ – where the magnetic ordering is well studied with muon spin rotation and resonant x-ray diffraction. [1, 2]

A magnetic ordering in a lanthanum nickelate with four consecutive layers directly connected via their apical oxygen atoms is unusual. Although magnetism was discussed for the RP phases, no solid evidence for long-range ordering has been found so far. However, because of the lack of high-quality single crystals, XMCD measurements of RP phases are missing up to date. [140, 141, 144]

Since we have now epitaxially grown thin films of the RP phases at hand, it could be interesting to study their magnetic properties in greater detail and compare their behavior with our hybrid structures.

Moreover, the observation of a magnetic peak in resonant diffraction would lend a strong support to our interpretation. However, the respective measurement will be extremely difficult because the *c* axis of the samples is quite large, leading to a plethora of strong structural Bragg reflections that are likely to overlap with the presumably very weak magnetic peak.

5.3.3 Electrical transport measurements

All of the above discussed electronic structure and ordering phenomena are obviously related to the electrical transport behavior of the samples. And both, intrinsic and extrinsic properties of the samples contribute to resistance. Therefore, excellent samples and good statistics are required to draw definite conclusions from transport behavior and to rule out sample quality being the cause of the observed properties. Admittedly, at the moment we lack both. Nonetheless, the data we have at hand may lay the basis for future investigations.

Before we turn towards the transport behavior of the nickelate-cuprate hybrid structures, we will first discuss the transport behavior of La_2CuO_4 and $La_{n+1}Ni_nO_{3n+1}$.

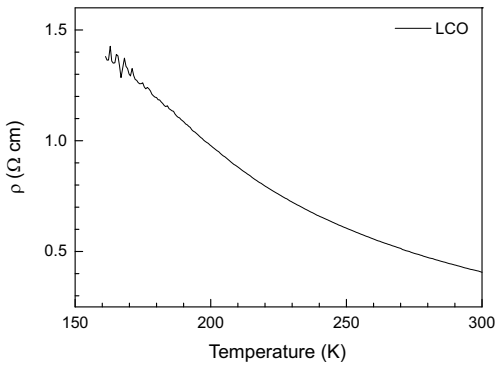

Figure 5.37: Temperature-dependent resistivity of LCO.

Undoped La_2CuO_4 is insulating (see also Figure 5.37). Moreover, it has a sizeable, negative magnetoresistance (MR) below the magnetic transition. Its magnitude reaches up to ~20%. [149] Upon hole-doping with either oxygen or strontium metallic and / or superconducting behavior is observed.

Among the RP-nickelates, $La_{n+1}Ni_nO_{3n+1}$, $LaNiO_3$ is metallic in the whole temperature regime. Upon heterostructuring, a weakly insulating state is observed when only two consecutive nickelate layers remain, sandwiched between a large band gap insulator. A fully insulating behavior is observed when the layer thickness is further reduced and only a single, isolated nickelate layer remains. [1, 2]

Fully oxygenated samples of $La_{n+1}Ni_nO_{3n+1}$, $n = 2$ or 3, were reported to be metallic, while oxygen-deficient samples are semiconducting. [141, 143, 144]

Our RP samples with $n = 3$ or 4 (grey, dashed lines in Figures 5.38a,b) are metallic with an upturn below ~100 K and the sample with $n = 2$ is insulating (grey, dashed line in Figure 5.38c). The upturn at low temperatures and the small negative magnetoresistance (Figure 5.38d) are an indication for weak localization or oxygen-deficiency.

In comparison, our nickelate-cuprate hybrid structures show a very similar behavior at first glance (colored, solid lines in Figures 5.38a-c). They have similar values of resistivity but the upturn at low temperatures is mostly smaller. As magnetic ordering affects the electrical transport and often an anomaly in electrical resistivity is observed when magnetic order sets in, it is worth to mention that there is no obvious anomaly in our hybrid samples.

In a stark contrast to our RP phases and to the reported negative MR of LCO, some of our hybrid structures show a small, positive MR at low temperatures (Figure 5.38d). Moreover, in those hybrid samples that do show a negative MR, the MR sets in at lower temperatures than in the corresponding RP phases. This is an indication that the behavior of the hybrid structure is indeed different from the corresponding RP phase and from LCO.

The small positive MR observed in some samples is suggestive for weak anti-localization (WAL) due to spin-orbit coupling. [87, 150] Moreover, for the joint contribution of both layers, nickelate and cuprate layers alike, to electronic conduction. It seems unlikely that our observation should be explained by sample quality alone.

Nonetheless, to confirm our findings regarding the weak (anti)localization, angle-

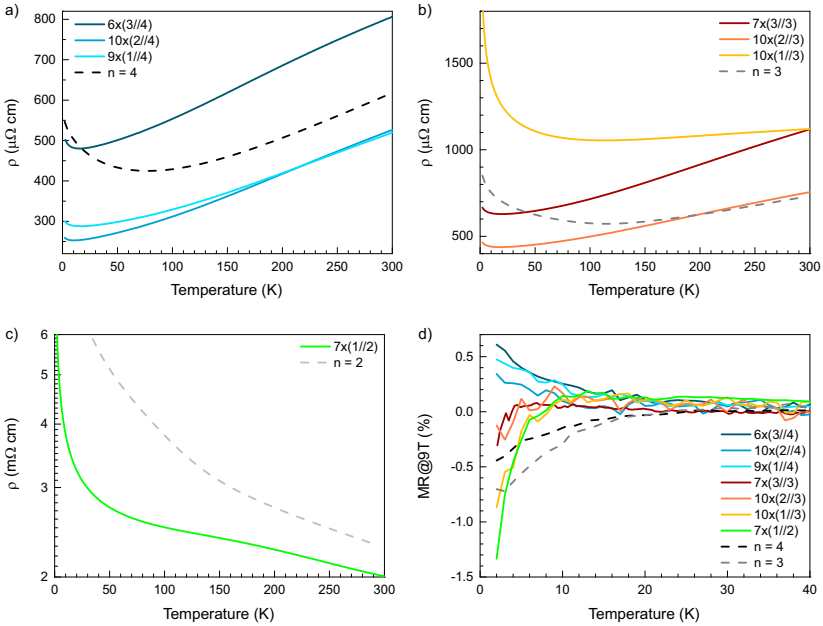

Figure 5.38: Temperature-dependent resistivity and temperature-dependent magnetoresistance (MR) of different hybrid samples, $[(La_2CuO_4)_nLaO(LaNiO_3)_m]_l - lx(n//m)$ (colored, solid lines) and RP phases, $La_{n+1}Ni_nO_{3n+1}$(grey, dashed lines). a) A series of samples with each four consecutive nickelate layers and a decreasing number of cuprate layers. b) A series of samples with each three consecutive nickelate layers and a decreasing number of cuprate layers. c) A hybrid sample with two consecutive nickelate layers and the corresponding RP phase. d) MR measured at 9T of the samples shown in a-c).

dependent studies of the MR are necessary and to confirm the contribution of, in particular, the cuprate layers, a measurement of the electrical transport along the *c*-axis would be helpful.

5.4 Conclusions

In the course of this chapter, we showed how to exploit the unique possibilities offered by our MBE system. The control over individual atomic layers enabled us to grow a novel kind of structure consisting of Ruddlesden-Popper-type lanthanum nickelate

layers ($La_{n+1}Ni_nO_{3n+1}$) and lanthanum cuprate (La_2CuO_4) layers following the K_2NiF_4 structure type. The sum formula of such a structure is $[(La_2CuO_4)_nLaO(LaNiO_3)_m]_l$ or in short lx(n//m). All samples presented in this work were grown on LSAT substrate which is a solid solution of $LaAlO_3$ and Sr_2AlTaO_6 in a ratio of three to seven.

We evaluated the sample quality via x-ray diffraction and scanning transmission electron microscopy (STEM) and showed how to improve the growth conditions. Nevertheless there is a strong variation in sample quality, especially the growth of structures with very thin cuprate and / or nickelate layers is prone to the formation of faults since a lack or surplus of nickel or copper cannot be leveled in the following layer.

In the sample with the highest structural quality, $[(La_2CuO_4)_3LaO(LaNiO_3)_4]_6$ – 6x(3//4), we were able to not only map the positions of the metal atoms but also that of the oxygen atoms with TEM. Here, we saw that both, the nickel-oxygen and the copper-oxygen octahedra, are elongated along the out-of-plane direction with respect to the in-plane lattice parameter of 3.87 Å. Cu^{2+} with its d^9 electronic configuration is Jahn-Teller active. Hence, such an elongation is expected. However, when comparing the measured distances with bulk values and with the expected values under the assumption of volume conservation, we noticed that the copper-oxygen octahedra are less elongated. The underlying mechanism could be an interfacial charge transfer, interfacial oxygen interstitials or vacancies, and interface roughness. In the case of the nickel-oxygen octahedra, there is a significant difference between interfacial (apical O–O distance = 4.11 Å) and inner (apical O–O distance = 3.91 Å) nickelate layers. The difference between the two different nickelate layers can easily be explained by their different chemical environment.

Through x-ray absorption spectroscopy (XAS) at the copper and nickel $L_{2,3}$-edges, we could show that copper is, as expected, close to a +II oxidation state. However, we also see variations from sample to sample that cannot be explained in a straightforward manner. The oxidation state of nickel is in between +II and +III and also here we see a sample-to-sample variation whose origin was discussed in detail but in order to arrive at a certain conclusion, a comparison of a whole series of samples is needed.

The use of linearly polarized light in XAS enabled us to observe the preferred occupation of the out-of-plane, $3d_{3z^2-r^2}$, orbital in both cases – nickel and copper – which

we directly connect to the elongation of octahedra measured with STEM.

In magnetization measurements with a SQUID magnetometer, we observe a transition to a weak ferromagnetic state below ~165 K in all samples, even in ones that have only single isolated cuprate layers. The occurrence of a transition at the same temperature in a La_2CuO_4 thin film suggests that the magnetic ordering is related to a canting of copper moments out of the copper-oxygen plane due to the Dzyaloshinskii-Moriya (DM) interaction. There is no second transition in any of the samples which would otherwise indicate a magnetic ordering of the nickel moments.

To further investigate the magnetic ordering, we conducted XAS with circularly polarized light (XMCD). The canting of copper moments due to the DM interaction should lead to a small dichroic signal at the copper $L_{2,3}$-edges. [44] There is indeed an XMCD signal in the case of the LCO film. However, no signal is measured for a 10x(2//4)-sample suggesting smaller distortions from the ideal, tetragonal structure in the latter case and a corresponding smaller XMCD signal which cannot be resolved.

We do observe a small dichroic signal at the nickel $L_{2,3}$-edges. Its temperature dependence suggests a magnetic ordering of nickel moments. However, the possibility of a saturation of paramagnetic moments, which would result in a similar temperature dependence, cannot be ruled out completely. To corroborate our interpretation of ordered nickel moments, it is worth to mention that superlattices of $LaNiO_3$ and $LaAlO_3$ with only two consecutive nickelate layers, whose magnetic ordering has been proven and studied with muon spin rotation and resonant magnetic x-ray scattering, [1, 2] show a very similar behavior. [148]

Electrical transport measurements show that most nickelate-cuprate hybrid structures are metallic. Only the sample with as few as two consecutive nickelate layers is semiconducting in the full measured temperature range. The value of the resistivity is comparable to that of corresponding RP phases with an equal number of consecutive nickelate layers.

Small differences in the transport behavior suggest a contribution of the LCO layers to the transport although bulk and thin film LCO are insulating. Moreover, the small positive magnetoresistance of some samples, which is in a stark contrast to measurements of corresponding RP phases, suggests a contribution of weak antilocalization caused by spin-orbit coupling.

For further studies on our novel material system, we need to improve sample quality and to conduct more in-depth measurements.

In particular, to shed more light onto the magnetic ordering of the nickel moments, a measurement of the x-ray magnetic *linear* dichroism at various field strengths and temperatures in combination with a more careful study of the x-ray *magnetic* dichroism could prove itself useful.

The realization of different strain states by using, for example, $SrTiO_3$ or $LaSrAlO_4$ as a substrate could furthermore contribute to the understanding on why the magnetic transition is that insensitive to any kind of perturbation and remains at 165 K for all samples measured in the course of this work.

One of the challenges of MBE growth is to achieve the deposition of a dopant layer that is confined to one atomic layer, so-called δ-doping. [151, 152] In real samples, where diffusion, in particular at high temperatures, cannot be eliminated there is al-

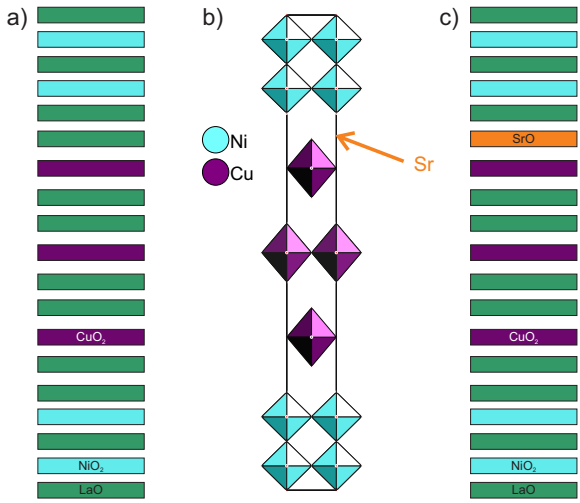

Figure 5.39: a) Atomic layer sequence for the growth of $[(La_2CuO_4)_3LaO(LaNiO_3)_4]$. b) The corresponding unit cell for a sample grown according to the layer sequence depicted in a). The arrow indicates a potential position for the replacement of a lanthanum layer by strontium. c) Atomic layer sequence for the growth of the δ-doped structure. It is expected that strontium will be confined to the indicated layer and the one on top.

ways a distribution of dopant concentration across several layers. Baiutti *et al.* [152] grew La_2CuO_4 thin films where individual lanthanum layers were replaced by strontium. They showed that the doping profile is asymmetric. Whereas it is very sharp at the bottom side of the inserted strontium layer, the concentration of strontium gradually decays above. By depositing a material that would be instable upon strontium doping, it is speculated that one can reduce or even eliminate the strontium diffusion in growth-direction and get closer towards a true δ-doping. Our class of novel materials is an ideal test candidate for such an approach. A strontium doping of the nickelate layers would drive nickel towards a +IV oxidation state which is not stable within our typical growth conditions. Hence, one can expect that strontium remains confined to one atomic layer if it is placed just before the nickelate layer as depicted in Figure 5.39.

One last question whose definite answer remains inaccessible with the available methods is the puzzle of oxygen vacancies and interstitials. In bulk samples, thermogravimetric analysis or iodometric titration are used to determine the oxygen content. For obvious reasons, these methods are not suitable for thin films and heterostructures. Instead, the best way is to use indirect measures like x-ray absorption and compare sample-to-sample deviations to gain insight into the level of oxidation.

Bibliography

[1] Boris, A. V. *et al.* Dimensionality control of electronic phase transitions in nickel-oxide superlattices. *Science* **332**, 937–940 (2011). URL http://science.sciencemag.org/content/332/6032/937. 9, 17, 27, 86, 103, 111, 112, 161, 164, 170, 172, 175

[2] Frano, A. *et al.* Orbital control of noncollinear magnetic order in nickel oxide heterostructures. *Phys. Rev. Lett.* **111**, 106804 (2013). URL http://link.aps.org/doi/10.1103/PhysRevLett.111.106804. 9, 17, 27, 103, 111, 112, 161, 164, 170, 172, 175

[3] Chaloupka, J. & Khaliullin, G. Orbital order and possible superconductivity in $LaNiO_3$/ $LaMO_3$ superlattices. *Phys. Rev. Lett.* **100**, 016404 (2008). URL http://link.aps.org/doi/10.1103/PhysRevLett.100.016404. 9, 17, 27, 92

[4] Hansmann, P. *et al.* Turning a nickelate fermi surface into a cupratelike one through heterostructuring. *Phys. Rev. Lett.* **103**, 016401 (2009). 9, 17, 27, 92

[5] Son, J. *et al.* Low-dimensional Mott material: Transport in ultrathin epitaxial $LaNiO_3$ films. *Applied Physics Letters* **96**, 062114 (2010). URL http://scitation.aip.org/content/aip/journal/apl/96/6/10.1063/1.3309713. 10, 18, 27, 69, 70, 71, 96, 97, 101, 102, 107, 112

[6] Scherwitzl, R. *et al.* Metal-insulator transition in ultrathin $LaNiO_3$ films. *Phys.*

Rev. Lett. **106**, 246403 (2011). URL http://link.aps.org/doi/10.1103/PhysRevLett.106.246403. 70, 71, 96, 97, 103, 107, 108, 112

[7] Zhou, J.-S., Marshall, L. G. & Goodenough, J. B. Mass enhancement versus Stoner enhancement in strongly correlated metallic perovskites: $LaNiO_3$ and $LaCuO_3$. *Phys. Rev. B* **89**, 245138 (2014). URL http://link.aps.org/doi/10.1103/PhysRevB.89.245138. 72, 86, 96, 97, 100, 112, 116

[8] King, P. D. C. *et al.* Atomic-scale control of competing electronic phases in ultrathin $LaNiO_3$. *Nat Nano* **9**, 443–447 (2014). URL http://dx.doi.org/10.1038/nnano.2014.59. 10, 18, 27, 70, 72, 86, 97, 100, 101, 103, 105, 106, 112

[9] Gayathri, N., Raychaudhuri, A. K., Xu, X. Q., Peng, J. L. & Greene, R. L. Electronic conduction in $LaNiO_{3-\delta}$: the dependence on the oxygen stoichiometry δ. *Journal of Physics: Condensed Matter* **10**, 1323 (1998). URL http://stacks.iop.org/0953-8984/10/i=6/a=015. 12, 19, 71, 96, 97, 101, 102

[10] Catalan, G. Progress in perovskite nickelate research. *Phase Transitions* **81**, 729–749 (2008). URL http://dx.doi.org/10.1080/01411590801992463. http://dx.doi.org/10.1080/01411590801992463. 24, 25

[11] Park, J.-C., Kim, D.-K., Byeon, S.-H. & Kim, D. XANES study on Ruddlesden-Popper phase, $La_{n+1}Ni_nO_{3n+1}$ (n = 1, 2, and ∞). *Journal of Synchrotron Radiation* **8**, 704–706 (2001). URL http://dx.doi.org/10.1107/S0909049500015983. 25

[12] Alonso, J. A. *et al.* Charge disproportionation in $RNiO_3$ (R = Tm, Yb) perovskites observed *in situ* by neutron diffraction and ^{57}Fe probe Mössbauer spectroscopy. *Phys. Rev. B* **87**, 184111 (2013). URL http://link.aps.org/doi/10.1103/PhysRevB.87.184111. 25

[13] Johnston, S., Mukherjee, A., Elfimov, I., Berciu, M. & Sawatzky, G. A. Charge disproportionation without charge transfer in the rare-earth-element

nickelates as a possible mechanism for the metal-insulator transition. *Phys. Rev. Lett.* **112**, 106404 (2014). URL http://link.aps.org/doi/10.1103/PhysRevLett.112.106404. 25, 77, 92, 93, 142

[14] Scagnoli, V. *et al.* Role of magnetic and orbital ordering at the metal-insulator transition in $NdNiO_3$. *Phys. Rev. B* **73**, 100409 (2006). URL http://link.aps.org/doi/10.1103/PhysRevB.73.100409. 25

[15] Berner, G. *et al.* Dimensionality-tuned electronic structure of nickelate superlattices explored by soft-x-ray angle-resolved photoelectron spectroscopy. *Phys. Rev. B* **92**, 125130 (2015). URL http://link.aps.org/doi/10.1103/PhysRevB.92.125130. 27, 103, 106

[16] Benckiser, E. *et al.* Orbital reflectometry of oxide heterostructures. *Nat Mater* **10**, 189–193 (2011). URL http://www.nature.com/nmat/journal/v10/n3/full/nmat2958.html. 27, 47, 50, 76, 77, 79, 80, 92, 112, 137

[17] Wu, M. *et al.* Strain and composition dependence of orbital polarization in nickel oxide superlattices. *Phys. Rev. B* **88**, 125124 (2013). URL http://link.aps.org/doi/10.1103/PhysRevB.88.125124. 27, 48, 50, 77, 78, 79, 80, 92, 112, 137

[18] Bednorz, J. G. & Müller, K. A. Possible high T_c superconductivity in the Ba–La–Cu–O system. *Zeitschrift für Physik B Condensed Matter* **64**, 189–193 (1986). URL http://dx.doi.org/10.1007/BF01303701. 28

[19] Wu, M. K. *et al.* Superconductivity at 93 K in a new mixed-phase Y-Ba-Cu-O compound system at ambient pressure. *Phys. Rev. Lett.* **58**, 908–910 (1987). URL http://link.aps.org/doi/10.1103/PhysRevLett.58.908. 28

[20] Norman, M. R. The challenge of unconventional superconductivity. *Science* **332**, 196–200 (2011). URL http://science.sciencemag.org/content/332/6026/196. http://science.sciencemag.org/content/332/6026/196.full.pdf. 28

[21] Ohtomo, A. & Hwang, H. Y. A high-mobility electron gas at the $LaAlO_3$/srtio$_3$ heterointerface. *Nature* **427**, 423–426 (2004). URL http://dx.doi.org/10.1038/nature02308. 30

[22] Reyren, N. *et al.* Superconducting interfaces between insulating oxides. *Science* **317**, 1196–1199 (2007). URL http://science.sciencemag.org/content/317/5842/1196. http://science.sciencemag.org/content/317/5842/1196.full.pdf. 30

[23] Falcón, H., Goeta, A. E., Punte, G. & Carbonio, R. E. Crystal structure refinement and stability of $LaFe_xNi_{1-x}O_3$ solid solutions. *Journal of Solid State Chemistry* **133**, 379–385 (1997). 30

[24] Uecker, R. *et al.* Properties of rare-earth scandate single crystals (Re=Nd–Dy). *Journal of Crystal Growth* **310**, 2649–2658 (2008). URL http://www.sciencedirect.com/science/article/pii/S0022024808000675. 30

[25] Herman, M. A. & Sitter, H. *Characterization Techniques*, 135–227 (Springer Berlin Heidelberg, Berlin, Heidelberg, 1996). URL http://dx.doi.org/10.1007/978-3-642-80060-3_4. 33

[26] Sullivan, M. C. *et al.* Complex oxide growth using simultaneous in situ reflection high-energy electron diffraction and x-ray reflectivity: When is one layer complete? *Applied Physics Letters* **106**, 031604 (2015). URL http://scitation.aip.org/content/aip/journal/apl/106/3/10.1063/1.4906419. 34, 59, 61

[27] Ohring, M. *Materials Science of Thin Films.*, vol. 2nd ed (Academic Press, 2002). URL http://search.ebscohost.com.ezproxy.fkf.mpg.de/login.aspx?direct=true&db=nlebk&AN=92177&site=ehost-live&scope=site. 34

[28] Koster, G., Kropman, B. L., Rijnders, G. J. H. M., Blank, D. H. A. & Rogalla, H. Quasi-ideal strontium titanate crystal surfaces through formation of strontium hydroxide. *Applied Physics Letters* **73**, 2920–2922

(1998). URL http://scitation.aip.org/content/aip/journal/apl/73/20/10.1063/1.122630. 36

[29] Kleibeuker, J. E. *et al.* Atomically defined rare-earth scandate crystal surfaces. *Advanced Functional Materials* **20**, 3490–3496 (2010). URL http://dx.doi.org/10.1002/adfm.201000889. 36

[30] Baiutti, F., Christiani, G. & Logvenov, G. Towards precise defect control in layered oxide structures by using oxide molecular beam epitaxy. *Beilstein J. Nanotechnol.* **5**, 596–602 (2014). 36, 37

[31] Bragg, W. H. & Bragg, W. L. The reflection of x-rays by crystals. *Proceedings of the Royal Society of London A: Mathematical, Physical and Engineering Sciences* **88**, 428–438 (1913). URL http://rspa.royalsocietypublishing.org/content/88/605/428. 41

[32] Ashcroft, N. W. & Mermin, N. D. *Solid State Physics* (Brooks/Coole Thomson Learning, 1976). 42, 50, 56, 94, 95, 109, 169

[33] Nelson, J. & Riley, D. An experimental investigation of extrapolation methods in the derivation of accurate unit-cell dimensions of crystals. *Proceedings of the Physical Society* **57**, 160–177 (1945). URL https://www.scopus.com/inward/record.uri?eid=2-s2.0-9944264851&partnerID=40&md5=b02e5e04433c8c388a0cc65e7fc9b461. Cited By 629. 42

[34] Lüth, H. *Solid Surfaces, Interfaces and Thin Films*. Graduate Texts in Physics (Cham: Springer International Publishing, 2015), 6th ed. 2015 edn. URL http://dx.doi.org/10.1007/978-3-319-10756-1?nosfx=y. 43, 44

[35] Bergamaschi, A. *et al.* The MYTHEN detector for X-ray powder diffraction experiments at the Swiss Light Source. *Journal of Synchrotron Radiation* **17**, 653–668 (2010). URL http://dx.doi.org/10.1107/S0909049510026051. 45, 123

[36] Hippert, F. *Neutron and X-ray Spectroscopy* (Springer Netherlands, Dordrecht, 2006). URL http://dx.doi.org/10.1007/1-4020-3337-0?nosfx=y. (Online service). 45, 46

[37] de Groot, F. X-ray absorption and dichroism of transition metals and their compounds. *Journal of Electron Spectroscopy and Related Phenomena* **67**, 529 – 622 (1994). URL http://www.sciencedirect.com/science/article/pii/036820489302041J. 46, 47, 151

[38] Haverkort, M. W., Zwierzycki, M. & Andersen, O. K. Multiplet ligand-field theory using Wannier orbitals. *Phys. Rev. B* **85**, 165113 (2012). URL http://link.aps.org/doi/10.1103/PhysRevB.85.165113. 46, 76

[39] de Groot, F. X-ray absorption of transition metal oxides: An overview of the theoretical approaches. *Journal of Electron Spectroscopy and Related Phenomena* **62**, 111 – 130 (1993). URL http://www.sciencedirect.com/science/article/pii/036820489380009B. 46

[40] van der Laan, G. Sum rules and fundamental spectra of magnetic x-ray dichroism in crystal field symmetry. *Journal of the Physical Society of Japan* **63**, 2393–2400 (1994). URL http://dx.doi.org/10.1143/JPSJ.63.2393. 47

[41] Stöhr, J., Padmore, H. A., Anders, S., Stammler, T. & Scheinfein, M. R. Principles of x-ray magnetic dichroism spectromicroscopy. *Surface Review and Letters* **05**, 1297–1308 (1998). URL http://www.worldscientific.com/doi/abs/10.1142/S0218625X98001638. 48, 156

[42] Alders, D. *et al.* Magnetic x-ray dichroism study of the nearest-neighbor spin-spin correlation function and long-range magnetic order parameter in antiferromagnetic NiO. *EPL (Europhysics Letters)* **32**, 259 (1995). URL http://stacks.iop.org/0295-5075/32/i=3/a=012. 48, 156

[43] Carra, P., Thole, B. T., Altarelli, M. & Wang, X. X-ray circular dichroism and local magnetic fields. *Phys. Rev. Lett.* **70**, 694–697 (1993). URL http://link.aps.org/doi/10.1103/PhysRevLett.70.694. 48

[44] De Luca, G. M. *et al.* Weak magnetism in insulating and superconducting cuprates. *Phys. Rev. B* **82**, 214504 (2010). URL http://link.aps.org/doi/10.1103/PhysRevB.82.214504. 49, 160, 167, 175

[45] Wu, M. *Orbital reflectometry of nickel oxide heterostructures*. Ph.D. thesis, University of Stuttgart (2015). URL http://dx.doi.org/10.18419/opus-6873. 50, 75

[46] Meyer, J. R. *et al.* Methods for magnetotransport characterization of IR detector materials. *Semiconductor Science and Technology* **8**, 805 (1993). URL http://stacks.iop.org/0268-1242/8/i=6S/a=004. 51

[47] van der Pauw, L. J. A method of measuring specific resistivity and Hall effect of discs of arbitrary shape. *Philips Research Reports* **13**, 1–9 (1958). 51, 52, 53

[48] Ramadan, A. A., Gould, R. D. & Ashour, A. On the van der Pauw method of resistivity measurements. *Thin Solid Films* **239**, 272–275 (1994). URL http://www.sciencedirect.com/science/article/pii/004060909490863X. 52

[49] Hurd, C. *The Hall Effect in Metals and Alloys*. The International Cryogenics Monograph Series (Springer US, Plenum Press, New York, 1972). 54, 55, 105, 109

[50] Pippard, A. B. *Magnetoresistance in Metals*, vol. 2 of *Cambridge studies in low temperature physics* (Campridge Univ. Pr., Cambridge, 1989). 54, 55, 106, 108, 109, 111

[51] Jaramillo, R., Ha, S. D., Silevitch, D. M. & Ramanathan, S. Origins of bad-metal conductivity and the insulator-metal transition in the rare-earth nickelates. *Nat Phys* **10**, 304–307 (2014). URL http://dx.doi.org/10.1038/nphys2907. 56

[52] Mott, N. F. Conduction in non-crystalline systems IX. the minimum metallic conductivity. *Philosophical Magazine* **26**, 1015–1026 (1972). URL http://dx.doi.org/10.1080/14786437208226973. 56, 70, 71

[53] Hikami, S., Larkin, A. I. & Nagaoka, Y. Spin-orbit interaction and magnetoresistance in the two dimensional random system. *Progress of Theoretical Physics* **63**, 707–710 (1980). URL http://ptp.oxfordjournals.org/content/63/2/707.abstract. 56

[54] Noun, W., Berini, B., Dumont, Y., Dahoo, P. R. & Keller, N. Correlation between electrical and ellipsometric properties on high-quality epitaxial thin films of the conductive oxide $LaNiO_3$ on STO (001). *Journal of Applied Physics* **102** (2007). URL http://scitation.aip.org/content/aip/journal/jap/102/6/10.1063/1.2781517. 59, 101

[55] Ngai, J. H. *et al.* Achieving A-site termination on $La_{0.18}Sr_{0.82}Al_{0.59}Ta_{0.41}O_3$ substrates. *Advanced Materials* **22**, 2945–2948 (2010). URL http://dx.doi.org/10.1002/adma.200904328. 65, 84

[56] Boschker, H. *et al.* Uniaxial contribution to the magnetic anisotropy of $La_{0.67}Sr_{0.33}MnO_3$ thin films induced by orthorhombic crystal structure. *Journal of Magnetism and Magnetic Materials* **323**, 2632 – 2638 (2011). URL http://www.sciencedirect.com/science/article/pii/S0304885311003283. 65

[57] Macke, S. *et al.* Element specific monolayer depth profiling. *Advanced Materials* **26**, 6554–6559 (2014). URL http://dx.doi.org/10.1002/adma.201402028. 68, 81

[58] Gray, A. X. *et al.* Insulating state of ultrathin epitaxial $LaNiO_3$ thin films detected by hard x-ray photoemission. *Phys. Rev. B* **84**, 075104 (2011). URL http://link.aps.org/doi/10.1103/PhysRevB.84.075104. 69, 70, 71

[59] Detemple, E. *et al.* Polarity-driven nickel oxide precipitation in $LaNiO_3$-$LaAlO_3$ superlattices. *Applied Physics Letters* **99** (2011). URL http://scitation.aip.org/content/aip/journal/apl/99/21/10.1063/1.3663568. 69, 84, 85, 113

[60] Scherwitzl, R., Zubko, P., Lichtensteiger, C. & Triscone, J.-M. Electric-field tuning of the metal-insulator transition in ultrathin films of $LaNiO_3$. *Applied*

Physics Letters **95** (2009). URL http://scitation.aip.org/content/aip/journal/apl/95/22/10.1063/1.3269591. 70, 71, 101, 102, 103

[61] Hayward, M. A., Green, M. A., Rosseinsky, M. J. & Sloan, J. Sodium hydride as a powerful reducing agent for topotactic oxide deintercalation: Synthesis and characterization of the nickel(I) oxide $LaNiO_2$. *Journal of the American Chemical Society* **121**, 8843–8854 (1999). URL http://dx.doi.org/10.1021/ja991573i. http://dx.doi.org/10.1021/ja991573i. 71

[62] Crespin, M., Isnard, O., Dubois, F., Choisnet, J. & Odier, P. $LaNiO_2$: Synthesis and structural characterization. *Journal of Solid State Chemistry* **178**, 1326 – 1334 (2005). URL http://www.sciencedirect.com/science/article/pii/S0022459605000125.

[63] Kawai, M. *et al.* Reversible changes of epitaxial thin films from perovskite $LaNiO_3$ to infinite-layer structure $LaNiO_2$. *Applied Physics Letters* **94**, 082102 (2009). URL http://scitation.aip.org/content/aip/journal/apl/94/8/10.1063/1.3078276. 71

[64] Guan, L. *et al.* Electronic structure and optical properties of $LaNiO_3$: First-principles calculations. *Solid State Communications* **150**, 2011 – 2014 (2010). URL http://www.sciencedirect.com/science/article/pii/S0038109810004874. 77

[65] Mazin, I. I. *et al.* Charge ordering as alternative to Jahn-Teller distortion. *Phys. Rev. Lett.* **98**, 176406 (2007). URL http://link.aps.org/doi/10.1103/PhysRevLett.98.176406. 77, 92

[66] de Groot, F., Arrio, M., Sainctavit, P., Cartier, C. & Chen, C. Fluorescence yield detection: Why it does not measure the x-ray absorption cross section. *Solid State Communications* **92**, 991 – 995 (1994). URL http://www.sciencedirect.com/science/article/pii/0038109894900272. 77

[67] Medarde, M. *et al.* $RNiO_3$ perovskites (R = Pr, Nd): Nickel valence and the metal-insulator transition investigated by x-ray-absorption spectroscopy.

Phys. Rev. B **46**, 14975–14984 (1992). URL http://dx.doi.org/10.1103/PhysRevB.46.14975. 78, 89, 90, 93, 137, 142, 143, 155

[68] Piamonteze, C. *et al.* Spin-orbit-induced mixed-spin ground state in RNiO$_3$ perovskites probed by x-ray absorption spectroscopy: Insight into the metal-to-insulator transition. *Phys. Rev. B* **71**, 020406 (2005). URL http://link.aps.org/doi/10.1103/PhysRevB.71.020406. 91, 113, 151

[69] Bodenthin, Y. *et al.* Magnetic and electronic properties of RNiO$_3$ (R = Pr, Nd, Eu, Ho and Y) perovskites studied by resonant soft x-ray magnetic powder diffraction. *Journal of Physics: Condensed Matter* **23**, 036002 (2011). URL http://stacks.iop.org/0953-8984/23/i=3/a=036002. 78, 89, 90, 92, 113, 137, 155

[70] Wold, A., Post, B. & Banks, E. Rare earth nickel oxides. *J. Am. Chem. Soc.* **79**, 4911–4913 (1957). URL http://pubs.acs.org/doi/abs/10.1021/ja01575a022. 81

[71] Iakoubovskii, K., Mitsuishi, K., Nakayama, Y. & Furuya, K. Thickness measurements with electron energy loss spectroscopy. *Microsc. Res. and Tech.* **71**, 626–631 (2008). URL http://dx.doi.org/10.1002/jemt.20597. 85

[72] Malis, T., Cheng, S. C. & Egerton, R. F. EELS log-ratio technique for specimen-thickness measurement in the TEM. *J. of Elec. Microsc. Tech.* **8**, 193–200 (1988). URL http://dx.doi.org/10.1002/jemt.1060080206. 85

[73] Zhu, M. *et al.* Effect of composition and strain on the electrical properties of LaNiO$_3$ thin films. *Appl. Phys. Lett.* **103**, 141902 (2013). 87

[74] Alonso, J. A. *et al.* Charge disproportionation in Rnio$_3$ perovskites: Simultaneous metal-insulator and structural transition in ynio$_3$. *Phys. Rev. Lett.* **82**, 3871–3874 (1999). URL http://link.aps.org/doi/10.1103/PhysRevLett.82.3871. 92

[75] Lu, Y. *et al.* Quantitative determination of bond order and lattice distortions in nickel oxide heterostructures by resonant x-ray scattering. *Phys. Rev. B* **93**, 165121 (2016). URL http://link.aps.org/doi/10.1103/PhysRevB.93.165121. 92

[76] Han, M. J., Marianetti, C. A. & Millis, A. J. Chemical control of orbital polarization in artificially structured transition-metal oxides: La_2NiXO_6 (X=B, Al, Ga, In) from first principles. *Phys. Rev. B* **82**, 134408 (2010). URL http://link.aps.org/doi/10.1103/PhysRevB.82.134408. 92

[77] Freeland, J. W. *et al.* Orbital control in strained ultra-thin $LaNiO_3$ / $LaAlO_3$ superlattices. *EPL (Europhysics Letters)* **96**, 57004 (2011). URL http://stacks.iop.org/0295-5075/96/i=5/a=57004. 92, 137

[78] Zaanen, J., Sawatzky, G. A. & Allen, J. W. Band gaps and electronic structure of transition-metal compounds. *Phys. Rev. Lett.* **55**, 418–421 (1985). URL http://link.aps.org/doi/10.1103/PhysRevLett.55.418. 93, 142

[79] Abbate, M. *et al.* Electronic structure and metal-insulator transition in $lanio_{3-\delta}$. *Phys. Rev. B* **65**, 155101 (2002). URL http://link.aps.org/doi/10.1103/PhysRevB.65.155101.

[80] Han, M. J., Wang, X., Marianetti, C. A. & Millis, A. J. Dynamical mean-field theory of nickelate superlattices. *Phys. Rev. Lett.* **107**, 206804 (2011). URL http://link.aps.org/doi/10.1103/PhysRevLett.107.206804. 93, 142

[81] Landau, L. D. The theory of a Fermi liquid. *Journal of Experimental and Theoretical Physics* **3**, 920 (1957). URL http://jetp.ac.ru/cgi-bin/e/index/e/3/6/p920?a=list. 95

[82] Maslov, D. L., Yudson, V. I. & Chubukov, A. V. Resistivity of a non-galilean–invariant Fermi liquid near Pomeranchuk quantum criticality. *Phys. Rev. Lett.* **106**, 106403 (2011). URL http://link.aps.org/doi/10.1103/PhysRevLett.106.106403. 95

[83] Rosch, A. Magnetotransport in nearly antiferromagnetic metals. *Phys. Rev. B* **62**, 4945–4962 (2000). URL http://link.aps.org/doi/10.1103/PhysRevB.62.4945. 95, 110

[84] Sreedhar, K. *et al.* Electronic properties of the metallic perovskite $LaNiO_3$: Correlated behavior of 3*d* electrons. *Phys. Rev. B* **46**, 6382–6386 (1992). URL http://link.aps.org/doi/10.1103/PhysRevB.46.6382. 96, 97

[85] Xu, X. Q., Peng, J. L., Li, Z. Y., Ju, H. L. & Greene, R. L. Resisitivity, thermopower, and susceptibility of $RNiO_3$ (R = La,Pr). *Phys. Rev. B* **48**, 1112–1118 (1993). URL http://link.aps.org/doi/10.1103/PhysRevB.48.1112. 96, 97

[86] Moon, E. J. *et al.* Strain-dependent transport properties of the ultra-thin correlated metal, $LaNiO_3$. *New Journal of Physics* **13**, 073037 (2011). URL http://stacks.iop.org/1367-2630/13/i=7/a=073037. 96, 97, 100, 112

[87] Lee, P. A. & Ramakrishnan, T. V. Disordered electronic systems. *Rev. Mod. Phys.* **57**, 287–337 (1985). URL http://link.aps.org/doi/10.1103/RevModPhys.57.287. 96, 172

[88] Mikheev, E. *et al.* Tuning bad metal and non-Fermi liquid behavior in a Mott material: Rare-earth nickelate thin films. *Science Advances* **1** (2015). URL http://advances.sciencemag.org/content/1/10/e1500797. 96, 97, 100

[89] Buhmann, J. M. Unconventional scaling of resistivity in two-dimensional fermi liquids. *Phys. Rev. B* **88**, 245128 (2013). URL http://link.aps.org/doi/10.1103/PhysRevB.88.245128. 99, 100, 114

[90] Moon, E. J. *et al.* Strain-controlled band engineering and self-doping in ultra-thin $LaNiO_3$ films. *Phys. Rev. B* **85**, 121106 (2012). URL http://link.aps.org/doi/10.1103/PhysRevB.85.121106. 101

[91] Eguchi, R. *et al.* Fermi surfaces, electron-hole asymmetry, and correlation kink in a three-dimensional fermi liquid $LaNiO_3$. *Phys. Rev. B* **79**, 115122 (2009). URL http://link.aps.org/doi/10.1103/PhysRevB.79.115122. 101, 104, 105

[92] Yoo, H. K. *et al.* Dimensional crossover of the electronic structure in $LaNiO_3$ ultrathin films: Orbital reconstruction, Fermi surface nesting, and the origin of the metal-insulator transition. *ArXiv e-prints* (2013). URL http://adsabs.harvard.edu/abs/2013arXiv1309.0710Y. 103

[93] Yoo, H. K. *et al.* Latent instabilities in metallic $LaNiO_3$ films by strain control of Fermi-surface topology. *Scientific Reports* **5**, 8746 (2015). URL http://dx.doi.org/10.1038/srep08746. 101

[94] Allen, S. J. *et al.* Gaps and pseudogaps in perovskite rare earth nickelates. *APL Mater.* **3** (2015). URL http://scitation.aip.org/content/aip/journal/aplmater/3/6/10.1063/1.4907771. 103, 105

[95] Kumah, D. P. *et al.* Tuning the structure of nickelates to achieve two-dimensional electron conduction. *Advanced Materials* **26**, 1935–1940 (2014). URL http://dx.doi.org/10.1002/adma.201304256. 103, 106, 112

[96] Nowadnick, E. A. *et al.* Quantifying electronic correlation strength in a complex oxide: A combined DMFT and ARPES study of $LaNiO_3$. *Phys. Rev. B* **92**, 245109 (2015). URL http://link.aps.org/doi/10.1103/PhysRevB.92.245109. 105

[97] Kumah, D. P. *et al.* Effect of surface termination on the electronic properties of $LaNiO_3$ films. *Phys. Rev. Applied* **2**, 054004 (2014). URL http://link.aps.org/doi/10.1103/PhysRevApplied.2.054004. 106

[98] Gayathri, N., Raychaudhuri, A. K., Xu, X. Q., Peng, J. L. & Greene, R. L. Magnetoresistance of the metallic perovskite oxide $LaNiO_3$. *Journal of Physics: Condensed Matter* **11**, 2901 (1999). URL http://stacks.iop.org/0953-8984/11/i=14/a=006. 107, 111, 112

[99] Abrikosov, A. A. Quantum linear magnetoresistance. *EPL (Europhysics Letters)* **49**, 789 (2000). URL http://stacks.iop.org/0295-5075/49/i=6/a=789. 109, 110, 111

[100] Abrikosov, A. A. Quantum magnetoresistance. *Phys. Rev. B* **58**, 2788–2794 (1998). URL http://link.aps.org/doi/10.1103/PhysRevB.58.2788. 111

[101] Parish, M. M. & Littlewood, P. B. Classical magnetotransport of inhomogeneous conductors. *Phys. Rev. B* **72**, 094417 (2005). URL http://link.aps.org/doi/10.1103/PhysRevB.72.094417. 110

[102] Bud'ko, S. L., Canfield, P. C., Mielke, C. H. & Lacerda, A. H. Anisotropic magnetic properties of light rare-earth diantimonides. *Phys. Rev. B* **57**, 13624–13638 (1998). URL http://link.aps.org/doi/10.1103/PhysRevB.57.13624. 110

[103] Zhao, J. G. *et al.* High-pressure synthesis of orthorhombic $SrIrO_3$ perovskite and its positive magnetoresistance. *Journal of Applied Physics* **103** (2008). URL http://scitation.aip.org/content/aip/journal/jap/103/10/10.1063/1.2908879;jsessionid=dcyPjd-iFRUT9PoCawXYF5AL.x-aip-live-02. 111

[104] Demazeau, G., Parent, C., Pouchard, M. & Hagenmuller, P. Sur deux nouvelles phases oxygenées du cuivre trivalent: $LaCuO_3$ et $La_2Li_{0.50}Cu_{0.50}O_4$. *Materials Research Bulletin* **7**, 913 – 920 (1972). URL http://www.sciencedirect.com/science/article/pii/0025540872900803. 116

[105] Lee, J. H. *et al.* Dynamic layer rearrangement during growth of layered oxide films by molecular beam epitaxy. *Nat Mater* **13**, 879–883 (2014). 118, 160

[106] Wang, Y., Salzberger, U., Sigle, W., Suyolcu, Y. E. & van Aken, P. A. Oxygen octahedra picker: A software tool to extract quantitative information from {STEM} images. *Ultramicroscopy* **168**, 46 – 52 (2016). URL http://www.sciencedirect.com/science/article/pii/S0304399116300808. 127

[107] Reehuis, M. *et al.* Crystal structure and high-field magnetism of La_2CuO_4. *Phys. Rev. B* **73**, 144513 (2006). URL http://link.aps.org/doi/10.1103/PhysRevB.73.144513. 134, 141, 150, 166

[108] Braden, M. *et al.* Relation between structure and doping in $La_{2-x}Sr_xCuO_{4+\delta}$ a neutron diffraction study on single crystals. *Physica C: Superconductivity* **223**, 396 – 416 (1994). URL http://www.sciencedirect.com/science/article/pii/092145349491284X. 134, 141

[109] Bianconi, A. *et al.* Evidence of $3d^9$-ligand hole states in the superconductor $La_{1.85}Sr_{0.15}CuO_4$ from L_3 x-ray absorption spectroscopy. *Physics Letters A* **127**, 285–291 (1988). URL http://www.sciencedirect.com/science/article/pii/0375960188906986. 137, 139, 147

[110] Sarma, D. D. *et al.* Electronic structure of high-T_c superconductors from soft-x-ray absorption. *Phys. Rev. B* **37**, 9784–9787 (1988). URL http://link.aps.org/doi/10.1103/PhysRevB.37.9784. 139, 140, 147

[111] Grioni, M. *et al.* Studies of copper valence states with Cu L_3 x-ray-absorption spectroscopy. *Phys. Rev. B* **39**, 1541–1545 (1989). URL http://link.aps.org/doi/10.1103/PhysRevB.39.1541. 139, 140

[112] Flipse, C. F. J., van der Laan, G., Johnson, A. L. & Kadowaki, K. Soft-x-ray absorption spectroscopy of electron-doped $(Nd,Sm)_{2-x}Ce_xCuO_{4-\delta}$ compounds. *Phys. Rev. B* **42**, 1997–2002 (1990). URL http://link.aps.org/doi/10.1103/PhysRevB.42.1997.

[113] Fink, J. *et al.* Electron energy-loss and x-ray absorption spectroscopy of cuprate superconductors and related compounds. *Journal of Electron Spectroscopy and Related Phenomena* **66**, 395 – 452 (1994). URL http://www.sciencedirect.com/science/article/pii/036820489301857B. 139, 147

[114] Nücker, N. *et al.* Site-specific and doping-dependent electronic structure of $YBa_2Cu_3O_x$ probed by O 1 *s* and Cu 2 *p* x-ray-absorption spectroscopy. *Phys.*

Rev. B **51**, 8529–8542 (1995). URL http://link.aps.org/doi/10.1103/PhysRevB.51.8529. 137

[115] Pompa, M. *et al.* Full multiple scattering analysis of linearly polarized Cu L_3-edge XANES of La_2CuO_4. *Physica C: Superconductivity* **184**, 51 – 64 (1991). URL http://www.sciencedirect.com/science/article/pii/0921453491915004. 137, 140

[116] Chen, C. T. *et al.* Out-of-plane orbital characters of intrinsic and doped holes in $La_{2-x}Sr_xCuO_4$. *Phys. Rev. Lett.* **68**, 2543–2546 (1992). URL http://link.aps.org/doi/10.1103/PhysRevLett.68.2543. 141

[117] Núñez Regueiro, M. D., Altarelli, M. & Chen, C. T. X-ray-absorption sum rule for linear dichroism: Application to high-T_c cuprate oxides. *Phys. Rev. B* **51**, 629–631 (1995). URL http://dx.doi.org/10.1103/PhysRevB.51.629. 137, 140, 141

[118] Mizokawa, T. *et al.* Electronic structure of $PrNiO_3$ studied by photoemission and x-ray-absorption spectroscopy: Band gap and orbital ordering. *Phys. Rev. B* **52**, 13865–13873 (1995). URL http://link.aps.org/doi/10.1103/PhysRevB.52.13865. 137

[119] Qiao, R. *et al.* Direct experimental probe of the Ni(II)/Ni(III)/Ni(IV) redox evolution in $LiNi_{0.5}Mn_{1.5}O_4$ electrodes. *The Journal of Physical Chemistry C* **119**, 27228–27233 (2015). URL http://dx.doi.org/10.1021/acs.jpcc.5b07479. http://dx.doi.org/10.1021/acs.jpcc.5b07479. 137

[120] Strebel, O. *et al.* Valency and covalency in high-T_c-superconductors from x-ray absorption. *Physica C: Superconductivity* **162**, 1331–1332 (1989). URL http://www.sciencedirect.com/science/article/pii/0921453489907181. 138, 139

[121] van Aken, P., Müller, W. & Choisnet, J. Strong reduction of the electron-doped superconductor $Nd_{2-x}Ce_xCuO_{4-\delta}$. *Physica C: Superconductivity* **211**, 421–432 (1993). URL http://www.sciencedirect.com/science/article/pii/092145349390149K. 139

[122] Condon, E. & Shortley, G. *The Theory of Atomic Spectra* (Cambridge University Press, 1951). URL https://books.google.de/books?id=hPyD-Nc_YmgC. 139

[123] van der Laan, G., Pattrick, R., Henderson, C. & Vaughan, D. Oxidation state variations in copper minerals studied with Cu 2p x-ray absorption spectroscopy. *Journal of Physics and Chemistry of Solids* **53**, 1185 – 1190 (1992). URL http://www.sciencedirect.com/science/article/pii/002236979290037E. 139, 146

[124] Ronay, M. *et al.* A new correlation for T_c from Cu $2p$ absorption. *Solid State Communications* **77**, 699 – 702 (1991). URL http://www.sciencedirect.com/science/article/pii/003810989190772N. 140, 147

[125] Pellegrin, E. *et al.* Orbital character of states at the fermi level in $La_{2-x}Sr_xCuO_4$ and $R_{2-x}Ce_xCuO_4$ (R = Nd,Sm). *Phys. Rev. B* **47**, 3354–3367 (1993). URL http://link.aps.org/doi/10.1103/PhysRevB.47.3354. 140

[126] Mei, C.-J. & Stollhoff, G. Electronic structure and correlations of high-temperature superconducting compounds. *Phys. Rev. B* **43**, 3065–3074 (1991). URL http://link.aps.org/doi/10.1103/PhysRevB.43.3065. 140

[127] Carra, P., König, H., Thole, B. & Altarelli, M. Magnetic x-ray dichroism. *Physica B: Condensed Matter* **192**, 182 – 190 (1993). URL http://www.sciencedirect.com/science/article/pii/092145269390119Q. 141

[128] Kambe, S. *et al.* Anisotropic resistivity in the two-dimensional metal $La_{2-x}Sr_xCuO_4$. *Physica C: Superconductivity* **160**, 35 – 41 (1989). URL http://www.sciencedirect.com/science/article/pii/0921453489904498. 141

[129] Kao, H. L., Kwo, J., Takagi, H. & Batlogg, B. Systematics of transport anisotropy in single-domain $La_{2-x}Sr_xCuO_4$ films. *Phys. Rev. B* **48**, 9925–9928 (1993). URL http://link.aps.org/doi/10.1103/PhysRevB.48.9925. 141

[130] Chakhalian, J. *et al.* Orbital reconstruction and covalent bonding at an oxide interface. *Science* **318**, 1114–1117 (2007). URL http://science.sciencemag.org/content/318/5853/1114. http://science.sciencemag.org/content/318/5853/1114.full.pdf. 146

[131] Nücker, N. *et al.* Experimental electronic structure studies of $La_{2-x}Sr_xCuO_4$. *Zeitschrift für Physik B Condensed Matter* **67**, 9–14 (1987). URL http://dx.doi.org/10.1007/BF01307300. 147

[132] Bruno, F. Y. *et al.* Probing the metal-insulator transition in nickelates using soft x-ray absorption spectroscopy. *Applied Physics Letters* **104** (2014). URL http://scitation.aip.org/content/aip/journal/apl/104/2/10.1063/1.4861132. 155

[133] Wu, M. *et al.* Orbital reflectometry of $PrNiO_3/PrAlO_3$ superlattices. *Phys. Rev. B* **91**, 195130 (2015). URL http://link.aps.org/doi/10.1103/PhysRevB.91.195130. 155

[134] Alders, D. *et al.* Temperature and thickness dependence of magnetic moments in nio epitaxial films. *Phys. Rev. B* **57**, 11623–11631 (1998). URL http://link.aps.org/doi/10.1103/PhysRevB.57.11623. 156

[135] Thio, T. *et al.* Antisymmetric exchange and its influence on the magnetic structure and conductivity of la_2cuo_4. *Phys. Rev. B* **38**, 905–908 (1988). URL http://link.aps.org/doi/10.1103/PhysRevB.38.905. 159

[136] Orenstein, J. & Vishwanath, A. Doped mott insulators: Breaking through to the other side. *Nat Phys* **6**, 566–567 (2010). URL http://dx.doi.org/10.1038/nphys1751. 160

[137] Suter, A. *et al.* Antiferromagnetic transition in epitaxial strained La_2CuO_4 thin films. *Journal of Magnetism and Magnetic Materials* **272–276, Part 1**, 110–111 (2004). URL http://www.sciencedirect.com/science/article/pii/S0304885303009727. Proceedings of the International Conference on Magnetism (ICM 2003). 160

[138] Coffey, D., Rice, T. M. & Zhang, F. C. Dzyaloshinskii-moriya interaction in the cuprates. *Phys. Rev. B* **44**, 10112–10116 (1991). URL http://link.aps.org/doi/10.1103/PhysRevB.44.10112. 160, 166

[139] Sreedhar, K. *et al.* Low-temperature electronic properties of the $La_{n+1}Ni_nO_{3n+1}$ (n = 2, 3, and ∞) system: Evidence for a crossover from fluctuating-valence to fermi-liquid-like behavior. *Journal of Solid State Chemistry* **110**, 208–215 (1994). URL http://www.sciencedirect.com/science/article/pii/S0022459684711613. 160

[140] Zhang, Z., Greenblatt, M. & Goodenough, J. B. Synthesis, structure, and properties of the layered perovskite $La_3Ni_2O_{7-\delta}$. *Journal of Solid State Chemistry* **108**, 402–409 (1994). URL https://www.scopus.com/inward/record.uri?eid=2-s2.0-0001215550&partnerID=40&md5=fccb01428f3ff66229cdd5786d8de583. 160, 161, 170

[141] Greenblatt, M., Zhang, Z. & Whangbo, M. H. Electronic properties of $La_3Ni_2O_7$ and $Ln_4Ni_3O_{10}$, Ln=La, Pr and Nd. *Synthetic Metals* **85**, 1451–1452 (1997). URL http://www.sciencedirect.com/science/article/pii/S0379677997803128. 161, 170, 172

[142] Ling, C. D., Argyriou, D. N., Wu, G. & Neumeier, J. Neutron diffraction study of $La_3Ni_2O_7$: Structural relationships among n = 1, 2, and 3 phases $La_{n+1}Ni_nO_{3n+1}$. *Journal of Solid State Chemistry* **152**, 517 – 525 (2000). URL http://www.sciencedirect.com/science/article/pii/S0022459600987218. 160

[143] Wu, G., Neumeier, J. J. & Hundley, M. F. Magnetic susceptibility, heat capacity, and pressure dependence of the electrical resistivity of $La_3Ni_2O_7$ and $La_4Ni_3O_{10}$. *Phys. Rev. B* **63**, 245120 (2001). URL http://link.aps.org/doi/10.1103/PhysRevB.63.245120. 160, 172

[144] Zhang, Z. & Greenblatt, M. Synthesis, structure, and properties of $Ln_4Ni_3O_{10-\delta}$ (Ln = La, Pr, and Nd). *Journal of Solid State Chemistry* **117**, 236 – 246

(1995). URL http://www.sciencedirect.com/science/article/pii/S0022459685712698. 161, 170, 172

[145] Wang, Z. *et al.* Magnetoelectric effect and phase transitions in CuO in external magnetic fields. *Nat Commun* **7**, 10295 (2016). URL http://dx.doi.org/10.1038/ncomms10295. 164

[146] Chen, C. T., Sette, F., Ma, Y. & Modesti, S. Soft-x-ray magnetic circular dichroism at the $L_{2,3}$ edges of nickel. *Phys. Rev. B* **42**, 7262–7265 (1990). URL http://link.aps.org/doi/10.1103/PhysRevB.42.7262. 170

[147] Vogel, J. & Sacchi, M. *Dichroism in X-ray Absorption for the Study of Antiferromagnetic Materials*, 69–97 (Wiley-VCH Verlag GmbH & Co. KGaA, 2010). URL http://dx.doi.org/10.1002/9783527630370.ch3. 170

[148] Wu, M. *X-ray Magnetic Circular Dichroism study of Nickel oxide Heterostructures*. Master's thesis, University of Stuttgart (2013). 170, 175

[149] Ono, S. *et al.* Spin reorientation and in-plane magnetoresistance of lightly doped $La_{2-x}Sr_xCuO_4$ in magnetic fields up to 55 T. *Phys. Rev. B* **70**, 184527 (2004). URL http://link.aps.org/doi/10.1103/PhysRevB.70.184527. 172

[150] Bergmann, G. Weak localization in thin films. *Physics Reports* **107**, 1 – 58 (1984). URL http://www.sciencedirect.com/science/article/pii/0370157384901030. 172

[151] Schubert, E. F. Delta doping of III–V compound semiconductors: Fundamentals and device applications. *Journal of Vacuum Science & Technology A* **8**, 2980–2996 (1990). URL http://scitation.aip.org/content/avs/journal/jvsta/8/3/10.1116/1.576617. 176

[152] Baiutti, F. *et al.* High-temperature superconductivity in space-charge regions of lanthanum cuprate induced by two-dimensional doping. *Nat Commun* **6**, 1–8 (2015). URL http://www.nature.com/ncomms/2015/151020/ncomms9586/full/ncomms9586.html. 176, 177

Acknowledgments

Now, that a long period of intense studying with all the highs and lows is about to reach its climax, it is time to express my gratitude towards a number of people. As there is an almost infinite amount of people who have made it possible for me to be where I am right now, this list will never be complete.

First of all, I would like to thank Prof. Keimer for giving me the opportunity to join his department and to gain insight into the exciting world of condensed matter physics (despite my chemistry background). I am a little bit proud that I won't be the last chemist in the department. I enjoyed a lot the immense knowledge that one can access in this department and in this institute.

I appreciate the consent of Prof. Weidenkaff and Prof. Niewa to evaluate my thesis work and to be the members of my Ph.D. examination committee.

I am grateful towards Dr. Eva Benckiser as my day-to-day supervisor. For introducing me into the field of nickelates – in fact, it is a bit ironic that the only allergy I have is against nickel. I still enjoy to learn more and more on this topic though and appreciate your help in understanding more and more.

I thank Dr. Gennady Logvenov, who is practically my second day-to-day supervisor, overseeing my growth although it is not a lot with something in the order of 2μm per year. All jokes aside, I appreciate your guidance and calmness.

Next in the list are Georg Christiani and Peter Specht, who keep the MBE running. Georg, thank you for arriving so early every morning enabling me to start early (at least for a scientist) and get as much out of a growth day as possible. Thank you, Peter, for all the repairs and for explaining me a lot of the technical details.

I feel blessed for having such wonderful and peaceful office mates, Jitae Park, Ali-

aksei Charnukha, Andreas Dittmaier, Giorgi Ghambashidze, Sewon Jeong, Michaela Souliou, Maximilian Krautloher, Hun-Ho Kim and Daniel Putzky. I look back with joy to the discussions on weather, on soccer, the nameless baby, and to “We will rock you”.

Beamtimes are always quite exhausting. But thanks to great colleagues, they can still be fun. The Flammkuchen (I highly appreciate the vegan version, Daniel!), the shifting of birthdays, the soccer ball, the mint leaf, the cat videos, the walks through the night through a deserted campus. Here, I should name (roughly in the order of appearence in my beamtime history) Meng Wu, Alex Frano, Yi Lu, Patrick Audehm, Daniel Pröpper, Santiago Blanco-Canosa, Willi Mahler, Timofei Larkin, Agnes Szoekefalvi-Nagy, Peter Wochner, Martin Bluschke, Matthias Hepting, Christopher Dietl, Daniel Putzky, Shyjumon Ibrahimkutty, Padma Radhakrishnan, Enrico Schierle.

I appreciate the presence of all members of the department, old and new ones and the support that I experienced.

I appreciate the support also from colleagues outside of the department: Yvonne and Benjamin Stuhlhofer and Birgit Lemke and Stephan Schmid for sputtering the contacts and other, little things. Hans Boschker for help with substrate termination and with transport measurements. Marco Lanzano for the magic box and for introducing me to the wire saw. Andreas Rost, Hiro Nakamura, Jan Bruin and Ali Bangura for help with transport measurements, for explaining me the theory behind and for fruitful discussions. Eberhard Goering for help with the XMCD analyses.

To me, the cheerfulness of the porters no matter what time of the day and the friendliness of the cleaning personnel contributed a lot to the good atmosphere I experienced during my time at the MPI.

With respect to people outside of the MPI sphere – in my view the MPI sphere includes the synchrotrons – I need to mention Lucas Tang and Alix McCollam from the High Field Magnet Laboratory at Radboud University. Many thanks to Lucas for operating the impressive machines and Alix for a great deal of useful advice.

I am grateful for the friends I have, at the institute, in Stuttgart and all over the world who fill my life with joy. In particular, I highly appreciate the cheering and support of Dr. Khan on the home stretch.

And above all I would like to express my deep gratitude towards my family, my

mum, my dad and my sister. Expressing gratitude in spoken words is way more difficult for me than in written words. So I'd like to seize the opportunity now: Mum, dad, sister, no matter what happens, I know that I can rely on you, I know that you believe in me. This knowledge is the fountain from which I gain my strength, it is the fertile soil into which I can put my roots to prosper and thrive. Thank you for your everlasting support!